# Earth system carbon cycle dynamics through time

**Mathis P Hain[a], Kathrine A Allen[b], and Sandra Kirtland Turner[c]**, [a]Department of Earth and Planetary Sciences, University of California, Santa Cruz, CA, United States; [b]School of Earth and Climate Sciences, University of Maine, Orono, ME, United States; [c]Department of Earth and Planetary Sciences, University of California, Riverside, CA, United States





## Abstract

Earth's carbon cycle controls the concentration of the greenhouse gas carbon dioxide ($CO_2$) in the atmosphere, which influences the climate on our planet and thereby affects the many processes that control the carbon cycle. These climate-carbon cycle feedbacks determine the long-term Earth System response to biological evolution, geologic drivers, and events such as anthropogenic fossil fuel use. In Section "Earth's carbon cycle" of this chapter we outline the reservoirs and chemistry of carbon in Earth's surface environment; in Section "Carbon fluxes and dynamic balances" we describe the dynamics underpinning carbon cycle feedbacks, including a discussion of carbon cycle models, and in Section "Climate and the carbon cycle" we survey the observational evidence base for our current understanding of long-term Earth System change by focusing on available proxy records and reconstructions of the climate and carbon cycle across the Cenozoic Era. In facing our collective impacts on Earth's future carbon cycle and climate these concepts are fundamental to human stewardship of our environment.

## Keywords

Atmospheric carbon dioxide; Boron isotopes; Carbon chemistry; Carbon cycle feedbacks; Carbon cycle models; Carbon isotopes; Carbonate compensation; Climate change; $CO_2$; Earth system; Ocean biological pump; Oxygen isotopes; Paleo proxy; Seawater alkalinity; Seawater pH; Silicate weathering thermostat

**Key points**

- Define feedback dynamics that stabilize fluxes among carbon reservoirs
- Survey key proxy systems used to reconstruct climate-carbon cycle coupling
- Outline reconstructed Earth System trends, shifts, rhythms, and aberrations

## Introduction

In this chapter, we review fundamental carbon cycle concepts that determine the distribution of carbon on Earth's surface and connect this conceptual understanding to the Cenozoic record of carbon cycle and climate interactions as well as the future fate of anthropogenic $CO_2$. Our review leads us to outline new recommendations for future paleo-reconstruction projects and data-model synthesis efforts aimed at constraining feedbacks between the carbon cycle and climate. We use results from a series of $CO_2$-injection experiments with the cGENIE intermediate complexity Earth system model to differentiate and illustrate the importance of "closed-system" redistribution of carbon within Earth's surface environment versus "open-system" exchanges with the solid Earth, demonstrating the timescales over which dynamic balances emerge. Rapid injection of $CO_2$ into Earth's atmosphere is immediately taken up by the ocean ($\sim 10^2$–$10^3$ year timescale), followed by seafloor carbonate compensation ($\sim 10^3$–$10^4$ year timescale), and a full "climate recovery" or reestablishment of initial atmospheric temperature ultimately occurs via the silicate weathering feedback, which takes $\sim 10^5$–$10^6$ years to return Earth to balance–a concept commonly referred to as "steady state." In this chapter, we also utilize refined terminology for categorizing paleo observations with respect to the relevant carbon cycle timescales described above, specifically: a "**trend**" is a secular drift in open-system steady state, which occurs on a timescale greater than the silicate weathering feedback; a "**transition**" occurs on the order of $10^5$ years but fails to recover or reverse over the silicate weathering timescale; an "**aberration**" is an abrupt disruption to the carbon cycle that does not correspond to an imbalance between carbon input fluxes and silicate weathering or a change in steady state; carbon "**optima**" are steady state intervals of high $CO_2$ maintained by elevated rates of carbon input –in other words, they are driven by changes in open-system fluxes; "**rhythms**" correlate with quasi-cyclic variations in Earth's orbital geometry, and finally "**variability**" refers to changes that occur over a millennial or shorter timescale. Ultimately, paleo proxies provide a window into Earth's past that may be used to explore how the carbon-climate system responds to perturbations and shifting boundary conditions through time. Development of these proxies is an ongoing endeavor, and it is becoming ever more clear that systems of independent proxies must be applied to fully constrain the carbon cycle, particularly the ocean's carbonate system. Further insight into the mechanisms governing the carbon cycle will come from combining increased temporal- and spatial-resolution reconstructions based on established and novel proxy systems with new numerical modeling approaches to assimilate these data. Close partnership between those who model the carbon-climate system and those who collect new observations from physical materials is crucial to the research community's mission to understand the boundaries, controls, and instabilities in Earth's linked carbon-climate system.

## Earth's carbon cycle

Evolution of life on Earth and its diverse biochemical pathways have over geologic time reshaped the surface environment and created a complex network of global biogeochemical cycles, such as the global carbon cycle. To achieve a long-term stability the coupled Earth System needs to maintain at least four delicate balances: (1) gross atmospheric $CO_2$ exchange into and out of the surface ocean are nearly balanced, (2) net primary production of biomass by photosynthesis is nearly balanced by heterotrophic respiration of that biomass, yielding a relatively small net accumulation and burial of organic carbon shown as $CH_2O$, (3) cation supply to the ocean from continental weathering is balanced by burial of carbonate ($CaCO_3$) ocean sediments, and (4) geologic $CO_2$ sources are thought to be balanced primarily by climate-dependent silicate mineral weathering and some burial of organic carbon from (2), represented by the following simplified reactions:

$$CO_2 + H_2O \leftrightarrow H_2CO_3 \leftrightarrow HCO_3^- + H^+ \leftrightarrow CO_3^{2-} + 2H^+ \quad (1)$$

$$CO_2 + H_2O \leftrightarrow CH_2O + O_2 \quad (2)$$

$$CO_2 + H_2O + Ca^{2+} \leftrightarrow CaCO_3 + 2H^+ \quad (3)$$

$$CO_2 + CaSiO_3 \leftrightarrow CaCO_3 + SiO_2 \quad (4)$$

Carbon dioxide ($CO_2$) dissolves into seawater ($H_2O$) to form carbonic acid, which can give off protons ($H^+$) to form bicarbonate and carbonate ion as a matter of acid/base chemistry (Eq. 1). Photosynthesis uses sunlight to convert inorganic carbon of oxidation state +IV ($CO_2$ on the left) into organic carbon of oxidation state 0 ($CH_2O$ on the right) and thereby sequesters carbon from ocean and atmosphere and produces oxygen ($O_2$ on the right), whereas respiration yields energy by oxidizing the organic matter back to inorganic carbon (Eq. 2). Formation of $CaCO_3$ acidifies the remaining seawater (produces $H^+$ on the right), whereas

$CaCO_3$ dissolution (right to left) neutralizes ocean acidification (Eq. 3). Silicate mineral weathering reactions convert $CO_2$ to $CaCO_3$ without ocean acidification (left to right in Eq. 4). Each of these reactions involves carbon in the form of $CO_2$, exemplifying the multiple controls on the relatively small atmospheric $CO_2$ reservoir (e.g., Sundquist and Visser Ackerman, 2014). These dynamics will be covered in Section "Carbon fluxes and dynamic balances". First, in Section "Earth's carbon cycle" we outline the geographic distribution of distinct carbon reservoirs of the Earth System (Section "Carbon reservoirs"), describe how these reservoirs are represented in models of the carbon cycle (Section "Carbon chemistry"), and highlight the chemical speciation effects on the solubility of $CO_2$ in seawater (Section "Carbon cycle models").

## Carbon reservoirs

Earth's carbon can be broadly divided into two sets of reservoirs: the combined "surface carbon" reservoir of ocean, atmosphere and (land) biosphere, and "geologic carbon" contained in rock formations and stored in sediments (Fig. 1). Surface carbon cycling is very rapid, but surface carbon is only a tiny fraction of all carbon on Earth. The vast majority of carbon is geologic and only exchanges very slowly with the surface (Sundquist and Visser Ackerman, 2014). Geologic carbon includes inorganic carbonate minerals that make up limestone, and organic forms of carbon either finely dispersed through sediment sequences or concentrated in coal seams, methane hydrates, and deeply buried permafrost that tend to accumulate slowly but can potentially be released rapidly back to the surface. Some ancient organic carbon has been converted to natural gas and petroleum, which humans started to industrially extract and burn: anthropogenic carbon emission from fossil fuel use rapidly releases geologic carbon to the surface (Fig. 1). Carbon in the surface environment (Eq. 5) is rapidly exchanged among the ocean, atmosphere, and land biosphere, where

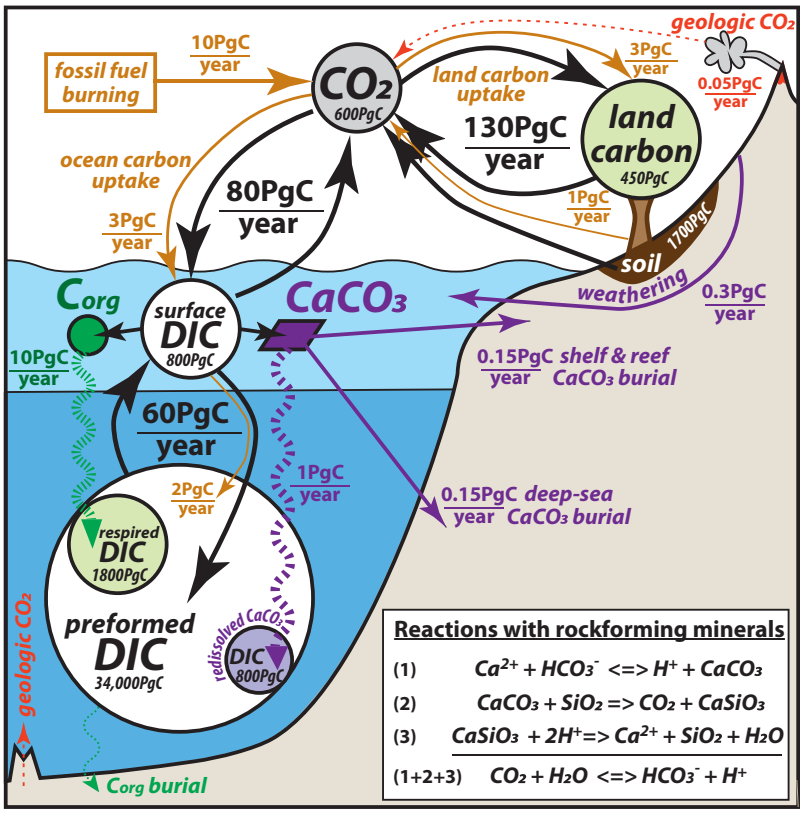


**Fig. 1** Schematic Earth surface carbon cycle. Three large exchange fluxes link the ocean, atmosphere and land surface carbon stocks: (1) land plant growth and heterotrophic respiration exchange about 130 petagram of carbon per year (PgC/year) of $CO_2$ with the atmosphere (Section "Land carbon storage"); (2) air/sea gas fluxes between atmosphere and surface ocean exchange $CO_2$ at a rate of about 80 PgC/year; where seawater carbon storage is predominantly in the form of dissolved inorganic carbon (DIC); and (3) ocean circulation exchanges seawater with its DIC between the surface ocean and the ocean interior, where only surface DIC can exchange with the atmosphere (Section "Air/sea $CO_2$ equilibration"). Plankton growth in the open ocean consumes surface DIC to produce organic matter ($C_{org}$) and calcium carbonate ($CaCO_3$) that "rains down" into the ocean interior before being converted back to DIC, thereby sequestering DIC and alkalinity (ALK; Section "Carbon cycle models") away from the atmosphere–a dynamic that is often referred to as the ocean's biological pump (Section "The ocean's biological pumps"). Exchanges, between the combined surface carbon stocks with carbon stocks held by the solid Earth are dominated by the weathering of limestone rock formations and the burial of $CaCO_3$ in marine sediments (Section "$CaCO_3$ compensation"), but other slow fluxes such as volcanic $CO_2$ emissions, weathering of silicate rocks (Section "Silicate weathering thermostat") as well as weathering and burial of organic carbon ($C_{org}$; Section "Organic carbon") can change the combined surface carbon stock when allowing for long geologic timescales. Highlighted in orange as a point of comparison are carbon fluxes associated with anthropogenic fossil fuel emissions and land use.

inventories of carbon on the left-hand side are usually reported in grams of carbon (gC) while concentrations of dissolved inorganic carbon (DIC), terrestrial organic carbon ($C_{org}$), and atmospheric $CO_2$ are often reported on the basis of the number of carbon atoms per mass of seawater, area of land surface, or number of other gas molecules, respectively. Average carbon concentrations can be converted to inventories with a factor of 12 gC per $6 \times 10^{23}$ (1 mol) of carbon atoms multiplied by the mass of the ocean ($M_{oc}$), land area ($A_{land}$), or number of gas molecules in the atmosphere ($N_{atm}$):

$$C_{oc} + C_{land} + C_{atm} \approx \frac{12\,gC}{molC} \left(\overline{DIC} \cdot M_{oc} + \overline{C_{org}} \cdot A_{land} + \overline{CO_2} \cdot N_{atm}\right) \quad (5)$$

### Ocean carbon

More than 90% of the total ~ 40,000 petagrams of carbon (PgC, $10^{15}$ gC) in the surface system resides in the ocean ($C_{oc}$), with about 9% of surface carbon stored in the land biosphere ($C_{land}$) and ~ 1% in the atmosphere ($C_{atm}$). Ocean carbon (excluding seafloor sediments; Fig. 1) exists predominantly in the form of dissolved inorganic carbon (DIC), where the average DIC (2250 μmol per kilogram seawater) multiplied by the ocean's mass ($M_{oc}$) yields the equivalent of about 38,000 PgC. The ocean carbon reservoir also includes dissolved organic carbon (DOC, not shown in Fig. 1). Most DOC is rapidly degraded back into DIC, but a proportion is highly refractory (Hansell, 2013; Jiao et al., 2010). The total inventory of DOC is estimated at ~600 Pg C (average concentration < 40 μmol/kg with higher values in the surface), and that inventory may have been relatively constant through Earth history (Fakhraee et al., 2021). Ocean biota, predominantly plankton, represent a comparatively small standing stock of just ~6 PgC particulate organic carbon (POC; Bar-On et al., 2018), where the carbon is contained within organic matter (OM) biomass. DIC is the carbon source for biological production of POC and DOC via photosynthesis (green $C_{org}$ in Fig. 1; Eq. 2, left to right), and respiration of that organic carbon returns the carbon to the DIC pool (right to left). Some marine organisms build hard parts from $CaCO_3$ (purple in Fig. 1; Eq. 3, left to right), yielding a <1PgC inventory of particulate inorganic carbon (PIC) suspended in the water column. Hence, more than 98% of all ocean carbon exists in the form of DIC, which unlike PIC, POC and DOC can directly exchange $CO_2$ with the atmosphere.

While the standing stocks of DOC, POC and PIC are small, they are central to the cycling of DIC in the ocean, yielding three distinct DIC components (Fig. 1; Eq. 6): (1) DIC can simply exchange with the atmosphere at the surface and then circulate into the ocean interior (about 34,000 PgC of preformed DIC), (2) DIC may be found in the ocean interior because organic carbon (DOC, POC) was produced in the surface and sank to depth before being respired ($DIC^{OM}_{respired}$; up to 2000 PgC), or (3) because $CaCO_3$ hard-parts of marine organisms (PIC) sank to depth from the surface before being dissolved ($DIC^{CaCO3}_{dissolved}$; up to 1000 PgC).

$$DIC = DIC_{preformed} + DIC^{OM}_{respired} + DIC^{CaCO_3}_{dissolved} \quad (6)$$

The top few centimeters of seafloor sediments contain both inorganic and organic carbon (~2500 and 650 Pg C, respectively) that are being converted into ocean DIC by dissolution and respiration while also being gradually buried and removed from the surface carbon cycle (Sundquist and Visser Ackerman, 2014). Only the surface sediment mixed layer resulting from the bioturbation by burrowing organisms is considered 'reactive' because it can return carbon to the ocean on relatively short timescales ($<10^4$ years, as described in Section "Open system exchanges"), whereas the reactivity of carbon below the surface sediment mixed layer is limited by diffusion. That is, most of the PIC and POC particles that settle onto the seafloor are recycled back into the surface carbon cycle and only a small fraction are preserved and buried to become part of the geologic carbon inventories.

### Land carbon

The terrestrial biosphere is a major reservoir of organic carbon (land carbon in Fig. 1; $C_{land}$ in Eqs. 5 and 7), storing about 450 PgC in living plants ($C_{plants}$), 1700 PgC in the upper 2 m of the soil column ($C_{soil}$) and an additional ~1400PgC in permafrost ($C_{permafrost}$) (Bar-On et al., 2018; Canadell and Monteiro, 2021; Friedlingstein et al., 2022), when summing across Earth's land surface area ($A_{land}$). For practical reasons organic carbon storage is commonly measured and reported on a per square meter basis ($C_{org}$ in Eq. 5; molC/$m^2$).

$$C_{land} = C_{plants} + C_{soil} + C_{permafrost} + C_{heterotrophs} \quad (7)$$

Land plants obtain the $CO_2$ they need for their growth from atmospheric $CO_2$, and soil and permafrost carbon growth is tied to the supply of organic carbon from land plants. In practice, $C_{land}$ is approximated without explicitly accounting for the mass of carbon in land animals (0.2PgC wildlife made up mainly of arthropods such as ants and termites, 0.1PgC livestock, and 0.06PgC human), but the much more significant microbial and fungal biomass on land (<4PgC) is implicitly included in the soil carbon inventory. Hence, heterotrophic organisms ($C_{hetertrophs}$) are important to the cycling of carbon in their ecosystems but they are within the rounding error of the other land carbon stocks (Bar-On et al., 2018).

### Atmospheric $CO_2$

Before anthropogenic carbon emissions, the atmospheric carbon reservoir ($C_{atm}$) was ~600 PgC (Fig. 1) at a concentration of 280 $CO_2$ molecules per 1 million nitrogen, oxygen and argon molecules: i.e., 280 ppm (parts per million). Excluding water vapor, the atmosphere has a total of $1.733 \times 10^{20}$ mol of molecules ($N_{atm}$ in Eq. 5). This dry atmospheric mixing ratio of $CO_2$ ($xCO_2$ in ppm units) is about 1–2% higher than $CO_2$ partial pressure and fugacity ($pCO_2$ and $fCO_2$, both in units of $\mu atm^{-1}$) at typical surface temperature, pressure and humidity. The relevant context for this natural $CO_2$ inventory is that humans have emitted ~470 PgC of

$CO_2$ from fossil fuel use and another ~5 PgC net carbon release from land (Canadell et al., 2021). $C_{atm}$ has risen by only ~295 PgC because the ocean absorbed the remainder of the emitted total (~185 Pg C), as of the global carbon budget 2022 (Friedlingstein et al., 2022).

In this view of the global carbon cycle the atmospheric $CO_2$ reservoir ($C_{atm}$) is of central importance, because it exchanges with the ocean DIC carbon reservoir ($C_{oc}$) through the sea surface, and with the land carbon reservoir ($C_{land}$) through the cell walls of plants and heterotrophs. These exchanges between surface carbon reservoirs can be considered "rapid" (Section "Closed system exchanges"), whereas the exchanges with carbon in sediments is considered "slow" and exchanges with geologic carbon are considered "very slow" (Section "Open system exchanges"). Complicating this perspective is the treatment of carbon that is chemically reactive but deeply buried in sediments; this includes deep permafrost organic carbon ($C_{permafrost}$; ~1400 PgC (Canadell et al., 2021), and old marine organic matter fermented to methane ($CH_4$ with carbon oxidation state -IV) and preserved in clathrate ice along continental margins (~2000 PgC of methane hydrates; Archer et al., 2009). Both of these natural reservoirs could be destabilized to rapidly release their carbon to the atmosphere (Archer et al., 2009; Ruppel and Kessler, 2017; Canadell et al., 2021) but they are routinely excluded from carbon cycle models because their long build-up time scale remains a challenge for simulation of the surface carbon cycle. Critically, ocean carbon cycling accounts for the vast majority of the surface carbon reservoir (Fig. 1) and hence the carbon chemistry of the ocean through time is an important research horizon.

## Carbon chemistry

Dissolved inorganic carbon (DIC) accounts for most of the ocean's vast carbon inventory ($C_{oc}$, Section "Carbon reservoirs"), and to understand the large carbon storage capacity of the ocean it is essential to realize that DIC exists in seawater in different chemical forms, but that only "dissolved $CO_2$" can exchange with the atmosphere. To relate the $CO_2$ concentration in the atmosphere to the ocean DIC inventory requires consideration of gas solubility. $CO_2$ has a low solubility ($K_0^*$) in seawater, where it hydrates to aqueous $CO_2$ and reacts with water to form carbonic acid (Eq. 1); these two DIC species are usually counted together as $H_2CO_3^*$ or $CO_2^*$ (Fig. 2). That is, with an atmospheric $CO_2$ concentration of 280 ppm we can expect only ~14 μmol/kg of $H_2CO_3^*$ dissolved in the ocean:

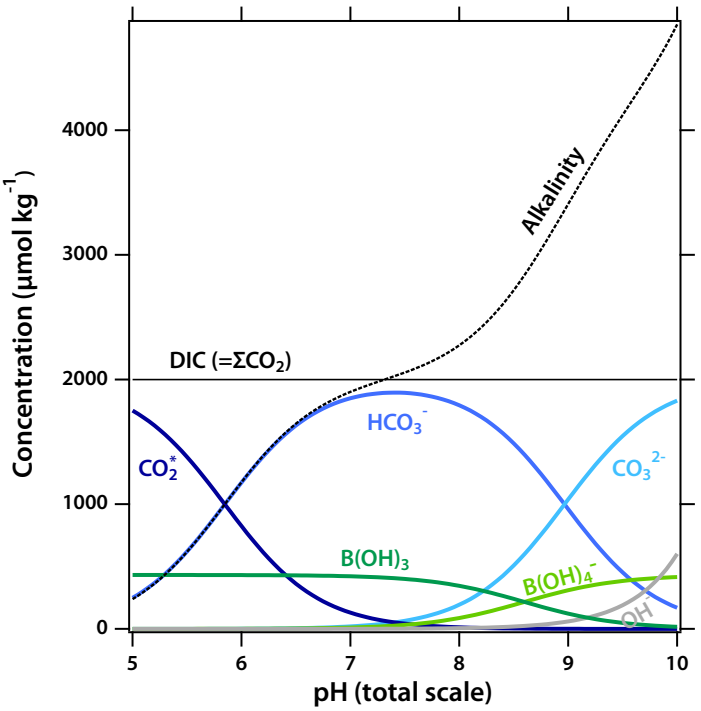


**Fig. 2** Seawater carbon speciation and pH. Typical surface seawater contains about 2000 μmol/kg of dissolved inorganic carbon (DIC) including carbonic acid and aqueous carbon dioxide ($CO_2^*$; Eq. 8), singly-deprotonated bicarbonate ion ($HCO_3^-$), and doubly-deprotonated carbonate ion ($CO_3^{2-}$; Eqs. (9)–(11)). The relative proportion of these DIC species as well as the deprotonation of boric acid ($B(OH)_3$) to borate ion ($B(OH)_4^-$) varies with pH governed by a set of stoichiometric dissociation constants (Eq. 12). The net charge of seawater must be zero (Eq. 13) and so the surplus of strong base over strong acid that exists in seawater (positive charge) is largely balanced by the deprotonation of the weak carbonic and boric acids (negative charge), a quantity defined as alkalinity (ALK; Eqs. 14 and 15; Fig. 3). In this illustration, DIC and total boron are held constant at 2000 μmol/kg and 420 μmol/kg while pH and alkalinity increase from left to right. The equilibrium constants were calculated for 25 °C and a salinity of 35 at surface pressure (Lueker et al., 2000; Dickson, 1990).

$$H_2CO_3^* = K_0^*(T)\cdot CO_2 \approx \frac{1\mu mol/kg}{20ppm}\cdot 280ppm = 14\mu mol/kg \quad (8)$$

with $K_0^*$ mainly a function of temperature and here approximated at bulk ocean temperature of about 5 °C. In $K_0^*$, the asterisk signifies that this is a stoichiometric (not thermodynamic) chemical equilibrium constant involving concentrations (not activities) of dissolved chemical species. We use stoichiometric equilibrium constants and refer to concentrations of chemical species throughout the chapter. The balance represented by Eq. (8) means that dissolved $H_2CO_3^*$ accounts for only about 1% of DIC, whereas the rest exists in the form of singly-deprotonated bicarbonate ion ($HCO_3^-$) and doubly-deprotonated carbonate ion ($CO_3^{2-}$). In Eqs. (9)–(12) that indicate the partitioning of carbon among these DIC species, $K_1^*$ and $K_2^*$ are the first and second deprotonation constants of $H_2CO_3$; $K_B^*$ is the deprotonation constant of boric acid ($B(OH)_3$) to borate ($B(OH)_4^-$); $K_w^*$ is the constant of autoprotolysis of water. The proton and oxyhydroxide concentrations ($H^+$, $OH^-$) and the constants are commonly expressed as pH, pOH and pK on a logarithmic scale of base 10:

$$HCO_3^- = H_2CO_3^* \cdot \frac{K_1^*}{H^+} \quad (9)$$

$$CO_3^{2-} = HCO_3^- \cdot \frac{K_2^*}{H^+} = H_2CO_3^* \cdot \frac{K_1^* \cdot K_2^*}{(H^+)^2} \quad (10)$$

$$DIC = H_2CO_3^* + HCO_3^- + CO_3^{2-} = K_0^* \cdot CO_2 \cdot \left(1 + \frac{K_1^*}{H^+} + \frac{K_1^* \cdot K_2^*}{(H^+)^2}\right) \quad (11)$$

$$pH = -\log H^+ = pK_2^* + \log\frac{CO_3^{2-}}{HCO_3^-} = pK_B^* + \log\frac{B(OH)_4^-}{B(OH)_3} = pK_1^* + \log\frac{HCO_3^-}{H_2CO_3^*} = pK_W^* - \log OH^- \quad (12)$$

To solve these Eqs. (9)–(12) to calculate pH and the concentration of the different DIC species (Fig. 2), we need to consider that the net charge of seawater must always be zero (Fig. 3). The $H^+$ ions are traded in every acid/base balance and therefore pH becomes the master variable describing the deprotonation of weak acids in seawater. We can think of this charge balance constraint in two different ways represented in Eqs. (13)–(15): (1) the net charge of water, $H^+$ and $OH^-$, (TOTH, in Morel and Hering, 1993) will be the sum of the net charge of all other dissolved ions (Eqs. 13 and 12) the deprotonation of the weak carbonic acid and boric acid is almost balanced by the difference between the strong bases and acids that effectively make up the salt content of seawater (Eq. 15)–this quantity is referred to as alkalinity (ALK) (Eq. 14) and measured in "equivalents of charge" per kilogram of seawater ($\mu mol_{eq}/kg$ is the product of ion charge and ion number concentration).

$$H^+ - OH^- = \sum_{charge}(anions - cations) = \sum_{H,OH}(acid - base) + HCO_3^- + 2CO_3^{2-} + B(OH)_4^- \quad (13)$$

$$ALK \equiv \sum_{H,OH}(base - acid) \approx Na^+ + 2Mg^{2+} + 2Ca^{2+} + K^+ + 2Sr^{2+} - Cl^- - 2SO_4^{2-} - NO_3^- \quad (14)$$

$$ALK \approx HCO_3^- + 2CO_3^{2-} + B(OH)_4^- \approx DIC + CO_3^{2-} + B(OH)_4^- \quad (15)$$

These formulations for ALK are slightly simplified by omitting minor species that should be included for best-practice calculations (for "total alkalinity" see Dickson, 1981; Dickson et al., 2007; Wolf-Gladrow et al., 2007; Middelburg et al., 2020). This is to highlight an eternal confusion about the two different but equivalent ways to define alkalinity: either (a) we subtract the acid-derived anion charge (~600 $mmol_{eq}/kg$) from the base-derived cation charge (~602 $mmol_{eq}/kg$) for a net positive charge of about +2350 $\mu mol_{eq}/kg$ in the bulk ocean average as defined in Eq. (14), or (b) we count the 2350 $\mu mol_{eq}/kg$ negative charge of bicarbonate, borate and carbonate ion (Eq. 15). That is, ALK is net positive (charge) but it is also often calculated as the absolute value of the negative charge of the deprotonated weak acids (Broecker and Peng, 1982)–as in Eq. (15). This is useful because it relates ALK directly to the pH and chemical speciation of the carbon and boron in seawater. Further, these formulations demonstrate a second principle of seawater chemistry that is often misunderstood: ALK is completely independent from DIC because we can easily create an artificial seawater with an ALK of 2350 $\mu mol_{eq}/kg$ by titrating 602 $mmol_{eq}/kg$ of strong base with 600 $mmol_{eq}/kg$ of strong acid, in complete absence of any carbon or boron (rendering Eq. 15 invalid). In this case, the net positive acid/base charge would be balanced by the equivalent negative TOTH charge; 2350 µmol of $OH^-$ at a pH of about 11. Likewise, we can simply bubble $CO_2$ into seawater to cause ocean acidification (increasing TOTH charge and thus declining pH) without adding any strong acid or removing any strong base.

DIC and ALK are not only independent from each other but they are also conservative, meaning that the mass of carbon and the net charge of ions are conserved and can only change if there are chemical sources or sinks, not during physical transport or mixing of seawater. Salinity is another conservative property of seawater, measured by conductivity and reported in Practical Salinity Units (Lewis and Perkin, 1981) or absolute salinity (IOC, SCOR and IAPSO, 2010), but generally referring to the grams of dissolved salts per kilogram of modern seawater (Forchhammer, 1865; Wallace, 1974). In the modern ocean the composition of dissolved salts is practically constant throughout the ocean, but the dissolved salt concentration (i.e., salinity) is higher in surface regions of net evaporation and lower in surface regions of net precipitation. That is to say, in the ocean interior there are no sinks or sources of

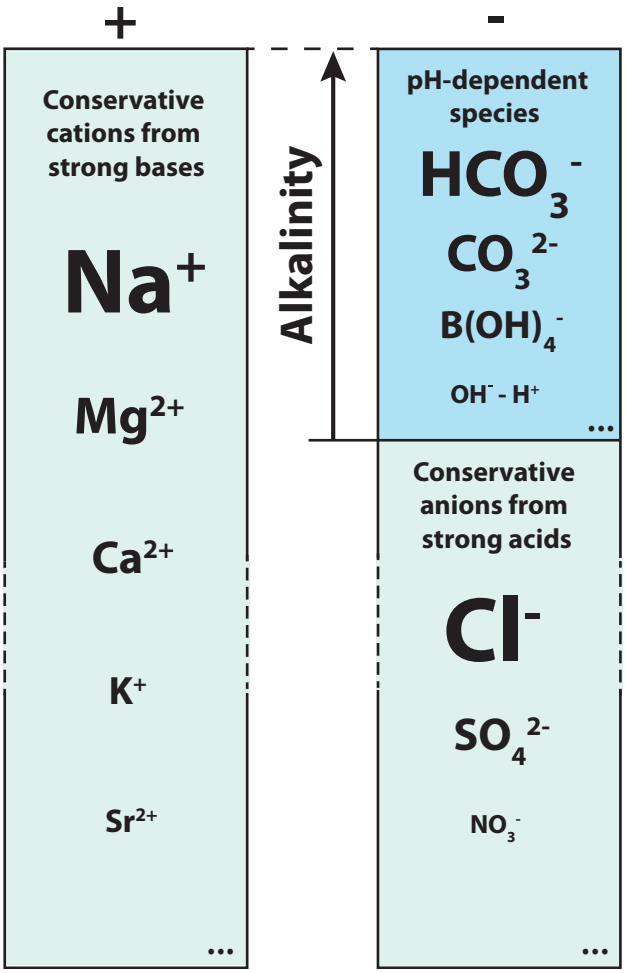


**Fig. 3** Seawater alkalinity. Alkalinity is the excess of proton acceptors over donors (vertical arrow). It can be described in two different, equivalent ways, defined as the surplus of strong base cations (alkali metals and alkaline-earth metals: $Na^+$, $Mg^{2+}$, $Ca^{2+}$, $K^+$, $Sr^{2+}$, . . .) relative to strong acid anions ($Cl^-$, $SO_4^{2-}$, $NO_3^-$, $Br^-$, $F^-$, . . .), where the ellipsis (. . .) represents trace amounts of other species in seawater (Eq. 14). This excess positive charge is exactly matched by the dissociation of weak carbonic, boric, silicic, and phosphoric acid and other weak acids that liberate protons to the solution (deprotonation) and yield negatively charged residual ions. In seawater at its natural pH, bicarbonate ion ($HCO_3^-$) is the dominant species, and including carbonate and borate ion ($CO_3^{2-}$, $B(OH)_4$) accounts for almost all of the negative charge to balance alkalinity (Eq. 15 and Fig. 2). Column heights are not to scale: in typical modern seawater strong acids and bases account for about 600,000 $\mu mol_{eq}/kg$ of charge each, with a difference of about +2250 $\mu mol_{eq}/kg$ mean ocean alkalinity and just about 5 $\mu mol_{eq}/kg$ of OH- and only about 0.006 $\mu mol_{eq}/kg$ of $H^+$ (i.e., pH of 8.22; Eq. 12).

salinity, and it can be used as a passive tracer of ocean circulation. This contrasts with DIC and ALK, which have biogeochemical sources and sinks in the ocean interior and are thus tracers of biogeochemical cycling and ocean circulation. The chemical speciation and pH of seawater is controlled by the conservative tracers (DIC, ALK, salinity) and physical conditions that are not conservative (pressure and temperature). Ocean carbon cycle models hence need to simulate all five of these factors in order to solve for carbon speciation and pH, which are not conservative. In contrast, carbon chemistry solver software (e.g., Raitzsch et al., 2021; Humphreys et al., 2021; Sharp et al., 2020) often include the option to specify any two parameters of DIC, ALK, pH, $CO_2$, $HCO_3^-$, $CO_3^{2-}$, or $CaCO_3$ saturation ($\Omega$) and solve for the remaining parameters, at specified temperature, pressure and salinity. For seawater from the geologic past it is further necessary to account for changes in the composition of dissolved salts that affect the chemical equilibrium constants (i.e., the K terms in Eqs. (8)–(12); Ben-Yaakov and Goldhaber, 1973; Millero and Pierrot, 1998; Hain et al., 2015; Clegg et al., 2023) and thereby also influence carbon speciation and pH.

Eq. (16) represents the charge balance of seawater in terms of carbonic and boric acid species–the two dominant weak acids in seawater. For instance, if we take seawater and add a small increment of base (an increase in ALK) at constant DIC, the result will be a decrease in the net charge of water (TOTH) with increased bicarbonate and boric acid deprotonation that increases the negative charge of the weak-acid anions carbonate ion and borate (from left to right in Eq. 16 and Fig. 2). The opposite will happen if strong acid is added, increasing TOTH (lowering pH) and shifting carbonate ion and borate to bicarbonate and boric acid (from right to left in Eq. (16) and Fig. 2). In both of these cases the change in $H^+$ is proportional to the shift in the speciation of

the weak acids, as shown in the definition of pH (Eq. 12). In contrast, if instead DIC is incrementally added to seawater without a change in ALK, it will come in the form of the uncharged $H_2CO_3^*$ species, most of which promptly deprotonates to bicarbonate, thereby increasing TOTH (lowering pH) and shifting carbonate and borate to bicarbonate (from right to left in Eq. 16). The opposite will happen if DIC is removed, decreasing TOTH (raising pH) and shifting bicarbonate and boric acid to carbonate ion and borate (from left to right in Eq. 16). The bicarbonate and boric acid deprotonation balances overwhelmingly compensate for ALK and DIC addition or removal to seawater with a miniscule but proportional change in the net charge of water (TOTH) that can only be expressed on the logarithmic pH scale. In other words, the presence of the partially deprotonated weak carbonic and boric acids effectively locks in a TOTH charge of about -3 µmol eq/kg that corresponds to a pH of about 8. Importantly, the principle of seawater pH-buffering by bicarbonate and boric acid deprotonation applies equally to changes in DIC and ALK, with borate ion accounting for roughly 1/3 and carbonate ion accounting for roughly 2/3 of the modern seawater buffering action per net proton release in this scenario. The fraction of proton transfers that is mediated by carbonate ion (as opposed to borate or other minor contributors) is also called the carbonate proton fraction (CPF; Hain et al., 2015):

$$\frac{2}{3}HCO_3^- + \frac{1}{3}B(OH)_3 \Leftrightarrow H^+ + \frac{2}{3}CO_3^{2-} + \frac{1}{3}B(OH)_4^- \tag{16}$$

As a consequence of this charge-balance algebra, the calculus of seawater carbonate chemistry is straightforward and described by Eqs. (17)–(19). First, ALK and DIC are independent, meaning that if one changes it has zero effect on the other because a change in DIC does not imply an addition or removal of strong acid or base and vice versa (Eq. 17). Second, for every net added amount of protons from a strong acid/base (causing equivalent reduction in the net positive acid/base charge; i.e., a decrease in ALK) or from carbonic acid deprotonation, about ⅔ of that increment are absorbed by carbonate ion reduction to produce about ⅔ bicarbonate (CPF is hence negative) (Eq. 18). Third, the incremental addition of DIC (carbonic acid $H_2CO_3^*$) raises bicarbonate by 1 for the deprotonation of that carbonic acid plus the ⅔ from the induced protonation of carbonate ion (Eq. 19; Hain et al., 2018):

$$\frac{\delta_{DIC}ALK}{\delta DIC} = \frac{\delta_{ALK}DIC}{\delta ALK} = 0 \tag{17}$$

$$CPF \equiv -\frac{\delta_{ALK}CO_3^{2-}}{\delta ALK} = \frac{\delta_{ALK}HCO_3^-}{\delta ALK} = \frac{\delta_{DIC}CO_3^{2-}}{\delta DIC} \approx -\frac{2}{3} \tag{18}$$

$$\frac{\delta_{DIC}HCO_3^-}{\delta DIC} = 1 + CPF \tag{19}$$

As a consequence of these principles of seawater carbonate chemistry, all global carbon cycle models have to track alkalinity (ALK) and total carbon concentration (DIC) separately in order to simulate the speciation of DIC and compute changes in pH (Eq. 12; see also Section "Air/sea $CO_2$ equilibration") and effective seawater $CO_2$ solubility (Eq. 11), which collectively describe the seawater carbonate system. Eqs. (8)–(19) link parameters pertaining to moles of dissolved inorganic carbon and moles of charge with equilibrium constants that vary with temperature, salinity, and pressure (T, S, and p). Knowledge of T, S, p, and at least two additional carbonate system parameters–such as concentration of ALK, DIC, carbonate ion ($CO_3^{2-}$), bicarbonate ion ($HCO_3^-$), carbon dioxide ($CO_2$), or pH–enables us to compute all of the remaining parameters.

## Carbon cycle models

There are three broad categories of carbon cycle models: (1) conceptual models that qualitatively represent causal relationships in the global cycling of carbon to reveal feedbacks and balances that arise as emergent properties through the interaction of these relationships, (2) mathematical and statistical models that seek to quantify these relationships and their interactions using algebra, calculus, logic and data, and (3) computational models that explicitly represent carbon cycle processes in space and time for computer systems to numerically simulate the operation of the global carbon cycle including its emergent feedbacks and balances. In this chapter we rely on all three categories of carbon cycle models: we use a computational model to simulate the carbon cycle response to anthropogenic carbon emissions (Figs. 4 and 5); we derive analytical solutions for the key emergent carbon cycle dynamics and their timescales to restore balance (Eqs. 22, 23, 25, 26, 45, and 56), and we communicate these dynamics with conceptual feedback diagrams (Figs. 6-9).

Numerical carbon cycle models exist in a hierarchy of increasing complexity and comprehensiveness: (1) geochemical box models, (2) Earth system models of intermediate complexity (EMICs), and (3) fully-coupled Earth System Models (ESMs). Carbon cycle box models represent the spatial distribution of carbon stocks as a set of distinct reservoirs that are assumed to be internally homogenous (i.e., each reservoir is akin to a well-mixed box). For each of these reservoirs the time rate of change of their chemical content is computed based on parameterized exchanges between reservoirs and imposed external sinks or sources (Eriksson and Welander, 1956). That is, box models rarely have more than 10 reservoirs to represent the biogeochemical cycling of carbon, whereas the physical climate and ocean circulation are typically inferred or prescribed (e.g., Keir, 1988; Toggweiler, 1999; Hain et al., 2014). This framework is flexible, computationally efficient and useful to diagnose the effect of climate and ocean circulation on the global carbon cycle (e.g., Hain et al., 2010), but climate-carbon cycle feedbacks are not simulated.

EMICs calculate ocean circulation internally by solving equations of geophysical fluid dynamics on a regular spatial grid of the ocean, but climate as a driver of ocean circulation is typically approximated (Weber, 2010). To achieve computational efficiency

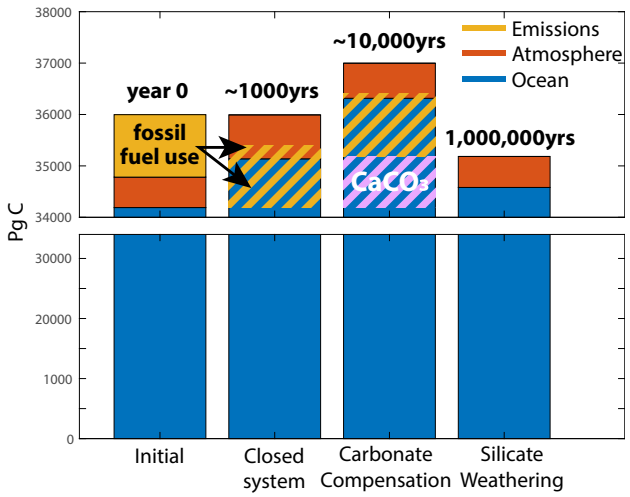


**Fig. 4** Simulated redistribution of anthropogenic carbon. Results from cGENIE experiments summarizing changes in the surface carbon budget in the long-term response to 1215 PgC of simulated anthropogenic carbon emissions from fossil fuel use. We highlight the redistribution of carbon between the atmosphere and ocean as a function of closed system feedbacks (Section "Closed system exchanges") versus open system feedbacks (Section "Open system exchanges"). 'Initial' indicates the quantity of carbon (PgC) at the start of each experiment in the atmosphere (red) and ocean (blue) as well as the quantity of carbon emitted (yellow). 'Closed system' shows the result after $10^3$ years, when the emitted carbon (yellow striping) has been redistributed from the atmosphere (red) to the ocean (blue) via ocean carbon uptake (Section "Closed system exchanges"). 'Carbonate Compensation' shows the results after $10^5$ years, when the ocean acidification from anthropogenic carbon has been neutralized by the net dissolution of $CaCO_3$ (mauve striping) so as to add to the ocean carbon inventory (blue) and draw additional anthropogenic carbon (yellow striping) from the atmosphere (red) into the ocean (blue).. 'Silicate weathering' shows the results after $10^6$ years, when most of the carbon from anthropogenic emissions has been chemically neutralized by base released during the weathering of silicate minerals, to be buried as $CaCO_3$ on the seafloor alongside the carbon from carbonate compensation. Our simulations do not include land carbon cycling (Section "Land carbon storage") or open system exchanges of organic carbon (Section "Organic carbon") and detailed results are shown in Fig. 5.

EMICs also tend to use a relatively coarse resolution ocean grid that requires parameterizations to improve the representation of transport of chemical tracers. As such, EMICs are structurally similar to geochemical box models, but with thousands of grid-cell boxes that allow for a more realistic simulation of transport of chemicals by ocean circulation. The key advantage of EMICs is that they can simulate the global carbon cycle through geologic time, with approximated climate and simplified ocean circulation.

Earth system models (ESMs) combine fully-coupled atmosphere-ocean climate models that solve the equations of motion of seawater and its transport of chemical tracers, with added representation of some biological, chemical and physical components of the Earth system. ESMs are the most complex within the hierarchy of modeling approaches because they allow for diverse networks of feedbacks between climate, ocean circulation and the global carbon cycle. By necessity, fully-coupled ESMs have higher spatial resolution of the atmosphere and ocean than EMICs in order to realistically resolve ocean-atmosphere physical interactions. Higher resolution requires high-performance computing resources and cyberinfrastructure to orchestrate simulations that rarely exceed a thousand years and are often limited to the 21st century. As such, state-of-the-art ESMs are of critical importance in anthropogenic global change research, but they are not practical tools to reconstruct carbon-climate dynamics from the geologic past.

These model categories represent points along a continuum–hybrid models exist that combine ocean box models with reactive transport models of sediments (Archer et al., 2002; Sigman et al., 1998; Zeebe, 2012) or weathering (Walker et al., 1981; Berner et al., 1983; Berner, 1990), and there are models with dynamic atmospheres that are classified as EMICs due to their relatively low resolution. Some EMICs may be more comprehensive than ESMs as their reduced resolution allows inclusion of biogeochemical Earth system processes that operate over longer timescales, e.g. methane hydrates.

## Carbon fluxes and dynamic balances

There are two conceptually different ways carbon and alkalinity move about Earth: either transported within and exchanged among the ocean, atmosphere and land biosphere, leading to no net change of the total surface inventory and hence commonly referred to as "closed-system" fluxes, or exchanged with the solid Earth rocks and sediments with net addition to or removal from the surface reservoirs by these "open-system" fluxes. In all these cases a flux refers to a quantity of carbon or alkalinity being moved or exchanged per unit time, where carbon fluxes are commonly multiplied by the molar mass of carbon to yield units of carbon weight per unit time; such as peta-gram C per year, PgC/yr (1 PgC is equivalent to $8.3 \times 10^{13}$ molC).

When we think of the global carbon cycle at the Earth system scale and through geologic time it is useful to consider not only that carbon is always in flux but also that the natural environmental balances are emergent properties of Earth and its ecosystems. These balances are revealed when we consider exchange-fluxes between distinct carbon reservoirs (Section "Carbon reservoirs"), where the

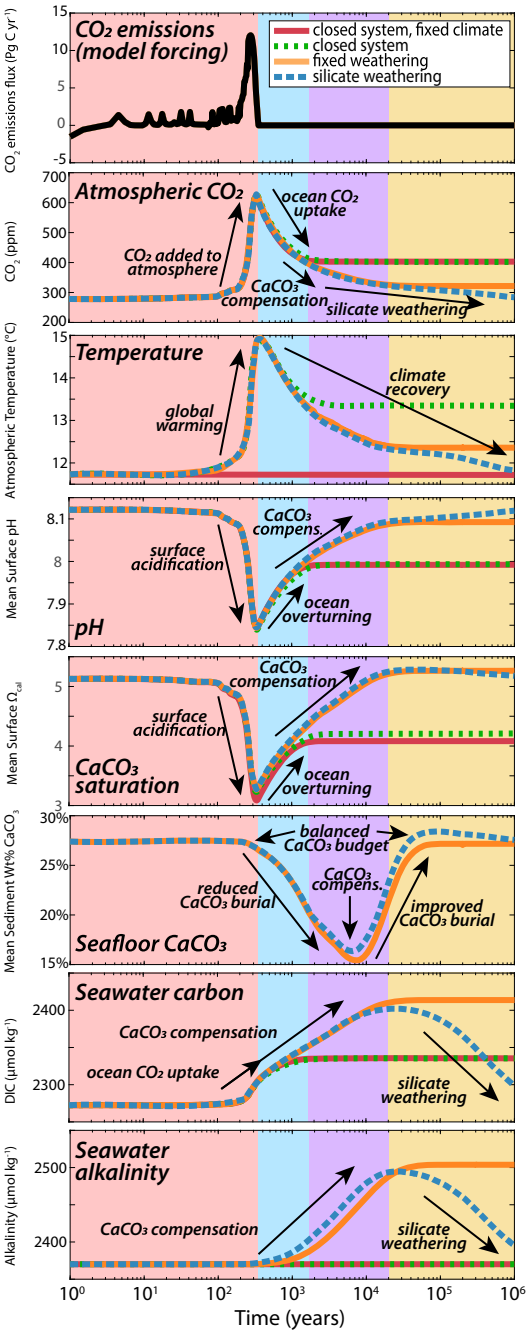


**Fig. 5** Simulated Earth System response to anthropogenic carbon. cGENIE Earth system model simulations of the response of the climate-carbon system to $CO_2$ injection as a function of the simulated feedbacks. All experiments use a simplified single-continent configuration with modern seawater chemistry and carbon emissions following the Shared Socioeconomic Pathway (SSP) 2 for a total of 1215 PgC released over 350 years. For both experiments labeled 'closed system' (red and green lines), carbon can only exchange between the ocean and atmosphere because sources and sinks of geologic carbon and alkalinity weathering and burial have been turned off (Section "Closed system exchanges"). Further, for the closed system experiment with fixed radiative forcing (red lines), the $CO_2$-climate feedback is disabled such that the release of $CO_2$ does not cause any change in temperature. The 'fixed weathering' experiment (orange lines) additionally allows for the dissolution or preservation of seafloor $CaCO_3$ - (e.g. $CaCO_3$ compensation; Section "$CaCO_3$ compensation"). The 'silicate weathering' experiment (blue lines) uses a temperature-dependent parameterization for both carbonate and silicate weathering as well as a representation of seafloor $CaCO_3$ dissolution and preservation (Section "Silicate weathering thermostat"). From top to bottom: imposed carbon emissions in units of PgC per year, atmospheric $CO_2$ (ppm), surface air temperature (°C), mean surface ocean pH, mean surface ocean saturation state with respect to calcite, mean surface sediment dry weight percentage of $CaCO_3$, mean ocean dissolved inorganic carbon (DIC) concentration in µmol/kg, and mean ocean alkalinity in $\mu mol_{eq}/kg$, . For all plots, time is on a log-scale, with closed system dynamics redistributing carbon in the surface carbon cycle on a $10^3$ year timescale (Eqs. 25 and 26), carbonate compensation mostly completed after about $10^5$ years (Eq. 45), and silicate weathering mostly completed after $10^6$ years (Eq. 56).

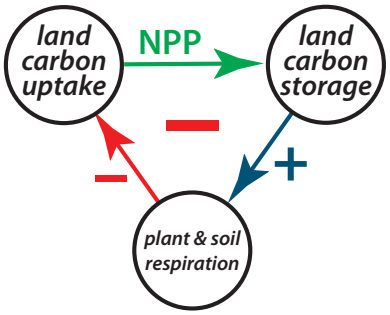


**Fig. 6** Feedback diagram of land carbon cycle. Land carbon storage is stabilized by a strong negative feedback (Section "Land carbon storage") that can be visualized using a feedback diagram, where the nodes (circles) represent fluxes or inventories, and links (arrows) represent the positive or negative effects that an increase in one node will have on the other. For example, if land plants assimilate $CO_2$ from the atmosphere through Net Primary Production (NPP) the effect will be an increase in terrestrial organic carbon biomass, i.e. land carbon storage. A larger inventory of organic carbon increases both habitat and food stock for heterotrophic organisms, thereby increasing the overall ecosystem respiration flux. An increase in total respiration reduces the net rate of land carbon uptake–where the net rate is simply the difference between NPP and respiration. That is, the initial increase in land carbon uptake by NPP leads to a reduction in land carbon uptake by respiration, a negative feedback loop symbolized by the big negative sign in the center. Hence, if there is a small imbalance between NPP and respiration (Eq. 22), the land carbon inventory and respiration rate will over time adjust to reduce the imbalance (Eq. 23). The timescale of the land carbon feedback is about 20 years, set primarily by the efficiency of heterotrophic decomposers (mainly microbes, ants, termites).

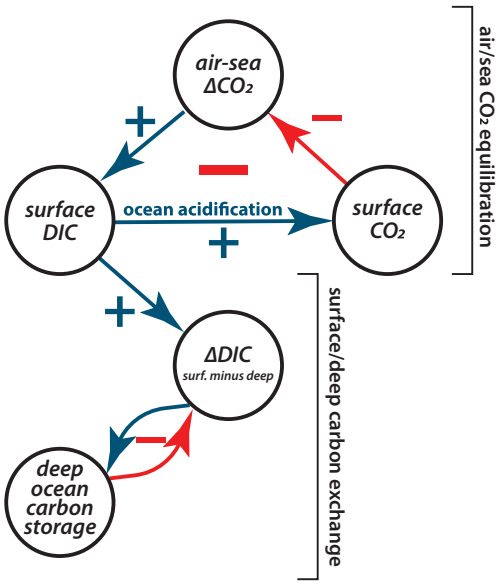


**Fig. 7** Feedback diagram of ocean/atm $CO_2$ equilibration. Two dynamics are required to understand the partitioning of $CO_2$ between the atmosphere, the surface ocean and the deep ocean interior (Section "Air/sea $CO_2$ equilibration"), one negative feedback to restore $CO_2$ balance between atmosphere and surface and another negative feedback to restore dissolved inorganic carbon (DIC) balance between the surface and deep ocean. Using anthropogenic carbon as an example, $CO_2$ emissions raise atmospheric $CO_2$ above the $CO_2$ partial pressure of surface water to create air/sea disequilibrium (positive $\Delta CO_2$) that causes ocean carbon uptake and thereby raises the DIC of the surface ocean. The increase in surface DIC causes ocean acidification that raises the $CO_2$ partial pressure of the surface seawater, which reduces the air/sea disequilibrium ($\Delta CO_2$) and thereby feeds back on ocean carbon uptake. Balance is achieved once the air-sea $CO_2$ disequilibrium is eliminated (Eq. 24), on a timescale of a few years ($\tau_{surf}$ in Eq. 25). The second feedback is activated when surface DIC increases in response to ocean carbon uptake, because new deepwater formation will carry a higher DIC concentration from the surface to be stored in the deep ocean. That is, the initial increase in surface DIC increases the DIC difference ($\Delta$DIC) between descending surface water and deepwater that is being upwelled to the surface, creating an imbalance between surface and deep ocean carbon exchange. That imbalance will over time raise deep ocean carbon storage and deep ocean DIC, acting to reduce $\Delta$DIC and the surface/deep carbon imbalance on a timescale of about 400 years ($\tau_{surf}$ in Eq. 25). Both these negative feedbacks are acting concurrently: fossil fuel emissions drive ocean acidification and atmospheric $CO_2$ rise in the short term, and deep ocean carbon uptake over the coming centuries.

change of carbon inventory stored in a given reservoir over time is simply the sum of fluxes, sources minus sinks. This framework yields three important concepts: rate of change, steady state, and turn-over timescale often referred to as "residence time."

To illustrate the difference between closed versus open system exchanges of the carbon cycle, we use a series of experiments with the intermediate complexity Earth system model cGENIE in a simplified configuration with a single continent (Vervoort et al., 2019) but modern climate and ocean chemistry (Cao et al., 2009). For all our scenarios (Section "Carbon chemistry") we simulate the response of the atmosphere and ocean to anthropogenic $CO_2$ injection using a moderate emissions scenario (Shared

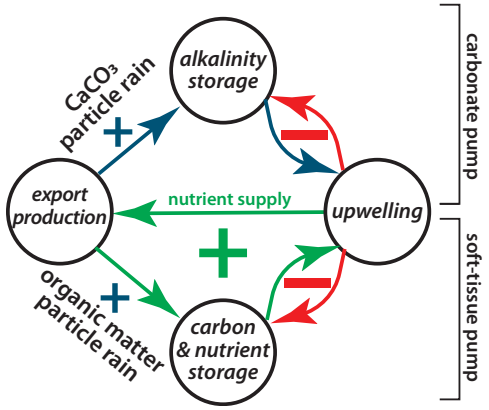


**Fig. 8** Feedback diagram of the ocean's biological carbon pumps. Biological storage of carbon and alkalinity in the ocean interior by the ocean biological pump (Section "The ocean's biological pumps") is structurally similar to carbon storage on land (Fig. 6; Section "Land carbon storage"), biological production extracts chemicals from the environment that accumulate an inventory that returns these chemicals only over time. In most of the surface ocean productivity is limited by the supply of nutrients from the upwelling of nutrient-rich water from below, which are used by phytoplankton to build soft-tissue biomass containing organic carbon and nutrient elements assimilated from the surface water, some of which is exported from the surface into the ocean interior before being respired by heterotrophs. If we consider the nutrient cycling, export production increases nutrient storage in the interior, which increases net upwelling of sequestered nutrients, which increases export production–a virtuous cycle of positive feedback that maintains the fertility of the ocean (highlighted in green). In contrast, the organic carbon that sinks to depth as soft-tissue biomass also accumulates an inventory of carbon storage ($DIC^{reg}_{OM}$ in Eq. 27), but the eventual upwelling of that carbon does not significantly affect surface productivity. Instead, upwelling of carbon sequestered by the biological pump acts as the negative feedback that balances soft-tissue export production to yield a stable inventory of biological carbon storage that is determined entirely by the total ocean inventory of limiting nutrients and the efficiency of phytoplankton to convert surface nutrients into export production (Eq. 30). This tight coupling between nutrient and organic carbon cycling is in contrast to the $CaCO_3$ inorganic carbon hard-parts produced by some plankton, a material that does not contain significant nutrients but rater two units of alkalinity (ALK) per unit of inorganic carbon. $CaCO_3$ is not a food source to heterotrophic organisms and therefore tends to dissolve back into seawater once it has reached the deep ocean seafloor, building an inventory of sequestered ALK and DIC (in a 2:1 ratio; Eqs. 27, 28, and 31). This distinction between the "soft-tissue" and "carbonate" components of the ocean's biological pump is important because biological carbon storage lowers atmospheric $CO_2$ while biological alkalinity storage raises $CO_2$.

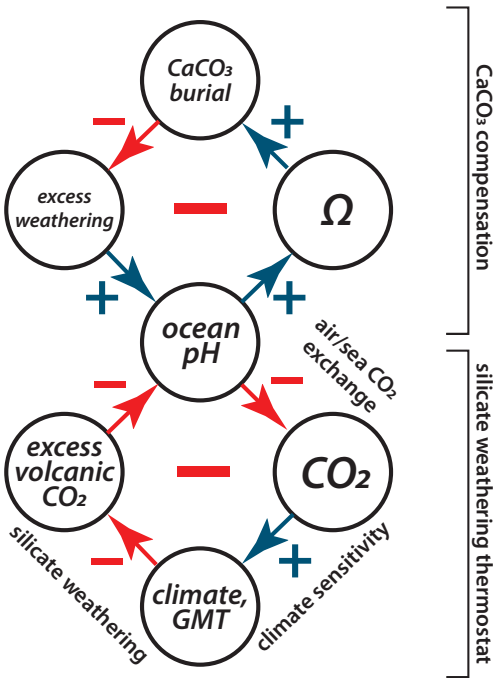


**Fig. 9** Feedback diagram of open-system carbon balances. The ocean receives the weathering products of limestone and silicate rocks and it absorbs $CO_2$ from volcanic emissions or other geologic sources, all to be balanced by burial of $CaCO_3$. Therefore, two separate negative feedbacks are required to understand the long-term Earth System carbon balance with regard to open system fluxes, one centering the ocean's alkalinity mass balance (top, see Section "$CaCO_3$ compensation") and the other balancing $CO_2$ sources with silicate weathering (bottom; see Section "Silicate weathering thermostat"). If there is more ALK supply to the ocean than ALK removal from $CaCO_3$ burial (i.e., excess weathering) the ocean will become more alkaline and seawater pH, carbonate ion concentration and $CaCO_3$ saturation state ($\Omega$) will rise (Eq. 37). An increase in $\Omega$ deepens the oceans calcite saturation horizon to expose more of the global seafloor to supersaturated conditions conducive for $CaCO_3$ burial (Eqs. 38 and 39), thereby reducing excess weathering in a negative feedback (Eqs. 40–45). In contrast, any excess of volcanic $CO_2$ emissions that is not matched by two units of ALK production by silicate weathering will accumulate (Eq. 50) so as to cause ocean acidification (lower pH) and raise atmospheric $CO_2$ (lower pH causes higher $CO_2$). Higher $CO_2$ will cause climate change and raise global mean temperatures (GMT) to accelerate silicate weathering (Eq. 49), which reduces excess volcanic $CO_2$ supply in a negative feedback (Eqs. 50–55). Both these feedbacks operate through the acid/base chemistry and carbon speciation of seawater, but on very different timescales: "carbonate compensation" stabilizes the ocean's alkalinity mass balance and deep ocean $\Omega$ with a e-folding timescale of about 4000 years (Eq. 45), whereas the "silicate weathering thermostat" stabilizes atmospheric $CO_2$ and climate on a timescale of maybe 500 thousand years (Eq. 56).

Socioeconomic Pathway, SSP 2) for emissions from 2020 to 2100 (Riahi et al., 2017) and historical emissions prior to 1990 diagnosed from combined ice core and instrumental records (Cao et al., 2009). Cumulatively, this emissions scenario corresponds to the input of 1215 Pg C over a total of 350 years (though nearly 90% of the emissions occur in the last 150 years). We conducted four simulations using the same forcing but simulation of different climate and carbon cycle feedbacks representing both closed and open system exchanges. Each of these simulations was computed for a total of one million years upon $CO_2$ emissions. Below we use these illustrative experiments to introduce the significance of closed versus open system dynamics in determining the fate of emitted carbon.

## Closed system exchanges

Carbon exchange between the ocean, atmosphere and land biosphere can repartition carbon among these reservoirs, but the total amount of carbon summed across these reservoirs is conserved and hence stays constant (Eq. 20), as does the ocean's alkalinity inventory (Eq. 21). This closed-system perspective on the global carbon cycle (Eriksson and Welander, 1956) represents the two primary balances governing land and ocean carbon storage.

$$\frac{\delta}{\delta t}C_{total} = \frac{\delta}{\delta t}C_{oc} + \frac{\delta}{\delta t}C_{land} + \frac{\delta}{\delta t}C_{atm} = 0 \tag{20}$$

$$\frac{\delta}{\delta t}\overline{ALK} = 0 \tag{21}$$

In response to $CO_2$ injection to the atmosphere, closed system exchanges will redistribute this $CO_2$ among the ocean, land, and atmosphere (orange in Fig. 1), but the sum of carbon across these reservoirs will simply equal the initial total plus the emitted mass of carbon in $CO_2$ (see Fig. 4). Two illustrative closed system experiments using cGENIE indicate this repartitioning (see Fig. 5, green and red lines). In the experiment 'closed system fixed climate' feedbacks between $CO_2$ and climate are disabled such that the injection of atmospheric $CO_2$ causes no change in temperature (i.e., climate sensitivity to $CO_2$ is turned off ). The experiment 'closed system' is identical except with the $CO_2$-climate feedback enabled. Comparison of these two experiments illustrates that the partitioning of carbon between the atmosphere and oceans via closed system exchanges is largely independent of the greenhouse effect on climate, with full ESM models better equipped to address the questions than out EMIC results (see Section "Carbon chemistry"). Further, our closed system experiments exclude land carbon storage (Section "Land carbon storage") but include both sets of exchanges that describe the partitioning between atmosphere and ocean carbon–air/sea equilibration (Section "Air/sea $CO_2$ equilibration") and the ocean's biological carbon pumps (Section "The ocean's biological pumps").

### *Land carbon storage*

Land plants assimilate about 120 PgC/yr from the atmospheric $CO_2$ inventory (Gross Primary Production, GPP) but they respire about half of that organic carbon back to $CO_2$ to yield about 60 PgC/yr of Net Primary Production (NPP) of terrestrial organic carbon that constitutes the base of the terrestrial food web (Gough, 2011). Our best estimates of current soil respiration by microbes, millipedes, beetles, earthworms, termites, ants and other edaphic fauna is about 90 PgC/yr (Bond-Lamberty, 2018; Caiafa et al., 2023), suggesting either that existing GPP, NPP and soil respiration estimates need to be revised to yield a balanced land carbon budget (Jian et al., 2022) and/or that ongoing global warming has accelerated soil respiration (e.g., Nissan et al., 2023). Wildfires are thought to burn about 2 PgC/yr (Jones et al., 2019) and rivers carry about 2 PgC/yr of organic carbon to the ocean (Tian et al., 2023). Estimates based on the current atmospheric $CO_2$ budget suggest that human land-use change removes about 1 PgC/yr from the land surface while existing biomes absorb 3 PgC/yr from the atmosphere (Friedlingstein et al., 2022), to yield a roughly 3% surplus between NPP as the source of land carbon versus respiration and disturbance as the sinks–this imbalance represents ongoing net land carbon uptake (LCU) or the land sink. Given the mass of the land carbon reservoir, the entire land carbon stock turns over with an average residence time of only 30 to 40 years ($\tau_{land}$). The answer to how land carbon storage changes will contribute to atmospheric $CO_2$ change in the near future is constrained by uncertainty over how humans decide to use the land surface, how ecosystems respond to climate and environmental change (e.g., Joos et al., 2001), and also the combined physiological plant response to higher $CO_2$ and temperature (Fatichi et al., 2019). General insight can be gained by assuming NPP and residence time as constant and expressing the land carbon imbalance as an inhomogeneous differential equation (Eq. 22, Fig. 6). In this simplified case the solution to the homogeneous differential equation (Eq. 23) equals the steady state land carbon inventory ($C^{ss}_{land}$) plus and an initial deficit/surplus ($\Delta C_0$) of land carbon relative to the steady state inventory that will be resolved over time (t) by land carbon uptake (LCU) with an e-folding timescale of $\tau_{land}$.

$$\frac{\delta}{\delta t}C_{land} = F_{l.NPP} - F_{l.resp} = F_{l,NPP} - \frac{C_{land}}{\tau_{land}} = LCU \tag{22}$$

$$C_{land}(t) = C^{ss}_{land} + \Delta C_0 \cdot e^{-\frac{t}{\tau_{land}}} = \tau_{land} \cdot \left(F_{l.NPP} + LCU_0 \cdot e^{-\frac{t}{\tau_{land}}}\right) \tag{23}$$

That is, a positive/negative imbalance in the land carbon inventory will over time increase/decrease land carbon storage and soil respiration–in both cases progressively reducing the initial imbalance to yield the steady state land carbon inventory. This negative feedback (Fig. 6) acts to stabilize the land carbon inventory through geologic time. For the purpose of this chapter we will set aside

this important topic because balances other than that of land carbon appear to regulate atmospheric $CO_2$ and climate on timescales longer than centuries (Sarmiento and Bender, 1994; Stocker, 2015), as described below.

### Air/sea $CO_2$ equilibration

Atmospheric $CO_2$ spontaneously dissolves into ocean surface water at a rate of about 80 PgC/yr ($F_{invasion}$) counterbalanced by surface ocean exsolution of $H_2CO_3^*$ ($F_{evasion}$), as determined by seawater carbon chemistry (Section "Carbon cycle models"). At this rate, air/sea gas exchange replaces atmospheric $CO_2$ every 7 or 8 years and the combined atmosphere and land carbon reservoirs every about 40 years (Bolin, 1960; Naegler and Levin, 2006). Ongoing anthropogenic carbon release to the atmosphere is elevating atmospheric $CO_2$ relative to the surface ocean, thereby causing a surplus of $CO_2$ invasion over evasion that leads to net ocean carbon uptake (OCU, Eq. 24) currently estimated at about 2 to 4 PgC/yr (Watson et al., 2020; Gruber et al., 2023). The gas transfer velocity (k) applicable to the global ocean has been estimated at about 70,000 mol/m$^2$/yr/atm (Broecker et al., 1985, 1986; Cember, 1989; Wanninkhof, 1992; Sarmiento and Gruber, 2006), such that preindustrial $CO_2$ of 280 ppm yields a gross invasion flux of 6 PmolC/yr (80 PgC/yr) and net ocean carbon uptake (OCU) of 3 PgC/yr (0.25 PmolC/yr) and yields a corresponding air/sea disequilibrium ($\Delta CO_2$) of only 10 ppm (equivalent to 21 PgC). That is, $CO_2$ exchange between the atmosphere and global surface ocean is sufficiently rapid to maintain approximate $CO_2$ equilibrium at the sea surface.

$$\frac{\delta}{\delta t}C_{oc} = (F_{invasion} - F_{evasion}) = k \cdot A_{oc} \cdot \Delta CO_2 \approx k \cdot A_{oc} \cdot \left(\frac{C_{atm}}{N_{atm}} - \frac{C_{surf}}{M_{surf}} \cdot \frac{H^+}{K_0^* \cdot K_1^*}\right) = OCU \tag{24}$$

In contrast to the surface ocean, the ocean interior cannot directly exchange $CO_2$ with the atmosphere. Instead, seawater is transported by the physical circulation of the ocean, thereby redistributing DIC and ALK globally. That is, ocean circulation acts against DIC and ALK gradients within the ocean, such that over time a balance is achieved between the rates of DIC and ALK sinking from the surface into the interior and the DIC and ALK transport by interior waters upwelled to the surface (Fig. 7). However, circulation can be relatively slow; the ocean mixing time is on the order of $10^3$ years for distributing carbon between the surface and interior ocean. Ocean carbon cycle models have been used to constrain the decline of OCU as atmosphere and ocean re-equilibrate after an imposed $CO_2$ pulse to the atmosphere, with broad agreement between different models that there are three separate timescales of ocean carbon uptake, represented by Eq. (25) (Joos et al., 2013): (1) a 4-year timescale ($\tau_{surf}$) of surface ocean air/sea equilibration via gas exchange, (2) a roughly 40-year timescale ($\tau_{upper}$) of carbon uptake by the shallow subsurface and thermocline by upper ocean geostrophic circulation, and (3) a roughly 400-year timescale ($\tau_{deep}$) for the entire upper ocean to be turned over by deep upwelling and new deep water formation:

$$CO_2(t)_{atm} = CO_2^{initial} + \Delta CO_2^{pulse} \cdot \left(0.2 + 0.3 \cdot e^{-t/\tau_{surf}} + 0.3 \cdot e^{-t/\tau_{upper}} + 0.2 \cdot e^{-t/\tau_{deep}}\right) \tag{25}$$

$$CO_2\,(t > 1000 years)_{atm} = CO_2^{initial} + 0.2 \cdot \Delta CO_2^{pulse} \tag{26}$$

To understand the consequences of gas exchange, surface carbon chemistry and ocean circulation, it is useful to consider that it takes about 6 PgC to raise atmospheric $CO_2$ by 1% (from 280 to 283 ppm); it takes about 2 PgC to raise surface ocean $CO_2$ by 1%, and it takes about 38 PgC to raise bulk ocean $CO_2$ by 1%. That is, adding 8 PgC $CO_2$ (100%) to the atmosphere will drive 2 PgC carbon uptake by the modern surface ocean proceeding over the course of a decade (25%), but it will ultimately drive about 6.4 PgC carbon uptake by the bulk ocean (80%) proceeding over the course of about one thousand years (Eqs. 25 and 26; Maier-Reimer and Hasselmann, 1987; Joos et al., 2013). Hence, when allowing for about 1000 years of equilibration, 6.4-out-of-8 added carbon atoms will be stored in the ocean and 1.6-out-of-8 will remain in the atmosphere. This steady state partitioning of added carbon between ocean and atmosphere is generally applicable to estimate the persistent $CO_2$ change for any perturbation that causes a short-term disequilibrium (Hain and Sigman, 2024), although the exact value of partitioning applies to the modern ocean and has likely changed through geologic time (Hain et al., 2015). For example, warming the bulk ocean by 1 °C initially raises ocean $CO_2$ by about 4% to create a 11 ppm disequilibrium, which then drives about 20 PgC of ocean $CO_2$ release to the atmosphere. During $CO_2$ release the ocean $CO_2$ declines by 0.6% (for a net change of +3.4%) and atmospheric $CO_2$ increases by 3.4% to eliminate the disequilibrium and establish a new steady state partitioning of $CO_2$ between the ocean and atmosphere.

In our illustrative cGENIE closed system experiments (both 'closed system' and 'closed system fixed climate'), the final value of atmospheric $CO_2$ (achieved in the light blue shaded region in Fig. 7) reflects the air-sea equilibration while the time at which this value is achieved reflects the full equilibration timescale ($\tau_{deep}$). Compared to a starting atmospheric $CO_2$ of 280 ppm, the equilibrium $CO_2$ following injection of 1215 Pg C is 400 ppm. This change in concentration corresponds to an excess of 263 Pg C in the atmosphere, which is ~22% of the emitted total. The final atmospheric $CO_2$ concentration is reached after about 1000 years, consistent with the 400-year e-folding time-scale of deep ocean overturning (Joos et al., 2013; Lord et al., 2016).

### The ocean's biological pumps

Biological production in the ocean surface converts DIC to organic matter and $CaCO_3$ that can sink into the ocean interior, thereby causing biological carbon sequestration (Sigman and Hain, 2013). When addressing the role of biology in regulating ocean and atmospheric $CO_2$, it is important to account for the carbon and alkalinity sequestered by this biological "pumping" away from the ocean surface and into the interior, i.e., the steady state inventories of regenerated DIC and ALK held in the ocean interior (Fig. 1; Eq. 6). Regenerated DIC and ALK, from the respiration of organic matter and dissolution of $CaCO_3$, are much smaller proportions

of the total ocean DIC and ALK inventories than the preformed components carried into the ocean interior by circulation and mixing (Section "Carbon reservoirs", Eq. 6). Assuming a constant total inventory (i.e., a closed system), we can directly relate changes in the preformed inventories to changes in the regenerated inventories from water column organic matter (OM) respiration and from export $CaCO_3$ dissolution (Eqs. 27–29). Further, we know that $CaCO_3$ contains two units of alkalinity per unit of carbon and we assume classical values for the element stoichiometry of typical marine biomass (Redfield, 1934; Redfield et al., 1963)–106 units of carbon and 18 units of acidity (i.e., negative alkalinity) per unit of phosphorous (P):

$$\Delta DIC_{pref} = -\Delta DIC_{reg}^{OM} - \Delta DIC_{reg}^{CaCO_3} \tag{27}$$

$$\Delta ALK_{pref} = -\Delta ALK_{reg}^{OM} - \Delta ALK_{reg}^{CaCO_3} = \frac{18}{106} \cdot \Delta DIC_{reg}^{OM} - 2 \cdot \Delta DIC_{reg}^{CaCO_3} \tag{28}$$

$$\Delta P_{pref} = -\Delta P_{reg}^{OM} = -\frac{\Delta DIC_{reg}^{OM}}{106} = \frac{\Delta ALK_{reg}^{OM}}{18} \tag{29}$$

To understand the operation of the biological pump (Fig. 8) it is useful to consider that regenerated DIC, ALK and P are continuously added to by biological export from the surface and subsequent respiration and dissolution, while the only loss term comes from ocean circulation returning them to the surface. That is, an increase in biological export tends to increase while a speedup of ocean circulation tends to decrease DIC, ALK and P storage by the biological pump, but in any case a balance between sources and sinks is eventually established with a timescale ($\tau_{circ}$; Eqs. 30 and 31). For example, if we were to suddenly switch off biological export it would take roughly 1000 years (about two e-folding timescales of deep ocean overturning, as in Section "Air/sea $CO_2$ equilibration") for DIC, ALK and P to return to the surface so that the regenerated inventories approach a steady state value of zero, and if we were to switch biological export back on it would again take roughly 1000 years for nutrients to cycle to the surface and be utilized by phytoplankton to yield new stable inventories of regenerated DIC, ALK and P. One key difference between the organic matter and carbonate pumps is that organic matter (OM) export is rapidly respired as it sinks through the water column, such that there is a relatively shallow remineralization depth of organic carbon and nutrients, whereas up to half of the particulate $CaCO_3$ exported from the surface ocean only dissolves after it has reached the deep ocean seafloor (Sulpis et al., 2018). As such, the efficiency of the global "soft-tissue" pump can be measured as the fraction of total nutrients used for carbon sequestration ($P_{reg}$ over $P_{total}$; Ito and Follows, 2005; Marinov et al., 2008a,b), whereas the inventory of regenerated $CaCO_3$ is decoupled from nutrient cycling and rather depends on the rate of deep ocean $CaCO_3$ dissolution and the timescale of deep ocean overturning circulation ($\tau_{circ}^{CaCO3}$; Hain et al., 2010, 2014; Kwon et al., 2011).

$$\frac{\delta DIC_{reg}^{OM}}{\delta t} = \frac{F_{export}^{OM}}{M_{oc}} - \frac{DIC_{reg}^{OM}}{\tau_{circ}^{OM}} \tag{30}$$

$$\frac{\delta ALK_{reg}^{CaCO_3}}{\delta t} = \frac{F_{dissolution}^{CaCO_3}}{M_{oc}} - \frac{ALK_{reg}^{CaCO_3}}{\tau_{circ}^{CaCO_3}} \tag{31}$$

If biological carbon storage in the ocean interior was to somehow increase by 100 PgC it would reduce the preformed ocean carbon inventory by that amount, driving a 2.8% reduction of ocean $CO_2$ and causing about 8 ppm disequilibrium with the atmosphere. This initial disequilibrium is resolved by about 14 PgC ocean $CO_2$ uptake resulting in 2.4% steady state atmospheric $CO_2$ lowering. Likewise, if the biogenic rain of $CaCO_3$ from the surface sequesters an additional 100 PgC in the interior (8.3 PmolC with 16.6 Pmol of alkalinity; ΔALK is exactly double ΔDIC) the reduction in preformed DIC would lower ocean $CO_2$ by 2.8% while the reduction in preformed ALK would raise ocean $CO_2$ by about 5%, for a net 2.2% ocean $CO_2$ increase (+6 ppm) that results in 1.9% (+5 ppm) steady state atmospheric $CO_2$ rise after equilibration is complete.

$$\delta \ln CO_2 \approx -\frac{6.4}{8} \cdot \delta \ln CO_3^{2-} = \frac{6.4}{8} \cdot \left[\frac{-CPF}{CO_3^{2-}} \cdot \left(\Delta DIC_{reg}^{OM} - \Delta ALK_{reg}^{OM} + \Delta DIC_{reg}^{CaCO_3} - \Delta ALK_{reg}^{CaCO_3}\right)\right]^{-1} \tag{32}$$

$$CO_2 \simeq CO_2^{initial} \cdot e^{\frac{-0.002}{\mu mol/kg} \cdot \left(\frac{106+18}{106} \cdot \Delta DIC_{reg}^{OM} + \frac{1-2}{1} \cdot \Delta DIC_{reg}^{CaCO_3}\right)} \tag{33}$$

Finally, the steady state $CO_2$ effect of any combination of closed-system carbon cycle changes can be estimated in the same way, following Eqs. (32) and (33). For example, if land carbon storage declines to release 100 PgC to the atmosphere (+47 ppm atmospheric $CO_2$) and biological carbon sequestration in the ocean increases by 100 PgC (−8 ppm bulk ocean $CO_2$) the resulting 55 ppm disequilibrium will resolve by 100 PgC net ocean carbon uptake (OCU) that reduces atmospheric $CO_2$ by 47 ppm and raises ocean $CO_2$ by 8 ppm. Hence, after equilibration there will be no net change in steady state $CO_2$ but rather a 100 PgC net transfer of carbon from land to the ocean–changes in biological carbon storage on land and in the ocean have equivalent effects on atmospheric $CO_2$ and can compensate for each other.

In our illustrative cGENIE experiments, the closed system experiment with fixed climate partially separates the relative impact of air-sea equilibration and the biological pump on the evolution of atmospheric $CO_2$ following anthropogenic emissions. Without a change in temperature, $CO_2$ forcing in this experiment (Fig. 5, red lines) produces no change in ocean circulation or in export productivity (given the simplified, nutrient-only representation of export; Ridgwell et al., 2007). The maximum increase in atmospheric $CO_2$ is 18 Pg C less than in the closed system experiment with a $CO_2$-climate feedback (Fig. 5, green lines).

The differences in air-sea gas exchange between these experiments (~0.2 PgC/yr) are less significant than the difference in export productivity (~0.6 PgC/yr), suggesting that the majority of the (minor) difference between these experiments is due to the impact of changes in the modeled biological pump. Reduced export production (due to a temporary stratification-induced reduction in surface nutrient availability) in the closed system experiment with a $CO_2$-climate feedback leaves a larger fraction of the emitted $CO_2$ in the atmosphere. However, when it comes to our cGENIE experiments of anthropogenic $CO_2$ release to the atmosphere, the similarity between experiments with and without climate feedback illustrates that the immediate dynamic of air-sea equilibration is relatively more important than induced feedbacks operating through changes in carbon storage by the biological pump. These climate/carbon cycle feedbacks are key uncertainties highlighted in the 6th IPCC Assessment Report (IPCC, 2021).

## Open system exchanges

Open system exchanges describe the balance between carbon addition and removal from the surface carbon reservoir ($C_{oc}$ + $C_{atm}$ + $C_{land}$) with the solid Earth (sediments and rocks). In other words, in closed-system scenarios (Section "Closed system exchanges"), the sum of surface carbon did not change. In open-system exchanges, that sum can change. Carbon is added to the surface via weathering, reaction with sediments, and volcanic emissions, and removed through sedimentary burial and alteration of oceanic crust. Both carbonate and silicate weathering act to transform $CO_2$ into bicarbonate ions, but since the formation of calcium carbonate also releases $CO_2$, only silicate weathering represents a net conversion of $CO_2$ into calcium carbonate. That is, carbonate weathering ($F_{CW}$) and volcanic emissions ($F_{volc}$) are sources of carbon; carbonate weathering and silicate weathering ($F_{SW}$) are sources of alkalinity, and both net sources are balanced by carbonate burial ($F_{CB}$) (Eqs. 34 and 35). While organic carbon weathering ($F_{OCW}$) and organic carbon burial ($F_{OCB}$) are also open system fluxes, we do not represent either process in our illustrative open system cGENIE experiments and reserve discussion until Section "Organic carbon."

$$\frac{\delta}{\delta t}(C_{oc} + C_{atm} + C_{land}) = F_{CW} - F_{CB} + F_{volc} \tag{34}$$

$$\frac{\delta}{\delta t}\overline{ALK} \cdot M_{oc} = 2F_{CW} - 2F_{CB} + F_{SW} \tag{35}$$

Critical to our understanding of the open-system global carbon cycle is the recognition that two negative feedback dynamics are needed to maintain the mass balances of alkalinity and carbon. The first dynamic of "$CaCO_3$ compensation" primarily maintains the ocean's $CaCO_3$ saturation mainly via the alkalinity mass balance (Section "$CaCO_3$ compensation"), whereas the second dynamic of the "silicate weathering thermostat" primarily maintains equable climates via the carbon mass balance (Section "Silicate weathering thermostat"). Our illustrative cGENIE experiments include two open system simulations that represent carbonate and silicate weathering and carbonate burial ("fixed weathering" and "silicate weathering").

### *$CaCO_3$ compensation*

The largest loss term of alkalinity from seawater is biologically controlled $CaCO_3$ precipitation in the surface ocean, both by organisms living on the shallow seafloor such as corals, mollusks and algae (~1.3–1.7 PgC/yr) and by plankton suspended in the surface layer of the open ocean (~0.8–1.4 PgC/yr) (Milliman, 1993; Jin et al., 2006; Wood et al., 2023). The $CaCO_3$ produced by these organisms can have two different fates: either it is recycled and dissolves back into seawater to yield zero net change in mean ocean alkalinity, or it is preserved on the seafloor to be buried and thereby lost from the ocean. For every carbon atom buried as $CaCO_3$ the ocean also loses one doubly charged calcium cation representing two units of alkalinity; reflecting the strict 2:1 ALK-to-DIC ratio of all carbonate minerals. That is, carbonate precipitation removes carbonate ion from seawater driving incremental deprotonation of bicarbonate ion so as to raise $H^+$ (lower pH) and thereby raise $CO_2$ (Eq. 36, from left to right), whereas the reverse reaction of $CaCO_3$ dissolution raises the pH (Eq. 36, from right to left):

$$Ca^{2+} + HCO_3^- \Leftrightarrow CaCO_3 + H^+ \text{ (see also equation \#3)} \tag{36}$$

Current estimates (Wood et al., 2023 and references therein) suggest that roughly 1 PgC/yr of neritic $CaCO_3$ is buried on the continental shelf (10% of seafloor area), and roughly 1 PgC/yr pelagic $CaCO_3$ is buried on the continental slope and mid-ocean ridges (<3.5 km; 20% of seafloor). There is almost zero $CaCO_3$ preservation on the deep abyssal seafloor (>3.5 km; 70% of seafloor). By inference this suggests that the majority of $CaCO_3$ production is recycled within the ocean, yielding no net change in mean ocean alkalinity. Moreover, the dramatic change in burial efficiency for pelagic $CaCO_3$ on deep seafloor (often referred to as lysocline, or the depth where sediments begin to show evidence of dissolution) is closely related to (but slightly deeper than) the calcite saturation horizon (CSH) – the transition in the water column from oversaturation ($\Omega > 1$) to undersaturation ($\Omega < 1$) of calcite (Eq. 37), the polymorph of $CaCO_3$ that comprises most of the pelagic $CaCO_3$ rain from the open ocean surface:

$$\Omega = \frac{Ca^{2+} \cdot CO_3^{2-}}{K^*_{sp}(z)} \tag{37}$$

That is, for every 1% increase in mean ocean carbonate ion ($\delta \ln CO_3^{2-} = 0.01$) the saturation of the deep ocean will also increase by 1% at any given depth ($d\ln\Omega|z = 0.01$), such that the water depth ($z$) at which calcite is at saturation ($\Omega_c = 1$; CSH) changes proportionally to the depth dependence of pressure-dependent calcite solubility constant ($\delta K/(K^* \delta z)$) (Eq. 38). Further, because of

the hypsometry of the ocean (the area of seafloor above a given water depth, A(z)) the seafloor area bathed in oversaturated ($\Omega > 1$) bottom water will increase by about 13 million km$^2$ for every 100 m increase in the CSH ($\delta A/\delta CSH$). This additional seafloor area increment ($\delta A$) is then projected to increase the deep sea $CaCO_3$ burial flux (Eq. 39).

$$\delta CSH = \left(\frac{\delta K^*_{sp}}{K^*_{sp} \cdot \delta z}\right)^{-1} \cdot \delta \ln \Omega|_{z=const.} = \left(\frac{\delta K^*_{sp}}{K^*_{sp} \cdot \delta z}\right)^{-1} \cdot \delta ln CO_3^{2-} \tag{38}$$

$$\delta F_{CB} \approx \frac{F^{pelagic}_{CaCO3}}{A_{oc}} \cdot \delta A = \frac{F^{pelagic}_{CaCO3}}{A_{oc}} \cdot \frac{\delta A}{\delta z} \cdot \delta CSH = k_{CSH} \cdot \delta CSH \tag{39}$$

where $k_{CSH}$ is the sensitivity of $CaCO_3$ burial to CSH change assuming modern average pelagic $CaCO_3$ sinking flux over the total area of the open ocean (F/A). It is this sensitivity of carbonate burial to the ocean's $CaCO_3$ saturation state ($\Omega$) that acts to reduce the imbalance between weathering and $CaCO_3$ burial ($I_{CaCO3}$) (Eq. 40). For example, if there was some initial imbalance (Eqs. 41 and 42) then we would expect that imbalance to decline as mean ocean carbonate ion concentration ($\ln CO_3$), ocean $CaCO_3$ saturation ($\ln\Omega$) and CSH all increase over time to expose more area seafloor ($\delta A$) to oversaturated bottom water ($\Omega > 1$):

$$I_{CaCO3} = F_W - F_{CB} \tag{40}$$

$$\delta I_{CaCO3} = -k_{CSH} \cdot \delta CSH = -k_{CSH} \cdot \left(\frac{\delta K^*_{sp}}{K^*_{sp} \cdot \delta z}\right)^{-1} \cdot \delta ln CO_3^{2-} \tag{41}$$

$$\frac{\delta CO_3^{2-}}{\delta t} = -CPF \cdot \frac{I_{CaCO3}}{M_{oc}} \Leftrightarrow \frac{\delta ln CO_3^{2-}}{\delta t} = -CPF \cdot \frac{I_{CaCO3}}{CO_3^{2-} \cdot M_{oc}} = \left(\frac{\delta K^*_{sp}}{K^*_{sp} \cdot \delta z}\right) \cdot \frac{\delta CSH}{\delta t} \tag{42}$$

As such, any initial imbalance ($I_0$) that might exist in the Earth System will exponentially decline over time as the CSH adjusts to match $CaCO_3$ burial to weathering. That is, for every increment of time ($\delta t$) that some imbalance exists, the imbalance will decline by a set percentage ($\delta I/I$) (Eq. 43), such that it asymptotes toward zero with a characteristic e-folding timescale ($\tau_{CaCO3}$), the timescale of carbonate compensation (Eqs. 44 and 45; top of Fig. 9):

$$\frac{\delta I_{CaCO3}}{I_{CaCO3}} = \delta ln I_{CaCO3} \approx \frac{CPF \cdot k_{CSH}}{CO_3^{2-} \cdot M_{oc} \cdot \left(\frac{\delta K^*_{sp}}{K^*_{sp} \cdot \delta z}\right)} \cdot \delta t \tag{43}$$

$$I_{CaCO3}(t) = I_0 \cdot e^{\frac{-t}{\tau_{CaCO3}}} \tag{44}$$

$$\tau_{CaCO3} = \frac{CO_3^{2-} \cdot M_{oc} \cdot \left(\frac{\delta K^*_{sp}}{K^*_{sp} \cdot \delta z}\right)}{-CPF \cdot k_{CSH}} = \frac{CO_3^{2-} \cdot M_{oc} \cdot \left(\frac{\delta K^*_{sp}}{K^*_{sp} \cdot \delta z}\right)}{-CPF \cdot \frac{F^{pelagic}_{CaCO3}}{A_{oc}} \cdot \frac{\delta A}{\delta z}} \approx 4000\ years \tag{45}$$

The process of carbonate compensation is reflected in our open system cGENIE simulation with fixed weathering (Fig. 5, orange lines). This experiment simulates both the dissolution and preservation of carbonate in seafloor sediments as a function of evolving seawater chemistry but maintains a fixed supply of alkalinity via weathering set at the flux required to maintain an open system steady state prior to carbon injection. In contrast to the closed system equilibrium $CO_2$ concentration of 400 ppm, atmospheric $CO_2$ after carbonate compensation is 322 ppm. Carbonate compensation thus absorbs nearly ⊠ of the excess carbon left in the atmosphere after closed-system equilibration between ocean and atmosphere. The open system response to $CO_2$ release is to neutralize the added carbon with net $CaCO_3$ dissolution in a ~1:1 ratio to yield a total addition of DIC and ALK in an approximately ~1:1 ratio with about half of the DIC from the $CO_2$ release and half from the carbonate compensation. In other words, compared to the closed system experiments, the increase in DIC concentration is approximately doubled (in a closed system [DIC] increases by 63 μmol/kg but with carbonate compensation [DIC] increases by an additional 79 μmol/kg). The combined ocean-atmosphere inventory grows by ~1000 PgC more than the quantity of carbon emitted, reflecting the input of carbon via carbonate dissolution (Fig. 4).

To yield a balanced ocean alkalinity budget, $CaCO_3$ production must equal the sum of dissolution and burial, and $CaCO_3$ burial is balanced by an equivalent alkalinity flux originating from weathering reactions of rock formations (though other fluxes such as submarine weathering and anaerobic processes may also play a minor role; Middelburg et al., 2020). If there happens to be an imbalance between weathering and burial (as in our fixed weathering cGENIE experiment) we would expect the calcite saturation of the ocean to adjust to the level where burial matches the weathering flux. For example, if $F_{burial}$ is greater than $F_{weathering}$ the ocean will lose ALK and DIC in a 2:1 ratio that lowers pH and $\Omega$ and raises $CO_2$, where the $\Omega$ decline shoals the depth of the calcite saturation horizon (CSH). This CSH shoaling increases the area of abyssal seafloor with complete $CaCO_3$ dissolution–a reduction in burial efficiency that works toward restoring the weathering/burial balance (Fig. 9). In the opposite case, $F_{burial}$ is less than $F_{weathering}$, the surplus supply of alkalinity would raise ocean $CO_3^{2-}$, pH and $\Omega$ so as to deepen the CSH to allow for more efficient burial and, eventually, a balanced alkalinity budget. The fact that the lysocline has existed in the deep ocean throughout the Cenozoic (the last 65 million years; e.g., Pälike et al., 2012) and likely since the rise of pelagic calcification in the mid-Mesozoic

(Ridgwell, 2005) suggests that the operation of this negative feedback acts to dynamically stabilize deep ocean $CaCO_3$ saturation by adjusting ocean ALK and DIC in a 2:1 ratio.

This general mechanism of "carbonate compensation" can act in two different ways starting from an initially balanced budget (Sigman et al., 1998): First, if there is an increase in weathering and/or reduction in $CaCO_3$ production, the initial CSH and lysocline will be too shallow to allow for adequate $CaCO_3$ burial to balance the alkalinity budget and so the ocean's alkalinity will increase to establish a new and deeper CSH and lysocline at a overall higher ocean Ω and lower $CO_2$. This dynamic response is referred to as steady state lysocline change that is expected to manifest in a lasting change in $CaCO_3$ preservation on the deep ocean seafloor. Second, if there is a sudden change in deep ocean Ω related to any of the closed-system changes, but not affecting weathering or $CaCO_3$ production, the initial forced change in Ω will change the CSH depth and cause an alkalinity budget imbalance without any change in the eventual steady state lysocline depth. For example, with a forced decrease in deep ocean Ω and burial efficiency by cooling or additional carbon sequestration by the soft-tissue pump, we expect carbonate burial to be transiently suppressed relative to weathering, while the ocean is accumulating alkalinity to raise saturation until the CSH and lysocline reach their old depth and the alkalinity budget is back in balance.

When considering these dynamics in the context of the long term record of Earth's carbon cycle we should therefore expect changes in weathering and $CaCO_3$ production to drive lasting changes in deep ocean $CaCO_3$ saturation and preservation associated with steady state lysocline shifts. In contrast, the timescale of carbonate compensation is sufficiently short (4000–5000 years; Section "$CaCO_3$ compensation") that transient carbonate compensation without steady state lysocline change will be hard to detect based on sediment properties alone, given the relatively slow accumulation rate of deep sea sediments. That is, on timescales >10,000 years we can safely assume that the alkalinity budget of the ocean will be balanced, but the degree of deep ocean $CaCO_3$ saturation required to achieve that balance will change with both $CaCO_3$ production and the weathering flux.

### *Silicate weathering thermostat*

Volcanic outgassing releases $CO_2$ to the atmosphere at a rate that is difficult to measure and likely variable through time for individual volcanic and hydrothermal systems (Aiuppa et al., 2019). And yet, the prevailing view is that the global aggregate volcanic $CO_2$ flux is relatively steady when averaged over thousands of years, with current estimates <0.1 PgC/yr (Burton et al., 2013; Werner et al., 2019; Fischer et al., 2019). While this rate is about 100× slower than anthropogenic $CO_2$ emissions, the ultimate fate of that carbon is similar. Without other reactions the added $CO_2$ will dissolve into the ocean to form bicarbonate and cause ocean acidification that reduces the $CaCO_3$ saturation of seawater (Eq. 46). This is the closed-system response that takes about 1000 years to complete. If the $CO_2$ is allowed to react with and dissolve limestone on land or previously deposited $CaCO_3$ in the ocean, the added carbon will be neutralized to bicarbonate (Eq. 47), with only a minor residual effect of raising $CO_2$ while the ocean accumulates DIC and ALK at double the rate of the volcanic $CO_2$ flux (continuous accumulation, no steady state). Alternatively, if the $CO_2$ is allowed to react with silicate minerals, then the weathering reaction will produce alkalinity without adding any further carbon so that the global carbon budget can be balanced by $CaCO_3$ burial if silicate weathering alkalinity release is double the volcanic $CO_2$ flux (Eq. 48).

$$CO_2 + H_2O \Rightarrow H^+ + HCO_3^- \Leftrightarrow 2H^+ + CO_3^{2-} \tag{46}$$

$$CO_2 + CaCO_3 + H_2O \Rightarrow Ca^{2+} + 2HCO_3^- \Leftrightarrow CaCO_3 + CO_2 \tag{47}$$

$$2CO_2 + CaSiO_3 + H_2O \Rightarrow Ca^{2+} + SiO_2 + 2HCO_3^- \Leftrightarrow CaCO_3 + SiO_2 + CO_2 \tag{48}$$

There are two leading hypotheses why the silicate weathering flux should be able to adjust through time to dynamically match in a 2:1 ratio whatever changes in volcanic $CO_2$ flux might occur due to plate tectonic forcing, and both of these possible negative feedbacks rely on the greenhouse effect of $CO_2$ to drive climate change (bottom of Fig. 9; Walker et al., 1981). If there was a surplus of volcanism over weathering, then that imbalance would tend to gradually raise $CO_2$ as the ocean accumulates $HCO_3^-$ from the imbalance and carbonate compensation, and that $CO_2$ rise would gradually raise surface temperatures so as to speed-up weathering reactions. This first mechanism is mainly applicable in situations where soil pore fluids are far from chemical equilibrium with respect to silicate minerals in the soil but the weathering reaction per unit mineral surface area is rate-limited due to the high activation energy of detaching surface ions from the mineral lattice. Alternatively, $CO_2$-driven warming causes the atmosphere to hold more water vapor, transport more water over land and thereby increase continental runoff. This second mechanism is mainly applicable if the runoff is near chemical equilibrium with silicate minerals so that the overall weathering reaction progress is transport-limited by the slow percolation and subsurface drainage of net precipitation (Fritsch et al., 2011; Guinoiseau et al., 2021) and by the slow denudation of soils to expose fresh silicate minerals (Stallard and Edmond, 1983). In both the rate-limited and transport-limited cases the overall weathering rate can be expected to increase exponentially with temperature, and a given increment of temperature increase requires an exponential increase in $CO_2$, thereby yielding changes in weathering that are proportional to differential $\delta \ln CO_2$ change and the associated radiative forcing (Eq. 49):

$$\frac{\delta F_{SW}}{\delta T}\frac{\delta T}{\delta lnCO_2} = \frac{\delta F_{SW}}{\delta lnCO_2} = k_T \cdot F_{SW} \cdot ESS \cdot 5.35\frac{W}{m^2} = k_{lnCO_2} \tag{49}$$

where $k_T$ is the percent change in silicate weathering per degree of warming, ESS is the Earth System Sensitivity (PALEOSENS, 2012; Wong et al., 2021) of Global Mean Temperature (GMT) to $CO_2$ radiative forcing, 5.35 $W/m^2$ is the $CO_2$ radiative forcing per

$lnCO_2$, and $k_{lnCO2}$ is the percent change in silicate weathering per $lnCO_2$. It is this sensitivity of silicate weathering to climate that acts to reduce the imbalance between volcanic $CO_2$ emissions and silicate weathering according to this theory. For example, if there was some initial imbalance (I) from surplus volcanic $CO_2$ emissions (as in Eq. 50), that imbalance should decline as $lnCO_2$ and silicate weathering increase (Eq. 51):

$$I = 2 \cdot F_{Volc} - F_{SW} \tag{50}$$

$$\delta I = -k_{lnCO_2} \cdot \delta lnCO_2 \tag{51}$$

Further, because the ocean $CaCO_3$ saturation is stabilized by carbonate compensation, there will be minimal change in ocean carbonate ion concentration, such that the change in atmospheric $CO_2$ needs to be supported by a proportional change in seawater bicarbonate concentration (Eq. 52) as forced by the imbalance between volcanism and silicate weathering (Eq. 53):

$$\delta lnCO_2 = 2 \cdot \delta lnHCO_3^- - \delta lnCO_3^{2-} \approx 2 \cdot \delta lnHCO_3^- \tag{52}$$

$$\frac{\delta HCO_3^-}{\delta t} = \frac{2 \cdot F_{Volc} - F_{SW}}{M_{oc}} \Leftrightarrow \frac{\delta lnHCO_3^-}{\delta t} \approx \frac{2 \cdot F_{Volc} - F_{SW}}{DIC \cdot M_{oc}} \tag{53}$$

As such, any initial imbalance ($I_0$) that might exist in the Earth System will exponentially decline over time as temperature, atmospheric $CO_2$ and silicate weathering all adjust to match volcanic $CO_2$ input with silicate weathering. Eq. (54)–(56) represent the timescale over which imbalances are eliminated. That is, for every increment of time ($\delta t$) that some imbalance exists, the imbalance will decline by a set percentage ($\delta I/I$), such that it asymptotes over time toward zero with a characteristic e-folding timescale ($\tau_{SW}$) (Eq. 56):

$$\frac{\delta I}{I_0} = \delta lnI \approx \frac{-2 \cdot k_{lnCO_2}}{DIC \cdot M_{oc}} \cdot \delta t \tag{54}$$

$$I(t) = I_0 \cdot e^{\frac{-t}{\tau_{SW}}} \tag{55}$$

$$\tau_{SW} = \frac{DIC \cdot M_{oc}}{-2 \cdot k_{lnCO_2}} = \frac{DIC \cdot M_{oc}}{-2 \cdot k_T \cdot ESS \cdot 5.35 \frac{W}{m^2} \cdot F_{SW}} \approx 0.5 \text{ to } 1 \text{ million years} \tag{56}$$

The $10^5$–$10^6$ yr timescale of the silicate weathering feedback, as derived above, is notably longer than the residence time of carbon in the surface reservoir, ~150 kyr. The long silicate weathering timescale is reflected in our open system cGENIE simulation (Fig. 8, blue lines), where silicate weathering acts to remove most of the added $CO_2$ and the net dissolved $CaCO_3$ from carbonate compensation by the end of our one million year experiment (i.e., about two e-folding timescales). That is, as the imbalance between volcanic $CO_2$ emissions and silicate weathering is gradually removing the anthropogenic carbon initially released in our experiment, the much faster carbonate compensation feedback is keeping up by burying the equivalent flux of $CaCO_3$. Hence, the silicate weathering experiment, in contrast to either the fixed weathering or closed system experiments, has a total inventory of carbon in the ocean and atmosphere after $10^6$ years that is near to the initial inventory prior to carbon injection. In other words, carbon has not only been redistributed into the oceans but has actually been removed from the surface reservoir (Fig. 4).

There is significant uncertainty in both the Earth System Sensitivity and in the temperature dependence of silicate weathering effective at the global scale, thereby casting significant uncertainty on the silicate weathering timescale, reflected in the large range provided in Eq. 56. Beyond the climatic factors that control weathering rates, geologic changes may also affect the 'weatherability' of the land surface (Kump and Arthur, 1997). Factors including continental area and its distribution, exposure of varying rock types, rates of uplift, and the distribution of soils and vegetation collectively determine weatherability and linearly modify the timescale of the silicate weathering feedback. Processes that also scale with mountain-building and erosion, such as oxidation of rock-bound organic carbon and sulfide minerals, can act as $CO_2$ sources and may also need to be explicitly taken into account (Hilton and Joshua West, 2020). Improved constraints should result from the use of models with spatially explicit representations of both weathering and carbonate burial, but computational expense has limited models to either global-scale or spatial consideration of only limited processes (e.g., carbonate burial but not weathering patterns are spatially resolved in our illustrative cGENIE experiments).

Still, in response to abrupt atmospheric carbon emissions, these uncertainties influence the long tail of atmospheric $CO_2$ and the eventual recovery of ocean carbon content, but not the $10^3$ year equilibration of the ocean and atmosphere, or the $10^4$ year neutralization of the added $CO_2$ by net $CaCO_3$ dissolution. This is apparent in the contrast of the fixed weathering and silicate weathering cGENIE experiments in Fig. 5, where their trajectories of atmospheric $CO_2$ only diverge after about $10^5$ years. Further reduction of uncertainty in the silicate weathering feedback strength (and timescale) requires proxy records that reconstruct past carbon cycle perturbations, described in Section "Climate and the carbon cycle."

### Organic carbon

Steady state in the open system carbon cycle also requires considering the input of carbon to the surface carbon reservoir via weathering of ancient organic matter in rocks (mainly as kerogen, or solvent-insoluble organic matter) and removal via sedimentary burial of organic matter (Chang and Berner, 1999; Hilton and Joshua West, 2020). Indeed, Paleozoic and Proterozoic sedimentary sequences have preserved large quantities of organic carbon that was sourced from photosynthesis hundreds of millions

of years ago (McKirdy and Imbus, 1992; Liu et al., 2017), suggesting that on geologic timescales new burial of organic carbon has exceeded tectonic uplift, erosion and weathering of organic carbon-rich sedimentary sequences, plus the leakage of petroleum and natural gas during thermal maturation of organic carbon-rich source rocks. Continental sedimentary sequences are often associated with accommodation space created in old foreland basin and rift systems. During most of Earth history these settings hosted marine or lacustrine depocenters of organic carbon-rich units (Liu et al., 2017), but since the rise of land plants in the Paleozoic these terrestrial sequences have also locked up an enormous amount of organic carbon in the form of coal. Net burial of organic carbon–new burial minus organic carbon weathering–is a source of oxygen to the surface environment (Eq. 2, left to right) and therefore plays an important part in the regulation of atmospheric $O_2$ levels (Berner, 2006).

Net organic carbon burial removes carbon from the surface environment at a rate of <0.1 Pg C per year (e.g., Blattmann et al., 2019), or about 20% of the rate of volcanic $CO_2$ emissions (Kump, 1999). Similar to carbonate and silicate weathering, the weathering of organic carbon should increase with atmospheric $CO_2$ and global warming, but this yields a positive feedback that would not lead to a new balance. There is significant uncertainty in the rate of organic carbon weathering, though a recent estimate has suggested that $CO_2$ release is similar to rates of $CO_2$ uptake by silicate weathering (Zondervan et al., 2023). New organic carbon burial appears to be persistent through geologic time and more closely tied to tectonics than to climate or atmospheric $CO_2$ levels, arguing against a role for net organic carbon burial in dynamically stabilizing atmospheric $CO_2$ and climate in a negative feedback. Moreover, the continued degradation of organic carbon with depth in the sediments by deep microbial activity complicates constraints on the geologic rate of organic carbon burial, also described by the burial efficiency or fraction of deposited organic carbon that is ultimately buried and preserved (Bradley et al., 2022). Recent estimates of organic carbon burial rates that consider the depth and age of organic C in sediment range from 0.144 to 0.202 PgC per year (Bradley et al., 2022), higher than the <0.1 PgC rate provided above (Blattmann et al., 2019). Given uncertainty in the atmospheric $CO_2$ control over both organic carbon weathering and burial, we suggest that the surface carbon budget imbalance from net organic carbon burial is ultimately resolved by the silicate weathering feedback. As such we can simply expand the silicate weathering imbalance equation (Eq. 50) to also include the imbalance between organic carbon weathering ($F_{OCW}$) and burial ($F_{OCB}$) (Eq. 57):

$$I = 2\cdot(F_{Volc} + F_{OCW} - F_{OCB}) - F_{SW} \tag{57}$$

$$\tau_{carbon} = \frac{C_{oc} + C_{atm} + C_{land}}{F_{volc} + F_{CW} + F_{OCW}} \approx \frac{C_{oc} + C_{atm} + C_{land}}{F_{CB} + F_{OCB}} < \tau_{SW} \tag{58}$$

As a consequence, changes in organic carbon cycling can affect atmospheric $CO_2$ and climate both on short timescales of the closed-system carbon cycle as well as the long timescales of carbonate compensation and silicate weathering. From this perspective net organic carbon burial may be understood as a geologic forcing of the carbon cycle and climate change, rather than being part of the dynamics that restore and stabilize surface conditions. Changes in all organic carbon fluxes are particularly significant in terms of carbon isotope mass balance in the surface carbon cycle because of the strong discrimination against $^{13}C$ relative to $^{12}C$ during photosynthesis, yielding organic carbon that is $^{13}C$ depleted relative the $CO_2$ source (O'Leary, 1993; see Section "Carbon and oxygen isotopes of marine carbonate"). The overall carbon isotopic composition of the combined surface carbon reservoir ($C_{oc}$, $C_{land}$, $C_{atm}$) responds to relative changes in the carbon sources from volcanism and weathering ($F_{volc}$, $F_{CW}$, $F_{OCW}$) and carbon burial sinks ($F_{CB}$, $F_{OCB}$), with a response timescale that is much shorter than the silicate weathering timescale (Eq. 58). Hence, carbon isotopes have proven tremendously useful in studying widely different aspects of organic carbon cycling (Mackensen and Schmield, 2019). For example: carbon isotopes record (a) organic carbon cycling by the ocean's biological pump (Hodell and Venz-Curtis, 2006), (b) abrupt release of ocean and terrestrial organic carbon to the atmosphere (Bauska et al., 2016), (c) abrupt release of geologic carbon to the surface environment (McInerney and Wing, 2011), and (d) the long term relative proportion of net organic carbon burial to volcanic $CO_2$ sources (Kump, 1999).

## Climate and the carbon cycle

### Proxies

A "proxy" is a property that may be measured today (such as the magnesium content of a fossil) that may be used to quantitatively or qualitatively reconstruct a property that can no longer be measured directly (such as the temperature of the Eocene ocean). All observational constraints on the dynamics of the carbon cycle through geologic time come from proxies. The exception is $CO_2$ trapped in ice cores, which is technically not a proxy, but an archive of the ancient atmosphere; such records extend a maximum of 2 million years ago (Yan et al., 2019). Most proxies of the carbon cycle and climate with high temporal and spatial resolution spanning the Cenozoic (the modern geologic Era) are derived from ocean sediments. In contrast to archives on land (including glacier ice, tree rings, cave deposits and ancient soils), the marine sedimentary archive is less impacted by unconformities or sparse coverage, though incompleteness is still a limitation. Marine proxies are also particularly important in that they provide information on the dominant component of Earth's surface carbon reservoir.

Paleoceanographers may draw upon a growing body of techniques to reconstruct past physical, chemical, and biological ocean conditions. These techniques are rooted in mid-20th century innovations in ocean drilling and isotope analysis (Becker et al., 2019) and they continue to evolve today as new analytical capabilities emerge (Shevenell et al., 2020). In Section "Proxies," we give a brief introduction to foundational paleo-proxies (e.g., $\delta^{18}O$, $\delta^{13}C$ of carbonate) and then focus on recent and emerging techniques for

constraining carbon cycling and the carbonate system, which increasingly involve creative combinations of proxies (e.g., Vollmer et al., 2022; Yu et al., 2019). Even as caveats or complications are recognized – for example, possible non-temperature controls on the magnesium-to-calcium ratio (Mg/Ca) of foraminiferal calcite – strategies are available to quantify and/or reduce the uncertainty associated with paleo reconstructions. These include (but are not limited to): (1) replication of reconstructions using independent proxies or species, (2) proxy development efforts that widen the span and/or increase the data density of calibrations, and (3) synthesis of complementary proxies that reconstruct different aspects or properties of the same process (e.g., dissolved $O_2$ and pH are both affected by respiration, but are reconstructed using different paleo proxies).

Earth's carbon cycle and climate system are intimately linked, with stabilizing feedbacks regulating atmospheric $CO_2$, surface ocean pH, global temperature and ice sheet extent or sea-level (e.g., Siegenthaler et al., 2005). The field of paleoceanography and paleoclimatology pursues two goals: to generate knowledge of past changes in both climate and the carbon cycle, and to use this knowledge to develop quantitative understanding of carbon-climate interactions and feedbacks within the Earth System (as described in Section "Carbon fluxes and dynamic balances" and visualized in Fig. 10). Knowledge is generated by development and application of empirical methods to reconstruct specific Earth conditions through geologic time, with two broad sets of parameters needed to track changes in the Earth system. We need reconstructions of physical climate conditions such as temperature, the hydrologic cycle, winds and ocean circulation, and we need reconstructions of changes in the global elemental cycles that sustain biological fertility, affect greenhouse gas concentrations and in turn impact climate. The specific parameters required depend on the questions being posed, and in practice the measurement of multiple proxies may be needed to accurately infer a single parameter. For example, radiocarbon dating of ocean water masses needs to be corrected for the effects of metabolic carbon isotope fractionation, and pH reconstructions need to account for ambient temperature change.

A complete description of all the existing techniques for reconstruction of parameters relevant to Earth's carbon-climate system is beyond the scope of this chapter. Here we provide an overview of just three sets of proxy systems that offer core constraints on climate-carbon cycle coupling of the Earth System: (1) carbon and oxygen isotopes ($\delta^{18}O$, $\delta^{13}C$) of marine carbonate, (2) boron proxies ($\delta^{11}B$, B/Ca) in marine carbonate, and (3) physical or faunal indicators in marine sediments of carbonate dissolution or production (weight % $CaCO_3$, carbonate mass accumulation rate). Other relevant proxy systems that we do not cover include (a) additional proxies for surface ocean and atmospheric $CO_2$, such as soil carbon- or alkenone-based carbon isotope approaches (e.g., Hönisch et al., 2023), (b) approaches to reconstruct open ocean productivity (Horner et al., 2021), (c) direct and indirect proxy systems for ocean nutrient cycling (Ai et al., 2020; Farmer et al., 2021), and (d) indirect measures of ocean oxygenation (e.g., Kast et al., 2019; Lu et al., 2020; Auderset et al., 2022; Hoogakker et al., 2024).

### *Carbon and oxygen isotopes of marine carbonate*

While we have discussed sedimentary carbonates as a major sink for carbon and alkalinity (Section "Land carbon storage"), they also represent a rich geochemical archive of Earth history. The stable isotope composition of carbon and oxygen in carbonates were

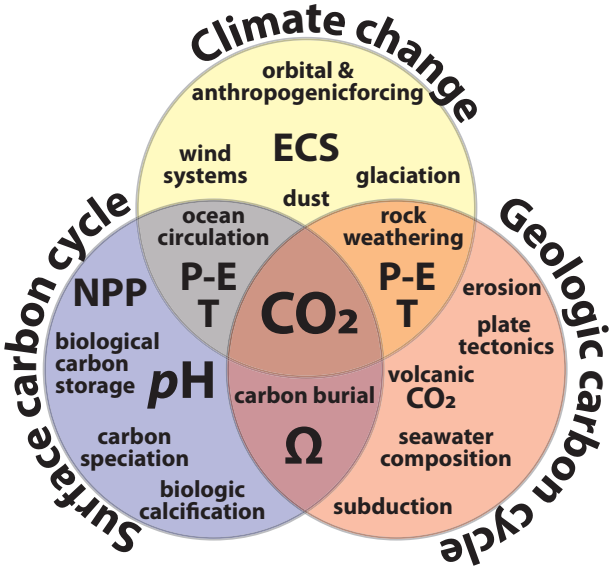


**Fig. 10** Targets for reconstructing Earth System change. If we want to reconstruct the interactions of the climate system with the global carbon cycle, atmospheric $CO_2$ is the central Earth System property we should target. If we want to understand why $CO_2$ has changed in the past we need to reconstruct both the surface carbon cycle (closed system, Section "Closed system exchanges") as well as exchange fluxes between the combined surface carbon stock and geologic carbon stocks (open system; Section "Open system exchanges"). The special complexity of the Earth System is that climate change directly and indirectly affects both open- and closed-system carbon cycling by changing ocean's physical circulation, biological productivity and chemical composition. All of these factors are hence targets for carbon cycle reconstructions. Disentangling how climate shaped atmospheric $CO_2$–and vice versa–provides constraints on the equilibrium climate sensitivity (ECS) to $CO_2$ change and climate-carbon cycle feedbacks applicable to human fossil fuel use.

among the first properties explored by paleoceanographers (e.g., Emiliani, 1955, 1966). Because of the widespread and long-standing access to these techniques and also because of the relatively small amount of sample material needed for analysis, carbon isotope ($\delta^{13}C$) and oxygen isotope ($\delta^{18}O$) records extracted from geologic archives have a greater spatial and temporal coverage than other types of geochemical records. The carbon and oxygen isotopes locked within marine carbonates (and other minerals) are directly linked to Earth's major element cycles and have recorded dramatic changes including the formation of cratons of continental crust since the Archean (Shields and Veizer, 2002; Galili et al., 2019), Proterozoic glaciations ("snowball Earth" episodes; Hoffman et al., 1998), environmental catastrophes and extinctions of the Phanerozoic (Veizer et al., 1999), as well as high resolution records of the climate and carbon cycle across the Cenozoic Era (Zachos et al., 2001; Westerhold et al., 2020), bearing clues to the origin of our present climate system (Langmuir and Broecker, 2012). While neither $\delta^{13}C$ nor $\delta^{18}O$ serve as a standalone proxy for any of the seawater carbonate system properties defined in Section "Carbon cycle models," their widespread availability, their inherent links to carbon, oxygen, and water cycles throughout Earth history, and their demonstrated relationships with carbon species dissolved in seawater make them extremely valuable tools for studying the carbon-climate system through time.

Marine carbonate deposits can form on shallow shelves or in the deep ocean. The ratio of carbonate burial in these two environments may be one of the key geologic controls on ocean pH, carbon and alkalinity inventory, and on atmospheric $CO_2$. It is currently unclear if the primordial ocean weathering alkalinity mass balance was closed through the abiotic precipitation of carbonate mud (Geyman et al., 2022) or authigenic clay minerals (i.e., reverse weathering; Isson and Planavsky, 2018). The evolution of organisms that grow hard parts from $CaCO_3$ (calcifiers) and opal has permanently altered ocean carbon and alkalinity cycling (Grotzinger, 2000), and these organisms' skeletal remains constitute a crucial geologic archive. Marine calcifying organisms arose as part of the Cambrian Explosion, which may have been a response to an unusual combination of extensive continental denudation and a corresponding spike in ocean alkalinity (Peters and Gaines, 2012). During the mid-Mesozoic revolution, the evolution of pelagic calcification by plankton suspended in the surface of the open ocean led to $CaCO_3$ rain to the deep seafloor, giving rise to the feedbacks that stabilize the global carbon cycle described in Section "Carbon fluxes and dynamic balances" (Ridgwell, 2005).

Carbon has two stable isotopes–$^{12}C$ and $^{13}C$–with natural relative abundances of about 98.9% and 1.1%, respectively. Data are typically reported in permille (per-thousand, ‰) as a ratio-of-ratios, where the $^{13}C/^{12}C$ isotope ratio of a sample ($^{13}R_{sample}$) is compared to the isotope ratio of a standard reference material ($^{13}R_{standard}$):

$$\delta^{13}C_{sample} = \left(\frac{^{13}R_{sample}}{^{13}R_{standard}} - 1\right)\cdot 10^3 \tag{59}$$

For example, if $^{13}R_{sample} = 0.01100$ and $^{13}R_{standard} = 0.01125$, then $\delta^{13}C = -22‰$. The aim of using a reference material is to enable quantitative comparisons of isotope ratio measurements made on different mass spectrometers and through time. The convention of formulating the δ-notation in permille units was established for its utility in describing very small differences in isotope ratio. Historically, carbonate samples were referenced to a standard derived from belemnite fossils collected in South Carolina's PeeDee region – PeeDee belemnite (PDB; Craig, 1957). That physical material has long since been consumed by analysis, but researchers still reference modern measured $^{13}R$ to PDB. At a meeting in Vienna in 1987, the zero point of the carbon isotope scale was defined as a virtual material (Vienna PeeDee Belemnite, VPDB), defined by a fixed isotope ratio value assigned to a calcite reference material called NBS19 (Hut, 1987). The VPDB scale was most recently updated in 2020 (Hélie et al., 2021) and efforts to enhance the accuracy, precision, and stability of reference material measurements are ongoing (e.g., Hoffman and Rasmussen, 2022).

The average $\delta^{13}C$ of mantle-derived $CO_2$ (and also the approximate composition of the atmosphere prior to anthropogenic $CO_2$ emissions) is –6‰ (VPDB); the ocean DIC reservoir is approximately 0‰, and organic carbon found in surface sediments and the lithosphere is significantly lower as a result of large kinetic isotope fractionations due to biological activity (≈ –10 to –30‰; Farquhar et al., 1989). In particular, photosynthesis discriminates against the heavy isotope ($^{13}C$), resulting in organic carbon compounds that have a lower $^{13}C/^{12}C$ than their carbon source (this is often referred to as heavy-isotope depletion, or simply isotope depletion; O'Leary, 1993). Within the ocean, variations in $\delta^{13}C$ of DIC ($\delta^{13}C_{DIC}$) are driven, in part, by upper ocean photosynthesis, which raises surface water $\delta^{13}C_{DIC}$ via preferential fixation of low-$\delta^{13}C$ organic carbon that then sinks out of the mixed layer. In the deeper ocean, low-$\delta^{13}C$ particulate organic matter is respired and returned to the DIC pool, which lowers the average $\delta^{13}C_{DIC}$ of the ocean interior. In this way, the biological pump (Section "The ocean's biological pumps") maintains vertical DIC and $\delta^{13}C_{DIC}$ gradients in spite of the large-scale ocean circulation, which works to counteract these gradients by subduction of high-$\delta^{13}C$ surface water and upwelling of low-$\delta^{13}C$ deep water. Air-sea gas exchange also fractionates carbon isotopes of DIC as a function of temperature, decoupling the $\delta^{13}C_{DIC}$ of preformed DIC from nutrients like phosphate, though strong global-scale correlation between $\delta^{13}C_{DIC}$ and phosphate indicate that biological processes exert the dominant control (Mook, 1986; Lynch-Stieglitz et al., 1995; Schmittner et al., 2013; Eide et al., 2017; Vollmer et al., 2022).

Incorporation of carbon into skeletal material may involve diffusion, pumping, and/or seawater vacuolization regulated by the calcifying organism. Potential sources of carbon in biogenic carbonates include dissolved forms such as $HCO_3^-$, $CO_3^{2-}$, and $CO_2$ as well as particulate organic carbon (POC, Section "Ocean carbon") ingested as food. The reservoir of carbon from which all of these are ultimately drawn–ocean DIC–changes in both size and isotopic composition through time. Changes in isotopic composition can occur in response to changes in the fluxes of isotopically distinct reservoirs into and out of the ocean DIC reservoir ($C_{oc}$). This includes both closed-system exchanges (Section "Closed system exchanges"), e.g., expansion/contraction of the isotopically depleted terrestrial biosphere (resulting in enrichment/depletion of global ocean $\delta^{13}C_{DIC}$) as well as open-system exchanges

(Section "Open system exchanges"), e.g., sediment deposition, burial of organic carbon, or volcanic outgassing. Isotopic mass balance dictates that changes in ocean $\delta^{13}C_{DIC}$ are a function of both the isotopic difference between the ocean and the source/sink as well as the magnitude of the flux. The $\delta^{13}C$ difference between planktic foraminifera, which grow in the upper ocean, and benthic foraminifera, which live on or in seafloor sediments, have also been used to assess past changes in the functioning of the biologic pump (Zachos et al., 1989; Ziegler et al., 2013; Greenop et al., 2017). Recent studies on modern samples have confirmed that $\delta^{13}C$ of epifaunal foraminifera is a faithful recorder of contemporaneous bottom-water $\delta^{13}C_{DIC}$ (Mackensen and Schmiedl, 2019); correlation of foraminiferal $\delta^{13}C$ with seawater $CO_3^{2-}$ and pressure merit further investigation (Schmittner et al., 2017).

Oxygen has three stable isotopes–$^{16}O$, $^{17}O$, and $^{18}O$–with natural relative abundances of 99.76%, 0.04%, and 0.20%, respectively. Similar to carbon isotopes, the two most abundant stable isotopes of oxygen are reported in permille (‰) relative to a standard:

$$\delta^{18}O_{sample} = \left(\frac{^{18}R_{sample}}{^{18}R_{standard}} - 1\right)\cdot 10^3 \tag{60}$$

where $^{18}R$ is the ratio of $^{18}O$ over $^{16}O$. Water samples are typically reported relative to a seawater standard: Vienna Standard Mean Ocean Water (V-SMOW), with the physical reference material updated to V-SMOW-2 in 2009 (Gröning et al., 2006). By definition, average seawater is close to 0‰ on the V-SMOW scale. The V-SMOW scale and V-PDB scale are offset from each other by approximately 30‰ (meaning that the same sample would be 0‰ relative to V-SMOW and ~30‰ relative to V-PDB), so when reporting data it is crucial to specify which scale is being referenced (Eqs. (61) and (62), below; Kim et al., 2015).

$$\delta^{18}O_{sample,VSMOW}\,(‰) = 1.03092 \cdot \delta^{18}O_{sample,VPDB} + 30.92 \tag{61}$$

$$\delta^{18}O_{sample,VPDB}\,(‰) = 0.97001 \cdot \delta^{18}O_{sample,VSMOW} - 29.99 \tag{62}$$

Carbonate $\delta^{18}O$ is higher than the water from which it forms because, all else being equal and assuming reversible chemical reactions, heavier isotopes tend to be concentrated into the phase in which they are more strongly bound (equilibrium fractionation) (Bigeleisen, 1965). Within the Earth system, fractionation occurs during gas exchange and phase changes of oxygen-bearing compounds (e.g., $H_2O$, $O_2$, $CaCO_3$, organic matter). Organic matter, marine carbonates, and atmospheric $O_2$ and $CO_2$ are all enriched in $^{18}O$ relative to mean ocean water, while ice locked in the Greenland and Antarctic ice caps are depleted by ~20 to >50‰ (Dansgaard, 1964; Epstein et al., 1977). This occurs as a combined result of preferential evaporation of water containing the lighter isotope ($H_2{}^{16}O$) into air parcels due to its higher vapor pressure (relative to $H_2{}^{18}O$) and also episodic, preferential loss via precipitation of water containing the heavier isotope ($^{18}O$) during atmospheric transport of water vapor to higher and colder latitudes (so-called Rayleigh distillation; Hayes, 2004). As a result, the waxing and waning of global continental ice volume is accompanied by a corresponding enrichment and depletion, respectively, of average ocean $\delta^{18}O$. This is sometimes referred to as the "ice-volume effect."

Oxygen can be incorporated into tests (shells) of foraminifera in different ways, and these processes and associated fractionations are still being investigated. An exhaustive review is beyond the scope of this chapter, but we note a few key observations. First, only about 0.1% of surface oxygen is in the atmosphere ($O_2$) we breathe whereas 99.7% of the oxygen is in the form of water ($H_2O$), with seawater solutes accounting for 0.2% in form of sulfate ($SO_4^{2-}$), and about 0.01% in form of dissolved inorganic carbon (DIC) species. Therefore the $\delta^{18}O$ of water exerts a strong baseline control on the $\delta^{18}O$ of dissolved inorganic carbon species, which are constantly exchanging oxygen with water molecules. Marine carbonate $\delta^{18}O$ is thus expected to be sensitive to changes in seawater $\delta^{18}O$. Second, marine carbonates form with a ~30‰ enrichment of $\delta^{18}O$ relative to seawater, and that fractionation factor is sensitive to the temperature at which inorganic carbonate forms (Urey et al., 1951). Third, isotopic offsets have been observed in the foraminiferal calcite of different species, even when grown under identical conditions, indicating some degree of biological influence or "vital effects" on $\delta^{18}O$ of these biogenic carbonates (e.g., Bemis et al., 1998; Marchitto et al., 2014). Fourth, $\delta^{18}O$ of foraminiferal carbonate has been observed to vary with seawater carbonate chemistry (pH and/or $CO_3^{2-}$), perhaps due to varying relative seawater abundances and/or incorporation of aqueous $HCO_3^-$ and $CO_3^{2-}$ (which are offset in terms of isotopic composition due to differing bond strengths) into growing shells, and/or some form of chemically sensitive biological mediation (e.g., Spero et al., 1997).

Laboratory experiments with inorganically precipitated carbonates have yielded a $\delta^{18}O$ temperature sensitivity of approximately −0.2‰ per °C (McCrea, 1950; O'Neil et al., 1969). Early paleotemperature equations established by Shackleton (1974) are based on inorganic calcite experiments at two temperatures combined with three core-top benthic foraminiferal values (from *Uvigerina*):

$$T = a - b\cdot(\delta_{CaCO_3} - \delta_{Seawater} + c) \tag{63}$$

$$T = a - b\cdot(\delta_{CaCO_3} - \delta_{Seawater} + c) + d\cdot(\delta_{CaCO_3} - \delta_{Seawater} + c)^2 \tag{64}$$

where T is temperature (°C), $\delta_{CaCO3}$ is $\delta^{18}O$ of carbonate (VPDB scale), and $\delta_{Seawater}$ is $\delta^{18}O$ on the VSMOW scale (a, b, c, and d are fitted constants). Calcite (and aragonite) $\delta^{18}O$ depends on both seawater temperature and $\delta^{18}O_{Seawater}$ (Fig. 11). As a result, either temperature or $\delta^{18}O_{Seawater}$ need to be estimated or independently reconstructed to solve for the third variable. Foraminiferal $\delta^{18}O$ during the Cenozoic Era (Section "Reconstructions") is often translated to 'ice-free temperatures' because of the changing contribution of temperature and seawater $\delta^{18}O$ variations to foraminiferal $\delta^{18}O$ following the development of large ice sheets. Ice-free seawater $\delta^{18}O$ estimates for the early Cenozoic are variable, but average around −1‰ on the VSMOW scale (Kennett et al., 1975; Lhomme, 2005; Cramer et al., 2011).

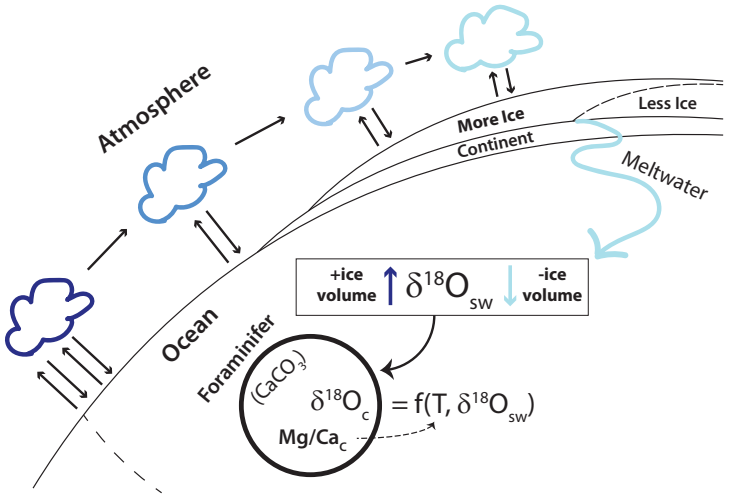


**Fig. 11** Foraminifera oxygen isotope system. The $\delta^{18}O$ of foraminiferal carbonate is primarily a function of two key parameters of the seawater in which it is grown: temperature and $\delta^{18}O_{SW}$. Seawater temperature is a fundamental property of Earth's climate system. Global average seawater $\delta^{18}O$ varies with global continental ice volume, as growth of ice sheets preferentially sequesters the light isotope ($^{16}O$) on land. Locally, seawater $\delta^{18}O$ may be affected by precipitation, evaporation, and water mass mixing.

Early work on the $\delta^{18}O$ of foraminifera has been built upon by many laboratory and field studies, resulting in new equations that are better constrained and have lower uncertainties (e.g., Marchitto et al., 2014) than those from earlier studies. Considering the mixed nature of the 1974 calibration dataset and the availability of more robust equations, continued use of these early calibrations is not recommended. Compilations of the most recent equations and even online tools for $\delta^{18}O$-temperature conversions are available (e.g., Gaskell and Hull, 2023). Another notable advance is the development of "clumped isotope" thermometry, which utilizes the temperature-dependence of bonding between rarer, heavier isotopes in ancient carbonates (e.g., $^{13}C$, $^{18}O$) to reconstruct paleo growth temperatures (Eiler, 2007). Though analytically challenging, this approach has the distinct advantage of being able to estimate temperature without independent knowledge of $\delta^{18}O_{Seawater}$.

### Boron-based proxies of seawater chemistry

Boron (B) is relatively rare in the cosmos, yet it is highly enriched in Earth's crust due to the element's affinity for fluids and aqueous melts (Grew, 2017). Processes that formed Earth's crust also enriched it in B, depleting the residual mantle. Today B continues to cycle among the major reservoirs of crust, mantle, and ocean (Fig. 12). The ocean's boron content has likely varied during Earth history primarily in response to changes in global river runoff and hydrothermal processes, perhaps ranging from 4 to almost 5 ppm (ppm) seawater concentration during the Cenozoic (Lemarchand et al., 2000, 2002). When dissolved in seawater, B is present in two major species: borate ($B(OH)_4^-$) and boric acid ($B(OH)_3$), which are governed by an acid-base equilibrium (Eq. 65, and also discussed in Section "Carbon cycle models"):

$$B(OH)_3 + H_2O \leftrightarrow B(OH)_4^- + H^+ \tag{65}$$

The relative abundances of these B species may be related by a dissociation constant (also called a stability or equilibrium constant), defined as:

$$K_B^* = H^+ \cdot \frac{B(OH)_4^-}{B(OH)_3} \tag{66}$$

The balance point, or stoichiometric dissociation constant, between the abundance of borate and boric acid, represented by $K_B^*$, depends on temperature, salinity, and pressure. As described in Section "Carbon cycle models," borate functions as part of the ocean's alkalinity–the pool of chemical species that will readily buffer addition of an acid, stabilizing solution pH. The parallel behavior of dissolved inorganic carbon species creates a strong link between dissolved C and B speciation in the ocean (Fig. 13). This pH-sensitive speciation, combined with the existence of a strong, constant B isotopic fractionation between $B(OH)_4^-$ and $B(OH)_3$, forms the theoretical foundation of B-based paleo proxies for reconstructing seawater carbonate chemistry.

Boron has two stable isotopes, $^{11}B$ and $^{10}B$, with natural abundances of 80.1% and 19.9%, respectively. The boron isotopic composition of materials is typically expressed in permille notation relative to National Bureau of Standards material 951 (Catanzaro et al., 1970):

$$\delta^{11}B_{sample} = \left(\frac{^{11}R_{sample}}{^{11}R_{NBS951}} - 1\right) \cdot 10^3 \tag{67}$$

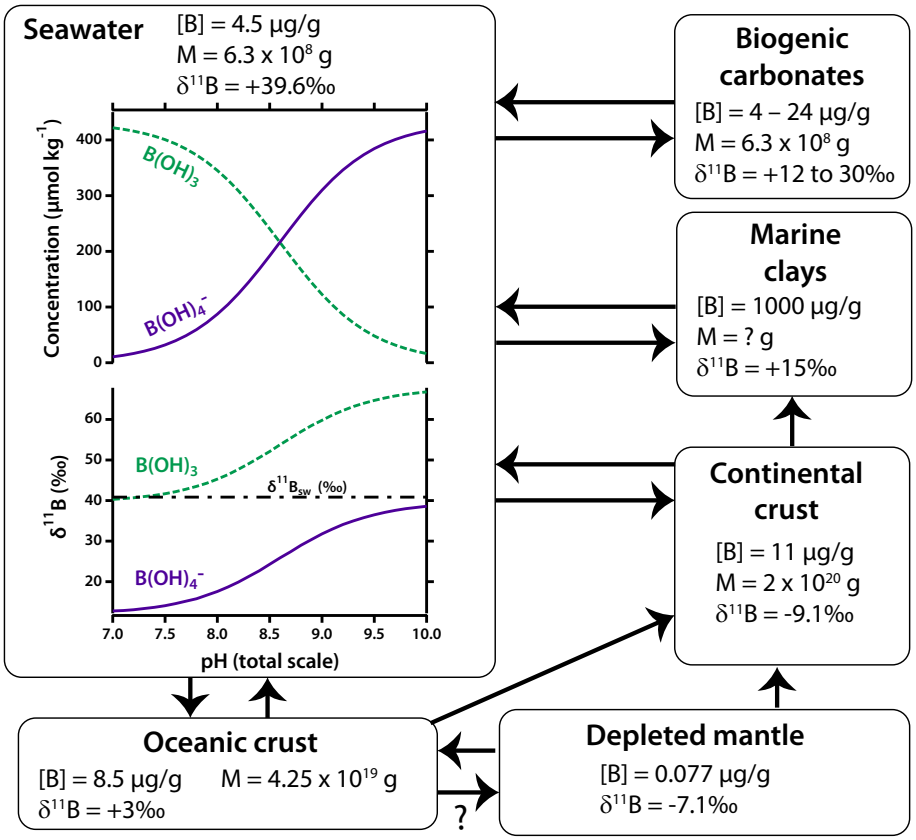


**Fig. 12** Foraminifera boron isotope system. Simplified boron cycle including the size (M) in grams and isotopic composition of reservoirs most relevant to boron paleoproxies. Boron concentrations ([B]) and isotope compositions in permille (‰) relative to NBS951 are from Grew (2017), Palmer (2017), Foster et al. (2010), and Hönisch et al. (2019). Boric acid ($B(OH)_3$) and borate ($B(OH)_4^-$) curves are estimates calculated using CO2SYS (Sharp et al., 2020) assuming $[B]_{sw}$ from Lee et al. (2010), $\alpha_B = 27.2‰$ (Klochko et al., 2006), $\delta^{11}B_{sw} = 39.61‰$ (Foster et al., 2010), 25 °C, salinity of 35, and surface pressure, corresponding to $pK_B$ value of 8.59.

where $^{11}R$ is the ratio of $^{11}B$ to $^{10}B$. Today the mean boron isotopic composition of seawater ($\delta^{11}B_{SW}$) is $39.61 \pm 0.04‰$ (Foster et al., 2010). Estimates for the residence time of B in the global ocean are on the order of $10^7$ years, supported by existing constraints on B fluxes and reservoirs and also by modern observations of global ocean isotopic homogeneity (Berner and Berner, 1996; Foster et al., 2010; Lemarchand et al., 2000, 2002). The mean ocean isotopic composition has varied in the past along with seawater B concentration in response to variable B fluxes among reservoirs (Lemarchand et al., 2000, 2002; Simon et al., 2006; Fig. 12).

Coordination of the boric acid molecule is trigonal-planar, while the borate molecule is tetrahedral. The resulting difference in vibrational frequencies in B-bonding environments of these two chemical species results in a constant isotopic fractionation between boric acid and borate in seawater (Klochko et al., 2006; Nir et al., 2015). This offset ($\varepsilon_B$), locked in at a constant value by the stable coordination of each B species, is illustrated in Fig. 12. Even as the relative abundances of boric acid and borate vary alongside pH, temperature, and seawater major ion composition (Hain et al., 2015), their isotopic offset and their summed isotopic composition remain constant (Nir et al., 2015). Eq. (68) provides an approximation for this isotope mass balance:

$$\delta^{11}B_{SW} \cdot B_{SW} = \delta^{11}B_{B(OH)_3} \cdot B(OH)_3 + \delta^{11}B_{B(OH)_4^-} \cdot B(OH)_4^- \tag{68}$$

This approximation is very useful, but it may result in small offsets from the full isotope ratio mass balance equation in Eq. (69), which can be solved when more accurate estimates are needed (Rae, 2018):

$$\frac{^{11}R_{SW} \cdot \left(B(OH)_4^- + B(OH)_3\right)}{^{11}R_{SW} + 1} = \frac{^{11}R_{B(OH)_4^-} \cdot \alpha_B \cdot B(OH)_3}{^{11}R_{B(OH)_4^-} \cdot \alpha_B + 1} + \frac{^{11}R_{B(OH)_4^-} \cdot \alpha_B \cdot B(OH)_4^-}{^{11}R_{B(OH)_4^-} + 1} \tag{69}$$

Collectively, these properties of boron–the element's ocean residence time, chemical speciation, and isotopic fractionation in seawater, as well as its pH-sensitive behavior alongside carbon – all can play a role in its function as a paleo proxy for different aspects of the carbonate system.

To reliably record the pH-dependent balance between the two dissolved B species in seawater (boric acid and borate) carbonates either need to incorporate a *single* B species, a *constant* mixture of the two, or a *predictable* mixture of the two. Initial hypotheses regarding B incorporation into carbonates suggested that the charged borate ion (as opposed to the uncharged boric acid molecule) would be more likely to be attracted to the charged mineral surface and ultimately be incorporated into the calcite and/or aragonite

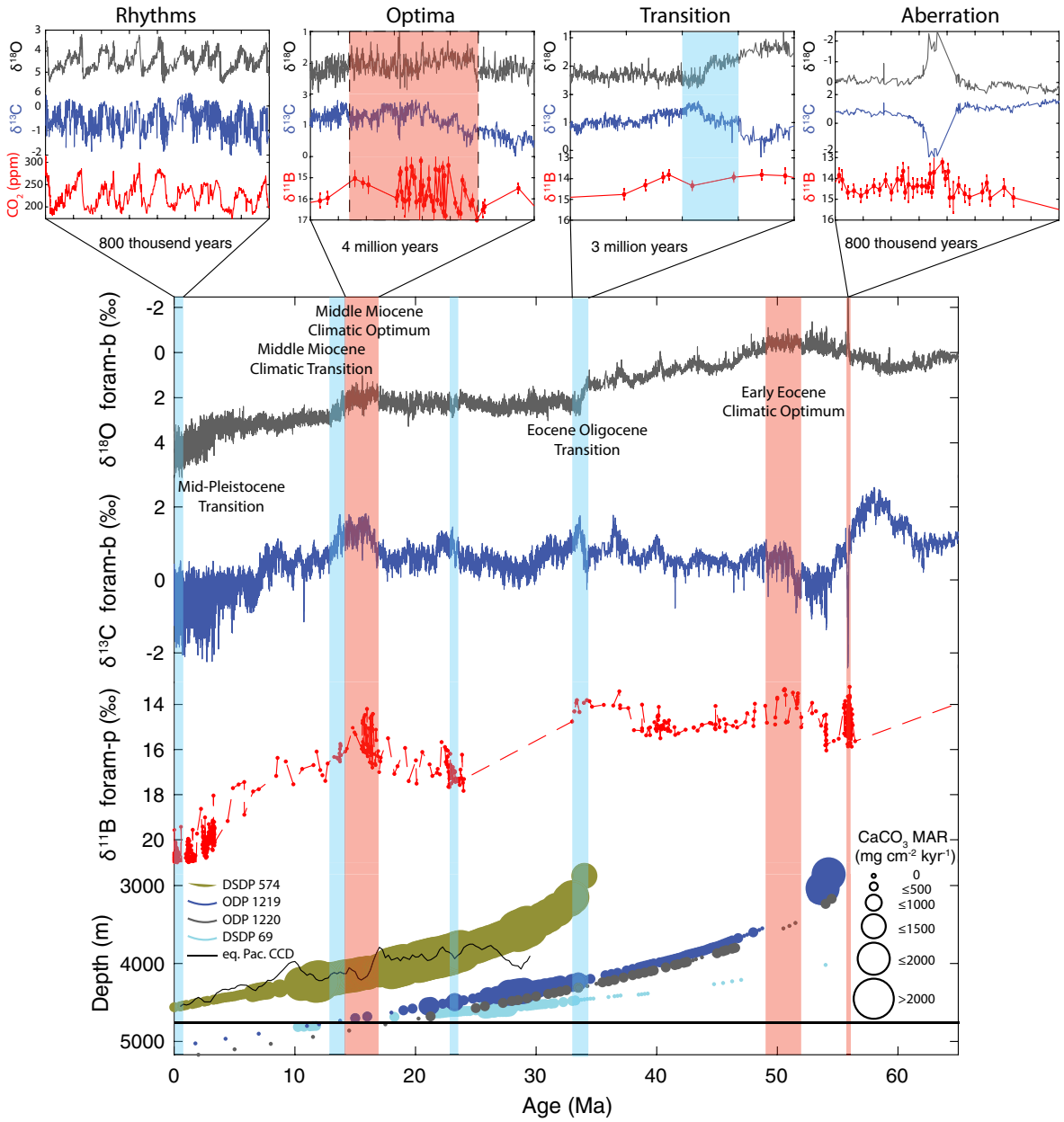


**Fig. 13** Cenozoic proxy records of the carbon cycle and climate. Compiled proxy records of the climate and carbon cycle for the Cenozoic Era, indicating reconstructions on different timescales as described in Section "Reconstructions." In the main figure (top to bottom), benthic foraminiferal oxygen stable isotope ($\delta^{18}O$, gray) and carbon stable isotope ($\delta^{13}C$, blue) records from the Cenozoic Global Reference benthic foraminifer carbon and oxygen Isotope Dataset (CENOGRID) (Westerhold et al., 2020), planktic foraminiferal boron stable isotope ($\delta^{11}B$, red) (Rae et al., 2021), and equatorial Pacific carbonate accumulation (Pälike et al., 2012 and CCD reconstruction (Campbell et al., 2018)) plotted as a function of past water depth. At the top of the figure, zoom-ins indicate the following: (1) 'rhythms' zooms in on the past 0.8 Myr and includes $\delta^{18}O$, gray, and $\delta^{13}C$, blue from CENOGRID, along with the ice core $CO_2$ record, red (Bereiter et al., 2015); (2) 'optima' zooms in on the Mid-Miocene Climate Optimum (MMCO) defined as ~14.7 to 17 Ma (Holbourn et al., 2015) and includes $\delta^{18}O$, gray, and $\delta^{13}C$, blue from CENOGRID, and $\delta^{11}B$, red (Rae et al., 2021); (3) 'transition' zooms in on the Eocene Oligocene Transition from 33.5 to 34 Ma and includes $\delta^{18}O$, gray, and $\delta^{13}C$, blue from CENOGRID, and $\delta^{11}B$, red (Rae et al., 2021); (4) 'aberrations' zooms in on the Paleocene-Eocene Thermal Maximum and includes $\delta^{18}O$, gray, and $\delta^{13}C$, blue from CENOGRID, and $\delta^{11}B$, red, from ODP Site 401 (Gutjahr et al., 2017).

lattice (e.g., Hemming and Hanson, 1992). Early inorganic precipitation experiments yielded evidence to support this idea (e.g., Sanyal et al., 2000), and recent work still largely supports sole or dominant incorporation of borate into aragonite, resulting in $\delta^{11}B$ and boron-to-calcium ratios (B/Ca) that broadly increase with solution pH. However, recent work has suggested that incorporation of B, especially into calcite, could involve a mixture of boric acid and borate and/or involve detectable kinetic fractionation (Uchikawa et al., 2015). Therefore while the current body of research on B in synthetic carbonates broadly supports the theoretical basis for B-based proxies for the carbonate system, with both B/Ca and $\delta^{11}B$ of precipitated $CaCO_3$ reliably increasing with seawater

pH, several questions remain and merit further investigation. In particular, deeper understanding of potential roles of solution temperature, different incorporation mechanisms, kinetic effects, and major-ion solution composition on B incorporation into carbonates could all enhance our ability to apply and interpret these proxy records (Henehan et al., 2022; also reviews by Hönisch et al., 2019 and Branson, 2018).

In recent decades, culture experiments and field studies have revealed the following regarding B in biogenic carbonates: (1) species offsets exist in terms of both $\delta^{11}B$ and B/Ca of specimens grown under identical conditions, indicating some level of biological control on B incorporation (e.g., Allen et al., 2012; Hönisch et al., 2021), (2) although $\delta^{11}B$ of biogenic carbonates reliably increases with seawater pH, the absolute value of carbonates can be variably or constantly offset from theoretical predictions for solution borate, indicating some incorporation of boric acid and/or operation of a fractionating process, (3) post-depositional modification of original bulk shell or skeletal composition could in some cases affect B proxies (cf. Edgar et al., 2015), and steps should be taken to minimize this possibility, including selection of large and/or consistent shell sizes (for applications involving foraminifera) and verification of reconstructions with independent proxy evidence (Hönisch et al., 2019; Rae, 2018). The theoretical framework for B incorporation into carbonate minerals outlined in the section above predicts that B/Ca and $\delta^{11}B$ of marine carbonates should behave in a similar manner, responding in parallel to changes in the concentration of borate in seawater. B/Ca observations deviate somewhat from theoretical predictions, with *benthic* foraminiferal B/Ca covarying strongly with bottom-water $\Delta CO_3^{2-}$ (Yu and Elderfield, 2007; Rae et al., 2011; Brown et al., 2011), *planktic* foraminiferal B/Ca appearing to respond to seawater borate-to-bicarbonate ion ratio or other, closely related parameters (Allen et al., 2011; Henehan et al., 2015), and unexplained offsets persisting among species.

Collectively, these observations and outstanding questions mean that both B/Ca and $\delta^{11}B$ are currently empirical proxies, as are virtually all other geochemical reconstruction techniques in our paleoceanographic toolbox. However, the broad consistency of observations with theoretical predictions is, in many cases, significant and encouraging, forming a reasonable framework that will continue to be investigated. In addition, recent interlaboratory studies determined that although isotopic offsets exist among techniques and laboratories that analyze $\delta^{11}B$, those offsets are quantifiable, consistent, and may be accounted for in order to produce comparable results within the international research community (Foster et al., 2013). Overall, boron-based proxies represent powerful tools with which the past ocean's carbon speciation and cycling may be investigated. Primary targets for future development should include the points listed above as well as establishment of robust constraints on mean-ocean total boron concentration and $\delta^{11}B$ through time. The latter is particularly important since it is required for the conversion of $\delta^{11}B$-borate estimates (reconstructed from marine carbonates) into seawater pH via Eq. (70):

$$pH = pK_B^* - log\left(-\frac{\delta^{11}B_{SW} - \delta^{11}B_{B(OH)_4^-}}{\delta^{11}B_{sw} - \alpha_B \cdot \delta^{11}B_{B(OH)_4^-} - \varepsilon_B}\right) \tag{70}$$

### Sedimentation constraints on the C cycle

Extant seafloor sediment deposits date as far back as ~180 million years, however, the mean age of ocean crust is only ~64 million years (Müller et al., 2008; Seton et al., 2020). The burial of carbonate and organic carbon in these preserved sediment sequences represents the removal of carbon from the surface reservoir ($C_{oc}$, $C_{land}$, $C_{atm}$), where only the preservation of carbonates is related to seawater acid/base chemistry and atmospheric $CO_2$ (Sections "Carbon cycle models" and "$CaCO_3$ compensation"). These relationships are illustrated in the contrast of our "fixed weathering" and "silicate weathering" cGENIE experiments in Fig. 5. In response to injection of atmospheric $CO_2$, the ocean saturation state ($\Omega$) decreases, and so does the amount of carbonate preserved on the seafloor. However, the reduction in sedimentary carbonate content delivers alkalinity to the oceans that enables the further reduction of atmospheric $CO_2$ beyond the closed system redistribution. The power of reconstructing sedimentary carbonate content is thus two-fold: it provides constraint not only on the overall mass balance of the surface carbon reservoir but it further constrains the distribution of carbon between the ocean and atmosphere. In a specific example, the prolonged reduction in deep sea $CaCO_3$ burial during the Paleocene-Eocene Thermal Maximum global warming event has been used as a constraint on the mass of carbon injected into the surface carbon cycle d (Panchuk et al., 2008; Zeebe et al., 2009; see Section "Reconstructions").

Constraints on carbonate preservation have historically taken the form of reconstructions of the regional/global lysocline and/or carbonate compensation depth (CCD). While the lysocline (Section "$CaCO_3$ compensation") is identified through evidence of dissolution in carbonate sediments, the CCD is the depth where sediments are practically devoid of carbonate (though in practice often identified where the weight percentage of $CaCO_3$ in the sediment is $<20$ wt%). Andel and Tjeerd (1975) provided the first reconstruction of the Cenozoic CCD based on the distribution through time of carbonate sediments with known age and depth of the underlying basement. The Van Andel CCD curves, along with some regional updates (e.g. Pälike et al., 2012) have been used to constrain the evolution of the carbonate system and $CO_2$ through time, even though these require the questionable assumption that the CCD faithfully records changes in the depth of the CSH (i.e., Tyrrell and Zeebe, 2004; Caves et al., 2016). At the same time, the depth between the lysocline and the CCD varies both within the present ocean (Broecker and Takahashi, 1977) and during past glacial to interglacial transitions (Farrell and Prell, 1989; Section "Reconstructions").

Another way to identify the CCD (aside from an approximate wt% $CaCO_3$ in sediments) is to calculate the depth at which the mass accumulation rate of carbonate approaches zero (Lyle, 2003). The advantage of accumulation rate constraints on the CCD beyond measurements of wt% $CaCO_3$ arises because there is a highly nonlinear relationship between wt% $CaCO_3$ and carbonate dissolution in sediments (Broecker and Peng, 1982) and because dilution by non-carbonate sediments also impacts wt%

$CaCO_3$ (Lyle, 2003). Sediment mass accumulation rates (or "bulk" MAR, g/kyr/cm$^2$) are the product of linear sedimentation rate (cm/kyr) and dry bulk density (g/cm$^3$). Accumulation of any particular sedimentary component (e.g., carbonate) can be obtained by multiplying bulk MAR by composition (wt%) measurements. Data of either wt% $CaCO_3$ or carbonate MAR are only effective at constraining the CCD when data from multiple sites at multiple depth intervals are combined. (A single site with $CaCO_3 < 20$ wt% or carbonate MAR = 0 can only provide a maximum depth of the CCD). Moreover, variability in the distribution of modern carbonate sediments (Archer, 1996a,b) indicates the importance of adequate spatial coverage to constrain the CCD equivalently in the past.

Finally, additional proxies may constrain the lysocline. These typically include aspects of the foraminifera found in deep-sea sediments. For example, the ratio of benthic to planktic foraminifera shells increases positively with dissolution (Berger, 1970) as does the ratio of shell fragments to whole intact shells (Le and Shackleton, 1992). Fragmentation index, in particular, can be difficult to assess; recent research has suggested the use of image analysis to determine fragmentation intensity, a metric that includes both the number and size of shell fragments (Suárez-Ibarra et al., 2021).

Burial of sedimentary $C_{org}$ is also an essential part of C cycling, but significant sedimentary $C_{org}$ burial occurs in much more restricted regions in comparison to carbonate, and $C_{org}$ burial rates in the deep sea (>1000 m) are an order of magnitude lower than for $CaCO_3$ (Hedges and Keil, 1995). In fact, shelves (<50 m) alone account for nearly half of all organic carbon burial (Dunne et al., 2007). The relative fraction of carbon buried as carbonate and organic carbon has very likely changed through geologic time (Kump, 1999); these variations can account for changes in the carbon isotope records of marine carbonates (Section "Reconstructions"). Reconstruction of $C_{org}$ burial is conceptually similar to carbonate MAR: multiplying wt% total organic carbon (TOC) by bulk MAR; however, calculating this value from the deep-sea sediment cores used in CCD reconstruction would represent only a tiny fraction of global organic carbon burial. Organic carbon burial during the Cenozoic could provide useful constraints for Earth System Models; at present, very few include a sophisticated representation of organic carbon preservation (Hülse et al., 2017), a fact hampered by the lack of quantitative past (or even present) reconstruction of organic carbon burial rates. Even in the modern ocean, the burial efficiency, or the proportion of organic carbon reaching the seafloor that is buried, is poorly defined, particularly because organic carbon continues to degrade in very deep and ancient sediment (Bradley et al., 2022).

## Reconstructions

Geologists have attempted to constrain carbon cycle and climate fluctuations across a vast sweep of Earth history (e.g. Mills et al., 2019). Reconstructions of climate and carbon cycle variations across the Cenozoic Era have dramatically better resolution in comparison to earlier Eras via the marine proxy systems. Increasingly, efforts at past reconstruction merge information from proxies (Section "Proxies") with numerical modeling techniques (Section "Carbon chemistry") in order to constrain not only past climate states but the distribution of carbon within the climate system controlled by carbon cycle dynamics (Section "Carbon fluxes and dynamic balances"). However, fundamental questions remain in reconstructing dynamics at multiple temporal scales across the Cenozoic; including (1) the first order Cenozoic-long decline in temperature and atmospheric $CO_2$, (2) the source and fate of carbon across distinct climatic transitions or aberrations, and (3) the redistribution of carbon between surface carbon reservoirs during the Quaternary glacial cycles. Understanding all of these dynamics is important for projecting the carbon cycle response to anthropogenic carbon input. The rapid timescale of modern carbon addition leads to disequilibrium in the partitioning of carbon within the surface carbon reservoir, but open system processes are crucial for the eventual recovery of the carbon cycle and climate because the source of carbon (primarily fossil fuels) is external to the r surface carbon system.

### *Cenozoic trends and rhythms*

The Cenozoic-long trends in the climate and carbon cycle are cooling and declining atmospheric $CO_2$, but these trends were not monotonic (Hönisch et al., 2023). Explicitly, we consider trends as a secular drift in open system steady state on a timescale greater than the silicate weathering feedback (Eq. 56). At steady state, carbon input and removal fluxes to/from the surface carbon reservoir ($C_{oc}$, $C_{land}$, $C_{atm}$) are balanced (see Section "Open system exchanges"). Trends in deep ocean temperature and global ice volume are reconstructed by benthic foraminiferal oxygen stable isotope records ($\delta^{18}O$, see Section "Boron-based proxies of seawater chemistry"); most recently the CENOGRID megasplice of records from deep sea sites has provided an astronomically dated 66 million year record of Earth's climate (Fig. 13, gray lines) (Westerhold et al., 2020). Peak deep ocean temperature in excess of 10 °C occurred in the Hothouse climate of the Early Eocene Climate Optimum (EECO, ~52 to 50 Ma) while the emergence of a Coolhouse climate characterized by near-freezing deep ocean temperatures and ice on Antarctica occurred across the Eocene Oligocene Transition (EOT, ~34 Ma) with Antarctic ice sheet retrenchment during cooling across the middle Miocene Climate Transition (~14–13 Ma). A full icehouse climate, with significant bipolar glaciation, arose across the Pliocene-Pleistocene Transition (~2.6 Ma; Zachos et al., 2001; Westerhold et al., 2020). Conversely, significant warming trends also occurred during the Cenozoic, particularly from late Paleocene to the Early Eocene Climate Optimum (~58–52 Ma) and into the Middle Miocene Climate Optimum (MMCO, ~17 to 14.7 Ma; Holbourn et al., 2015; Westerhold et al., 2020). Prior to the development of significant land-based ice across the EOT, the benthic $\delta^{18}O$ record is a more straightforward indicator of changes in deep ocean temperature. Following the EOT, an independent constraint on temperature or the $\delta^{18}O$ of seawater is needed to convert variations in $\delta^{18}O$ to temperature.

Alongside long Cenozoic cooling, proxy-$CO_2$ records consistently indicate a decline in atmospheric $CO_2$, from a peak of ~1600 ppm during the Early Eocene to the Quaternary Icehouse minimum of ~180 ppm (Hönisch et al., 2023). Fig. 13 includes

a compilation of boron isotope data ($\delta^{11}B$, red lines, see Section "Boron-based proxies of seawater chemistry") from subtropical planktic foraminifera (Rae et al., 2021); the long-term Cenozoic increase in $\delta^{11}B$ is consistent with increasing surface ocean pH and declining atmospheric $CO_2$. The clear coupling of $CO_2$ and climate trends across the Cenozoic implicates $CO_2$ as the primary (though not sole) driver of Cenozoic climate change. However carbon cycle reconstructions are insufficient to constrain the cause of this long-term Cenozoic $CO_2$ trend, which has been explained variously by enhanced weathering fluxes (Raymo, 1991), enhanced weathering feedback strength (Kump and Arthur, 1997; Caves et al., 2016), decreased volcanic outgassing flux (Der Meer et al., 2014), or combinations of these processes (Berner, 1990). Cenozoic evolution of the carbon cycle would also have been influenced by any changes in organic carbon weathering and burial (Li and Elderfield, 2013). Reconstruction of the CCD is often used as an additional constraint on Cenozoic trends in atmospheric $CO_2$; for instance, as a second constraint on the seawater carbonate system in order to use the $\delta^{11}B$-pH proxy to calculate $CO_2$ (Raymo et al., 1988; Kashiwagi et al., 2008; Caves et al., 2016; Der Ploeg et al., 2019; Komar and Zeebe, 2021; Rae et al., 2021; Derry, 2022). Given the requirement that carbonate burial balances the weathering input of alkalinity, movements of the CCD are presumed to reflect this balance. This interpretation is complicated by changes in the relative shallow-to-deep distribution of carbonate burial as a function of changing seawater chemistry and ocean hypsometry, which decouples CCD changes from global carbonate burial (Opdyke and Wilkinson, 1988; Greene et al., 2019; Komar and Zeebe, 2021; Paytan et al., 2021). Overall, the Cenozoic-long trend of CCD deepening determined by Andel and Tjeerd (1975) has been reproduced by subsequent studies (summarized in Komar and Zeebe, 2021).

In contrast to the clear Cenozoic trends in benthic foraminiferal oxygen isotopes (temperature and ice volume), proxy-$CO_2$, and the CCD, benthic carbon isotopes ($\delta^{13}C$, see Section "Carbon and oxygen isotopes of marine carbonate") show large variations but no obvious Cenozoic-long trend parallel to either temperature or $CO_2$ (Fig. 13, blue lines). Prominent multi-million year shifts in benthic $\delta^{13}C$ occurred around the Late Paleocene Carbon Isotope Maximum (~59–57 Ma), the mid-Miocene ('Monterey Event', ~16–14 Ma), and the late Miocene carbon isotope shift (~8–7 Ma) (Westerhold et al., 2020). These shifts have most commonly been interpreted as evidence for intervals of elevated organic carbon burial as a fraction of total carbon burial, leading to prominent carbon isotope maxima because of the large isotopic difference between $CO_2$, DIC and organic matter due to photosynthetic fractionation, though such changes could equivalently indicate reduction in organic carbon weathering (e.g. Kump, 1999). Importantly, the organic carbon fraction of the total carbon burial rate most directly impacts surface ocean $\delta^{13}C$, whereas deep ocean $\delta^{13}C$ is offset by the biological pump (Kump, 1991) (Section "The ocean's biological pumps"). Ideally, variations in the fraction of organic carbon burial would be constrained by estimating mean surface ocean $\delta^{13}C$ from planktic foraminiferal records, though planktic foraminifera are typically less well preserved in comparison to more robust benthic foraminifera. Changes in the rates of volcanism or weathering of carbonates and silicates should result in comparatively less change in benthic foraminiferal $\delta^{13}C$ given the much more similar isotopic composition between mantle carbon, carbonate, and ocean DIC.

Climate change across the Cenozoic is also subject to the influence of persistent rhythms due to quasi-cyclic variations in Earth's orbital geometry (e.g. Zachos et al., 2001; Westerhold et al., 2020). The timescale of these rhythms ranges from the $10^4$ yr period of Earth's combined precession cycles and obliquity cycle to the $10^5$ yr period of cycles in eccentricity. Amplitude modulation of these cycles ranges from $10^5$ to $10^6$ yr periods, such that these climatic rhythms inherently interact with the silicate weathering timescale (Pälike et al., 2006; Russon et al., 2010; Zeebe et al., 2017; Vervoort et al., 2021). Over the $10^4$ year timescale, orbital variations interact with carbonate compensation and ocean-atmosphere carbon exchange. The ice age cycles of the Plio-Pleistocene are the most well-known example of feedbacks between cyclic changes in Earth's orbit and carbon cycle dynamics (see Fig. 13, 'Rhythms'), but similar interactions existed throughout the Cenozoic, albeit with varying results in terms of the feedback mechanisms and amplitude of climatic change (Westerhold et al., 2020).

### *Climate optima*

The term climate optima refers to steady state intervals of high $CO_2$ maintained by elevated rates of carbon input to the surface reservoir relative to removal; in other words, they require changes in open system fluxes. However, there is no clear criteria for what climatic conditions should constitute an 'optimum.' Westerhold et al., 2020, instead suggested the categories Hothouse, Warmhouse, Coolhouse, and Icehouse to identify distinctive climate states across the Cenozoic. The two most prominent Cenozoic intervals labeled as optima based on benthic foraminiferal $\delta^{18}O$ records, corroborated by additional paleotemperature proxies (Meckler et al., 2022) and consistent with reconstructions of atmospheric $CO_2$, are the Early Eocene climatic Optimum (EECO) and the Mid Miocene Climate Optimum (MMCO) (Fig. 13, 'Optima'). These two intervals are local maxima on timescales of $10^6$–$10^7$ years; in other words, they persist on timescales longer than the silicate weathering feedback. The Middle Eocene Climatic Optimum (MECO, ~40 Ma) has also been labeled as an optimum, though it is a shorter lived event of ~400 kyr and hence did not persist for longer than the silicate weathering timescale (Bijl et al., 2010). A Pliocene Climate Optimum has also been described as the warmest interval of the early Pliocene (4.4 to 4 Ma) (Fedorov et al., 2013), though once again, this interval did not persist for a timescale longer than the silicate weathering feedback and does not stand out as a local maxima in temperature or $CO_2$. The EECO was the warmest interval of the entire Cenozoic, identified as a Hothouse climate (Westerhold et al., 2020). Maximum deep ocean temperatures above 10 °C corresponded to atmospheric $CO_2$ of ~1600 ppm based on lower resolution boron isotope reconstructions (Westerhold et al., 2020; Rae et al., 2021; Hönisch et al., 2023). The rise in temperature lagged a trend of declining $\delta^{13}C$ following the Paleocene Carbon Isotope Maximum. Consequently both enhanced volcanism from the North Atlantic Igneous Province as well as reduced organic carbon burial or exhumation and weathering of previously buried organic matter have been proposed as potential sources of elevated $CO_2$ (Komar et al., 2013; Greene et al., 2019). There is some evidence for a relative

deepening of the CCD associated with the warming trend from the Late Paleocene to Early Eocene (Komar et al., 2013; Slotnick et al., 2015), though this has been disputed (Greene et al., 2019). However, understanding of the silicate weathering feedback (Section "Silicate weathering thermostat") suggests that global warming should have resulted in enhanced weathering supply of alkalinity, which must have been compensated by additional carbonate burial somewhere.

Compared to the EECO, the rise in temperature into the mid-Miocene Climate Optimum (~17 to 14.7 Ma) was more abrupt, occurring over $<10^6$ years (Holbourn et al., 2015; Kochhann et al., 2016), though the duration of the climatic optimum was similar (~2 Myr). Comparable to EECO, the MMCO has also been linked to volcanism, in the latter case via eruption of the Columbia River flood basalt group in the Pacific northwest United States (Kasbohm and Schoene, 2018). Proxy records suggest mean atmospheric $CO_2$ during the MMCO of ~500 ppm (Hönisch et al., 2023). There is association between the MMCO and another $\delta^{13}C$ maximum; however, while the Paleocene Carbon Isotope Maximum led the EECO, the Monterey Excursion slightly lagged peak temperature across the mid-Miocene (Westerhold et al., 2020). Reconstructions of the Mid-Miocene CCD indicate an overall shoaling, though reconstructed carbonate accumulation indicates an increase during the MMCO compared to the modern, consistent with an enhanced silicate weathering feedback (Si and Rosenthal, 2019; Si et al., 2023).

### Transitions

We distinguish climate transitions as changes that occur on the order of $10^5$ yrs. (consistent with the residence time of carbon in the surface reservoir, Eq. 58), but fail to recover or reverse over the silicate weathering timescale (Eq. 56). Transitions are distinct from trends in that they occur more rapidly; hence a cooling trend is apparent across the early-middle Eocene following the EECO but the MMCO was followed more abruptly by the mid-Miocene Climate Transition at ~14 Ma (Super et al., 2018). Trends should be clearly longer than the silicate weathering timescale, but insufficient resolution in proxy records may make some transitions appear as trends; in contrasting the end of EECO and the MMCO, the resolution and number of available records is greater for the latter. Open system carbon cycle exchanges must be considered in understanding the establishment of a new steady state, but the transition itself suggests an interval in which open system exchanges were out of balance. Westerhold et al. (2020) identify key climatic transitions during the Cenozoic as the Eocene Oligocene Transition (EOT or Oi-1, ~34 Ma), the Oligocene Miocene Transition (OMT or Mi-1, ~23 Ma), the middle Miocene Climate Transition (mmCT, ~14 Ma), the Pliocene-Pleistocene Climate Transition (~2.7 Ma), and the Mid-Pleistocene Transition (MPT, ~1.2 Ma). Of these, the most recent, Mid-Pleistocene Transition is explicitly related to the character of the climate and carbon cycle response to orbital forcing; it describes the transition from 41-kyr glacial-interglacial cycles to ~100-kyr cycles (Berends et al., 2021). Continuous ice core records do not yet span the MPT, but discontinuous ice core samples and $\delta^{11}B$-based $CO_2$ reconstructions do not conclusively indicate a long-term decline, but rather lower glacial $CO_2$ levels (Hönisch et al., 2009; Chalk et al., 2017; Yan et al., 2019). However, there is evidence connecting the earlier transitions to orbital forcing as well. In particular, glacial transitions appear to correlate to low-amplitude obliquity and eccentricity minima, which favor cool summers and ice accumulation (Zachos et al., 2001; Galeotti et al., 2016; Greenop et al., 2019). Broadly, transitions hence result from a combination of open system imbalances and rhythmic forcing, suggestive of thresholds in the carbon cycle and climate system that once crossed permanently transition the steady state conditions of the Earth System.

### Aberrations

The Paleocene-Eocene Thermal Maximum (PETM, ~56 Ma) is unique in the Cenozoic for the magnitude and rate of change in the carbon cycle and climate; alongside anthropogenic $CO_2$ release, it stands out as an aberration of the carbon cycle and climate system. Climate aberrations are abrupt disruptions to the carbon cycle that do not drive a change in steady state; instead, the system recovers over the silicate weathering timescale (Eq. 56; Figs. 5 and 9). The establishment of Antarctic Ice across the EOT and the OMT have been described as a climate aberrations (Zachos et al., 2001), but the lack of recovery in benthic $\delta^{18}O$ suggests that these are better understood as transitions to a new climatic state, potentially influenced by climate factors, like ice sheets, that act in addition to changes in open-system carbon fluxes (e.g. the shift from Warmhouse to Coolhouse across the EOT, Westerhold et al., 2020).

During the PETM, global temperature rose by ~6 °C (Tierney et al., 2022) as a consequence of massive emissions of $^{13}C$-depleted carbon to the atmosphere and oceans that generated a global negative $\delta^{13}C$ excursion in carbonates and organic matter (McInerney and Wing, 2011). While two detailed planktic foraminiferal $\delta^{11}B$ records exist across the PETM, uncertainty in the ocean carbonate system translates into uncertainty in reconstructed $CO_2$ across the event, with estimates for pre-PETM to PETM $CO_2$ concentrations ranging by a few hundred ppm (Tierney et al., 2022; Inglis et al., 2020). During the PETM, atmospheric $CO_2$ may have doubled (Tierney et al., 2022; Inglis et al., 2020; Gutjahr et al., 2017; Schubert and Hope Jahren, 2013); larger than the 1.5-fold $CO_2$ rise during late Pleistocene ice age terminations. While significant debate exists regarding the onset duration of the PETM (Turner, 2018), rates of carbon emissions within the Cenozoic Era have only exceeded the PETM as a result of ongoing anthropogenic fossil fuel burning (Zeebe et al., 2016).

Early estimates of the amount of carbon required to explain the global PETM negative $\delta^{13}C$ excursion quickly discounted the possibility that the PETM was caused primarily by the redistribution of carbon within the surface carbon reservoirs (e.g. Dickens et al., 1995), and more recent estimates have tended to increase the estimated mass of emitted carbon (Cui et al., 2011; Gutjahr et al., 2017; Haynes and Hönisch, 2020). However, the rate of carbon emissions is important in relating the change in atmospheric $CO_2$ to the total mass of carbon emitted. Due to the counteracting influence of a strengthened weathering feedback (von Strandmann et al., 2021) a slower rate of carbon addition means that more total carbon must be added to generate an equivalent

rise in atmospheric $CO_2$ (Vervoort et al., 2019). Various approaches have been used to constrain the rate of carbon addition across the PETM (Turner, 2018), and consensus is emerging for a duration of carbon release between $10^3$ and $10^4$ years.

In other words, PETM carbon release occurred within the closed system timescale but the ultimate recovery was due to open system processes. Our illustrative carbon release experiments in cGENIE for anthropogenic carbon release are thus conceptually very similar to possible PETM scenarios even though the late Paleocene carbon cycle differed in key ways from the modern, including the ocean's major ion composition (lower $Mg^{2+}$ and higher $Ca^{2+}$ concentrations) and lower alkalinity (Tyrrell and Zeebe, 2004; Hain et al., 2015; Boudreau et al., 2019).

### *Variability*

The recent geologic record provides a wealth of examples for coupling between the carbon cycle and climate on short (ca. 1000-years or less) timescales. This variability in the carbon cycle and climate may or may not be quasi-periodic and may or may not involve external forcing. Examples of the coupled carbon cycle connection to climate variability include the millennial-scale Daansgard-Oeschger and Heinrich events studied within the last glacial and similar events occurring in the early Holocene (e.g. Menviel et al., 2015; Zhang et al., 2017; Martens et al., 2020; Bauska et al., 2021; Jochum et al., 2022). Internal modes of variability also interact with the carbon cycle; for instance, warm-anomaly ENSO years are associated with weakening land carbon sinks (Betts et al., 2020). Because this variability involves changes that occur over a millennial or shorter timescale, these events do not cause an open system carbon cycle response. However, we are only beginning to scratch the surface in understanding how these dynamics occur within different time periods and under different background climate conditions.

## Summary statement

The long-term stability of the global carbon cycle is the result of dynamic balances that arise through negative feedbacks that all act together to determine how carbon is partitioned in space and between different chemical forms on Earth, including the atmospheric greenhouse gasses $CO_2$ and methane. The global carbon cycle hence influences Earth's climate. Moreover, most of the feedbacks within the carbon cycle are themselves influenced by or even require climate change for their operation. This complex coupling between carbon biogeochemistry and physical climate is an emergent property of Earth that cannot be predicted by examining any of its parts or processes in isolation, but rather arises from all its interactions. As such, climate-carbon cycle feedbacks can be measured only indirectly and numerical models struggle to capture their complexity in simulating past, present or future Earth. The best chance we have to quantify, represent and understand these feedbacks is through reconstructing their operation at different timescales through geologic time. The picture that emerges suggests we should be wary of carbon cycle feedbacks when attempting solutions to anthropogenic climate change that do not address stewardship of the comprehensive carbon cycle.

Much of what we know with some confidence about coupled changes in the climate and carbon cycle comes from studying the record of continuous deep sea sediments and the chemical, isotopic and biological proxy evidence of both climate and carbon cycle changes that they hold. Proxies and proxy-systems have advanced in parallel to the Deep Sea Drilling Project (DSDP, 1966–1983), Ocean Drilling Program (ODP, 1983–2003), Integrated Ocean Drilling Program (IODP, 2003–2013), and International Ocean Discovery Program (2014–2024), offering robust and highly successful platforms for the retrieval of sample material form deeply buried sediment sequences on the deep ocean seafloor. Recent development of new climate and carbon cycle proxies, particularly for seawater carbonate chemistry, is promising more detailed information on past carbon cycle dynamics. Increasingly rigorous combination of proxy data with climate models highlights the crucial need for improvements in spatial coverage through time. Developing effective strategies to make best use of the available legacy material and planning for future platforms to acquire new sample material are key priorities of the paleoclimate and paleoceanographic research community.

New insights are likely to come from systematic data aggradation and data-driven modeling. Particular areas deserving of synthesis studies include (1) constraints on Earth System Sensitivity from geologic intervals with varying climate states; (2) reconstruction of $CaCO_3$ burial, changes in saturation state, and changes in weathering through time; (3) reconstruction of organic carbon burial and constraints on the recycling of organic carbon after it has been buried; and (4) reconstruction of the production of organic carbon and carbonate and the connection to evolution and changes in community composition through time. In general, improved spatial and temporal coverage are a priority–for example, proxy records of $CO_2$ that can resolve climate rhythms throughout the Cenozoic.

Both data synthesis and integration of proxy data with models should allow the scientific community to increase the rigor of defining past carbon cycle and climate trends, optima, transitions, rhythms, aberrations, and variability. More precise definitions can aid the integration of data-driven and modeling approaches to study past interactions between the carbon cycle and climate. For example, if climatic optima are defined by warming that persists timescales longer than the silicate weathering feedback, this should distinguish modeling studies of optima versus aberrations in the climate system; the former involves steady state open system fluxes while the latter involves a system transiently pushed out of steady state. Improvements in numerical modeling will increasingly allow the representation of a more comprehensive carbon cycle in models of increasing complexity. A key challenge will remain how to address processes that generally operate over slow, open system timescales, but have the potential to be perturbed more rapidly as a consequence of human activities, either accidentally or due to deliberate attempts to affect Earth's geological carbon cycle through technologies like enhanced weathering or geological carbon sequestration by enhanced mineral hydration and carbonation reactions.

## References


Ai XE, Studer AS, Sigman DM, Martínez-García A, Fripiat F, Thöle LM, Michel E, et al. (2020) Southern ocean upwelling, Earth's obliquity, and glacial-interglacial atmospheric $CO_2$ change. *Science* 370(6522): 1348–1352. https://doi.org/10.1126/science.abd2115.

Aiuppa A, Fischer TP, Plank T, and Bani P (2019) CO2 flux emissions from the Earth's most actively degassing volcanoes, 2005–2015. *Scientific Reports* 9(1): 5442. https://doi.org/10.1038/s41598-019-41901-y.

Allen KA, Hönisch B, Eggins SM, Jimin Y, Spero HJ, and Elderfield H (2011) Controls on boron incorporation in cultured tests of the planktic Foraminifer Orbulina Universa. *Earth and Planetary Science Letters* 309(3–4): 291–301. https://doi.org/10.1016/j.epsl.2011.07.010.

Allen KA, Hönisch B, Eggins SM, and Rosenthal Y (2012) Environmental controls on B/Ca in calcite tests of the tropical planktic foraminifer species Globigerinoides Ruber and Globigerinoides Sacculifer. *Earth and Planetary Science Letters* 351–352: 270–280. https://doi.org/10.1016/j.epsl.2012.07.004.

Andel V and Tjeerd H (1975) Mesozoic/Cenozoic calcite compensation depth and the global distribution of calcareous sediments. *Earth and Planetary Science Letters* 26(2): 187–194. https://doi.org/10.1016/0012-821X(75)90086-2.

Archer D (1996a) A data-driven model of the global calcite lysocline. *Global Biogeochemical Cycles* 10(3): 511–526. https://doi.org/10.1029/96GB01521.

Archer DE (1996b) An Atlas of the distribution of calcium carbonate in sediments of the deep sea. *Global Biogeochemical Cycles* 10(1): 159–174. https://doi.org/10.1029/95GB03016.

Archer DE, Morford JL, and Emerson SR (2002) A model of suboxic sedimentary diagenesis suitable for automatic tuning and gridded global domains. *Global Biogeochemical Cycles* 16(1). https://doi.org/10.1029/2000GB001288.

Archer D, Eby M, Brovkin V, Ridgwell A, Cao L, Mikolajewicz U, Caldeira K, et al. (2009) Atmospheric lifetime of fossil fuel carbon dioxide. *Annual Review of Earth and Planetary Sciences* 37(1): 117–134. https://doi.org/10.1146/annurev.earth.031208.100206.

Auderset A, Moretti S, Taphorn B, Ebner P-R, Kast E, Wang XT, Schiebel R, Sigman DM, Haug GH, and Martínez-García A (2022) Enhanced ocean oxygenation during cenozoic warm periods. *Nature* 609(7925): 77–82. https://doi.org/10.1038/s41586-022-05017-0.

Bar-On YM, Phillips R, and Milo R (2018) The biomass distribution on Earth. *Proceedings of the National Academy of Sciences* 115(25): 6506–6511. https://doi.org/10.1073/pnas.1711842115.

Bauska TK, Baggenstos D, Brook EJ, Mix AC, Marcott SA, Petrenko VV, Schaefer H, Severinghaus JP, and Lee JE (2016) Carbon isotopes characterize rapid changes in atmospheric carbon dioxide during the last deglaciation. *Proceedings of the National Academy of Sciences* 113(13): 3465–3470. https://doi.org/10.1073/pnas.1513868113.

Bauska TK, Marcott SA, and Brook EJ (2021) Abrupt changes in the global carbon cycle during the last glacial period. *Nature Geoscience* 14(2): 91–96. https://doi.org/10.1038/s41561-020-00680-2.

Becker K, Austin J, Exon N, Humphris S, Kastner M, McKenzie J, Miller K, Suyehiro K, and Taira A (2019) Fifty years of scientific ocean drilling. *Oceanography* 32(1): 17–21. https://doi.org/10.5670/oceanog.2019.110.

Bemis BE, Spero HJ, Bijma J, and Lea DW (1998) Reevaluation of the oxygen isotopic composition of planktonic Foraminifera: Experimental results and revised paleotemperature equations. *Paleoceanography* 13(2): 150–160. https://doi.org/10.1029/98PA00070.

Ben-Yaakov S and Goldhaber MB (1973) The influence of sea water composition on the apparent constants of the carbonate system. *Deep Sea Research and Oceanographic Abstracts* 20(1): 87–99. https://doi.org/10.1016/0011-7471(73)90044-2.

Bereiter B, Egglestone S, Schmitt J, et al. (2015) Revision of the EPICA Dome C $CO_2$ record from 800 to 600 Kyr before present. *Geophysical Research Letters*. https://doi.org/10.1002/2014GL061957.

Berends CJ, Köhler P, Lourens LJ, and Van De Wal RSW (2021) On the cause of the mid-Pleistocene transition. *Reviews of Geophysics* 59(2): e2020RG000727. https://doi.org/10.1029/2020RG000727.

Berger WH (1970) Planktonic Foraminifera: Selective solution and the lysocline. *Marine Geology* 8(2): 111–138. https://doi.org/10.1016/0025-3227(70)90001-0.

Berner RA (1990) Atmospheric carbon dioxide levels over Phanerozoic time. *Science* 249: 1382–1386. https://doi.org/10.1126/science.249.4975.1382.

Berner RA (2006) GEOCARBSULF: A combined model for Phanerozoic atmospheric $O_2$ and $CO_2$. *Geochimica et Cosmochimica Acta* 70(23): 5653–5664. https://doi.org/10.1016/j.gca.2005.11.032.

Berner EK and Berner RA (1996) *Global Environment: Water, Air and Geochemical Cycles*. United States: Princeton University Press.

Berner RA, Lasaga AC, and Garrels RM (1983) The carbonate-silicate geochemical cycle and its effect on atmospheric carbon dioxide over the past 100 million years. *American Journal of Science* 283(7): 641–683. https://doi.org/10.2475/ajs.283.7.641.

Betts RA, Burton CA, Feely RA, Collins M, Jones CD, and Wiltshire AJ (2020) In: McPhaden MJ, Santoso A, and Cai W (eds.) *ENSO and the Carbon Cycle*. *Geophysical Monograph Series*, 1st edn, pp. 453–470. Wiley. https://doi.org/10.1002/9781119548164.ch20.

Bigeleisen J (1965) Chemistry of isotopes. *Science* 147(3657): 463–471.

Bijl PK, Houben AJP, Schouten S, Bohaty SM, Sluijs A, Reichart G-J, Sinninghe Damsté JS, and Brinkhuis H (2010) Transient middle Eocene atmospheric $CO_2$ and temperature variations. *Science* 330(6005): 819–821. https://doi.org/10.1126/science.1193654.

Blattmann TM, Liu Z, Zhang Y, Zhao Y, Haghipour N, Montluçon DB, Plötze M, and Eglinton TI (2019) Mineralogical control on the fate of continentally derived organic matter in the ocean. *Science* 366(6466): 742–745. https://doi.org/10.1126/science.aax5345.

Bolin B (1960) On the exchange of carbon dioxide between the atmosphere and the sea. *Tellus* 12(3): 274–281. https://doi.org/10.1111/j.2153-3490.1960.tb01311.x.

Bond-Lamberty B (2018) New techniques and data for understanding the global soil respiration flux. *Earth's Future* 6(9): 1176–1180. https://doi.org/10.1029/2018EF000866.

Boudreau BP, Middelburg JJ, Sluijs A, and Van Der Ploeg R (2019) Secular Variations in the carbonate chemistry of the oceans over the Cenozoic. *Earth and Planetary Science Letters* 512: 194–206. https://doi.org/10.1016/j.epsl.2019.02.004.

Bradley JA, Hülse D, LaRowe DE, and Arndt S (2022) Transfer efficiency of organic carbon in marine sediments. *Nature Communications* 13(1): 7297. https://doi.org/10.1038/s41467-022-35112-9.

Branson O (2018) Boron incorporation into marine $CaCO_3$. In: Marschall H and Foster G (eds.) *Boron Isotopes. Advances in Isotope Geochemistry*, pp. 71–105. Cham: Springer International Publishing. https://doi.org/10.1007/978-3-319-64666-4_4.

Broecker WS and Peng T-H (1982) *Tracers in the Sea*. Eldigo Press, Lamont-Doherty Geological Observatory. https://doi.org/10.1017/S0033822200005221.

Broecker WS and Takahashi T (1977) The solubility of calcite in sea water. In: Fraser DG (ed.) *Thermodynamics in Geology*, pp. 365–379. Dordrecht: Springer Netherlands. https://doi.org/10.1007/978-94-010-1252-2_18.

Broecker WS, Peng T-H, Ostlund G, and Stuiver M (1985) The distribution of bomb radiocarbon in the ocean. *Journal of Geophysical Research: Oceans* 90(C4): 6953–6970. https://doi.org/10.1029/JC090iC04p06953.

Broecker WS, Ledwell JR, Takahashi T, Weiss R, Merlivat L, Memery L, Peng T-H, Jahne B, and Munnich KO (1986) Isotopic versus micrometeorologic ocean $CO_2$ fluxes: A serious conflict. *Journal of Geophysical Research: Oceans* 91(C9): 10517–10527. https://doi.org/10.1029/JC091iC09p10517.

Brown RE, Anderson LD, Thomas E, and Zachos JC (2011) A core-top calibration of B/Ca in the Benthic Foraminifers Nuttallides Umbonifera and Oridorsalis Umbonatus: A proxy for Cenozoic bottom water carbonate saturation. *Earth and Planetary Science Letters* 310(3–4): 360–368. https://doi.org/10.1016/j.epsl.2011.08.023.

Burton MR, Sawyer GM, and Granieri D (2013) Deep carbon emissions from volcanoes. *Reviews in Mineralogy and Geochemistry* 75(1): 323–354. https://doi.org/10.2138/rmg.2013.75.11.

Caiafa L, Barros NO, and Lopes JFS (2023) Greenhouse gas emissions from ant nests: A systematic review. *Ecological Entomology*: een.13238. https://doi.org/10.1111/een.13238.

Campbell SM, Moucha R, Derry LA, and Raymo ME (2018) Effects of dynamic topography on the cenozoic carbonate compensation depth. *Geochemistry, Geophysics, Geosystems* 19: 1025–1034. https://doi.org/10.1002/2017gc007386.

Canadell JG, Monteiro PMS, et al. (2021) Global Carbon and Other Biogochemical Cycles and Feedbacks. *Climate Change 2021 – The Physical Science Basis*. IPCC. https://doi.org/10.1017/9781009157896.007.

Cao L, Eby M, Ridgwell A, Caldeira K, Archer D, Ishida A, Joos F, et al. (2009) The role of ocean transport in the uptake of anthropogenic $CO_2$. *Biogeosciences* 6(3): 375–390. https://doi.org/10.5194/bg-6-375-2009.

Catanzaro EJ, Champion CE, Garner EL, Marinenko G, Sappenfield KM, and Shields WR (1970) *Boric Acid; Isotopic, and Assay Standard Reference Materials*. National Bureau of Standards. https://nvlpubs.nist.gov/nistpubs/Legacy/SP/nbsspecialpublication260-17.pdf.

Caves JK, Jost AB, Lau KV, and Maher K (2016) Cenozoic carbon cycle imbalances and a variable weathering feedback. *Earth and Planetary Science Letters* 450: 152–163. https://doi.org/10.1016/j.epsl.2016.06.035.

Cember R (1989) Bomb radiocarbon in the Red Sea: A medium-scale gas exchange experiment. *Journal of Geophysical Research: Oceans* 94(C2): 2111–2123. https://doi.org/10.1029/JC094iC02p02111.

Chalk TB, Hain MP, Foster GL, Rohling EJ, Sexton PF, Badger MPS, Cherry SG, et al. (2017) Causes of Ice Age intensification across the mid-Pleistocene transition. *Proceedings of the National Academy of Sciences* 114(50): 13114–13119. https://doi.org/10.1073/pnas.1702143114.

Chang S and Berner RA (1999) Coal weathering and the geological carbon cycle. *Geochimica et Cosmochimica Acta* 63(19–20): 3301–3310. https://doi.org/10.1016/S0016-7037(99)00252-5.

Clegg SL, Waters JF, Turner DR, and Dickson AG (2023) Chemical speciation models based upon the Pitzer activity coefficient equations, including the propagation of uncertainties. III. Seawater from the freezing point to 45°C, including acid-base equilibria. *Marine Chemistry* 250: 104196. https://doi.org/10.1016/j.marchem.2022.104196.

Craig H (1957) Isotopic standards for carbon and oxygen and correction factors for mass-spectrometric analysis of carbon dioxide. *Geochimica et Cosmochimica Acta* 12(1–2): 133–149. https://doi.org/10.1016/0016-7037(57)90024-8.

Cramer BS, Miller KG, Barrett PJ, and Wright JD (2011) Late Cretaceous–Neogene trends in deep ocean temperature and continental ice volume: Reconciling records of Benthic Foraminiferal geochemistry ($\delta^{18}$ O and Mg/Ca) with sea level history. *Journal of Geophysical Research* 116(C12): C12023. https://doi.org/10.1029/2011JC007255.

Cui Y, Kump LR, Ridgwell AJ, Charles AJ, Junium CK, Diefendorf AF, Freeman KH, Urban NM, and Harding IC (2011) Slow release of fossil carbon during the Palaeocene–Eocene thermal maximum. *Nature Geoscience* 4(7): 481–485. https://doi.org/10.1038/ngeo1179.

Dansgaard W (1964) Stable isotopes in precipitation. *Tellus* 16: 436–468. https://doi.org/10.3402/tellusa.v16i4.8993.

Der Meer V, Douwe G, Zeebe RE, Van Hinsbergen DJJ, Sluijs A, Spakman W, and Torsvik TH (2014) Plate tectonic controls on atmospheric $CO_2$ levels since the Triassic. *Proceedings of the National Academy of Sciences* 111(12): 4380–4385. https://doi.org/10.1073/pnas.1315657111.

Der Ploeg V, Robin BP, Boudreau JJ, and Middelburg, and Appy Sluijs. (2019) Cenozoic carbonate burial along continental margins. *Geology* 47(11): 1025–1028. https://doi.org/10.1130/G46418.1.

Derry LA (2022) Carbonate weathering, $CO_2$ redistribution, and Neogene CCD and $pCO_2$ evolution. *Earth and Planetary Science Letters* 597: 117801. https://doi.org/10.1016/j.epsl.2022.117801.

Dickens GR, O'Neil JR, Rea DK, and Owen RM (1995) Dissociation of oceanic methane hydrate as a cause of the carbon isotope excursion at the end of the Paleocene. *Paleoceanography* 10(6): 965–971. https://doi.org/10.1029/95PA02087.

Dickson AG (1981) An exact definition of total alkalinity and a procedure for the estimation of alkalinity and total inorganic carbon from titration data. *Deep Sea Research Part A. Oceanographic Research Papers* 28(6): 609–623. https://doi.org/10.1016/0198-0149(81)90121-7.

Dickson AG (1990) Standard potential of the reaction: Agcl(s)+12$H_2$(g)=Ag(s)+HCl(aq), and the standard acidity constant of the ion HSO4−in synthetic sea water from 273.15 to 318.15 K. *The Journal of Chemical Thermodynamics* 22(2): 113–127. https://doi.org/10.1016/0021-9614(90)90074-Z.

Dickson AG, Sabine CL, Christian JR, Bargeron CP, and North Pacific Marine Science Organization (2007) *Guide to Best Practices for Ocean CO2 Measurements*. PICES Special Publication, no. 3, Sidney, BC: North Pacific Marine Science Organization.

Dunne JP, Sarmiento JL, and Gnanadesikan A (2007) A synthesis of global particle export from the surface ocean and cycling through the ocean interior and on the seafloor. *Global Biogeochemical Cycles* 21(4): 2006GB002907. https://doi.org/10.1029/2006GB002907.

Edgar KM, Anagnostou E, Pearson PN, and Foster GL (2015) Assessing the impact of diagenesis on δ11B, δ13C, δ18O, Sr/Ca and B/Ca values in fossil Planktic Foraminiferal calcite. *Geochimica et Cosmochimica Acta* 166: 189–209. https://doi.org/10.1016/j.gca.2015.06.018.

Eide M, Olsen A, Ninnemann US, and Eldevik T (2017) A global estimate of the full oceanic $^{13}$C Suess effect since the preindustrial. *Global Biogeochemical Cycles* 31(3): 492–514. https://doi.org/10.1002/2016GB005472.

Eiler JM (2007) 'Clumped-Isotope' geochemistry—The study of naturally-occurring, multiply-substituted isotopologues. *Earth and Planetary Science Letters* 262(3–4): 309–327. https://doi.org/10.1016/j.epsl.2007.08.020.

Emiliani C (1955) Pleistocene temperatures. *The Journal of Geology* 63(6): 538–578.

Emiliani C (1966) Isotopic paleotemperatures. *Science* 154(3751): 851–857.

Epstein S, Thompson P, and Yapp CJ (1977) Oxygen and hydrogen isotopic ratios in plant cellulose. *Science* 198(4323): 1209–1215. https://doi.org/10.1126/science.198.4323.1209.

Eriksson E and Welander P (1956) On a mathematical model of the carbon cycle in nature. *Tellus* 8(2): 155–175. https://doi.org/10.1111/j.2153-3490.1956.tb01207.x.

Fakhraee M, Tarhan LG, Planavsky NJ, and Reinhard CT (2021) A largely invariant marine dissolved organic carbon reservoir across Earth's history. *Proceedings of the National Academy of Sciences* 118(40): e2103511118. https://doi.org/10.1073/pnas.2103511118.

Farmer JR, Hertzberg JE, Cardinal D, Fietz S, Hendry K, Jaccard SL, Paytan A, et al. (2021) Assessment of C, N, and Si isotopes as tracers of past ocean nutrient and carbon cycling. *Global Biogeochemical Cycles* 35(7): e2020GB006775. https://doi.org/10.1029/2020GB006775.

Farquhar GD, Ehleringer JR, and Hubick KT (1989) Carbon isotope discrimination and photosynthesis. *Annual Review of Plant Physiology and Plant Molecular Biology* 40(1): 503–537. https://doi.org/10.1146/annurev.pp.40.060189.002443.

Farrell JW and Prell WL (1989) Climatic change and $CaCO_3$ preservation: An 800,000 year bathymetric reconstruction from the central equatorial Pacific Ocean. *Paleoceanography* 4(4): 447–466. https://doi.org/10.1029/PA004i004p00447.

Fatichi S, Pappas C, Zscheischler J, and Leuzinger S (2019) Modelling carbon sources and sinks in terrestrial vegetation. *New Phytologist* 221(2): 652–668. https://doi.org/10.1111/nph.15451.

Fedorov AV, Brierley CM, Lawrence KT, Liu Z, Dekens PS, and Ravelo AC (2013) Patterns and mechanisms of early Pliocene Warmth. *Nature* 496(7443): 43–49. https://doi.org/10.1038/nature12003.

Fischer TP, Arellano S, Carn S, Aiuppa A, Galle B, Allard P, Lopez T, et al. (2019) The emissions of CO2 and other volatiles from the world's subaerial volcanoes. *Scientific Reports* 9(1): 18716. https://doi.org/10.1038/s41598-019-54682-1.

Forchhammer G (1865) IV. On the composition of sea-water in the different parts of the ocean. *Philosophical Transactions of the Royal Society of London* 155: 203–262. https://doi.org/10.1098/rstl.1865.0004.

Foster GL, Pogge Von Strandmann PAE, and Rae JWB (2010) Boron and magnesium isotopic composition of seawater: DATA BRIEF. *Geochemistry, Geophysics, Geosystems* 11(8). https://doi.org/10.1029/2010GC003201.

Foster GL, Hönisch B, Paris G, Dwyer GS, Rae JWB, Elliott T, Jérôme Gaillardet N, Hemming G, Louvat P, and Vengosh A (2013) Interlaboratory comparison of boron isotope analyses of boric acid, seawater and marine CaCO3 by MC-ICPMS and NTIMS. *Chemical Geology* 358: 1–14. https://doi.org/10.1016/j.chemgeo.2013.08.027.

Friedlingstein P, O'Sullivan M, Jones MW, Andrew RM, Gregor L, Hauck J, Le Quéré C, et al. (2022) Global Carbon Budget 2022. *Earth System Science Data* 14(11): 4811–4900. https://doi.org/10.5194/essd-14-4811-2022.

Fritsch E, Balan E, Do Nascimento NR, Allard T, Bardy M, Bueno G, Derenne S, Melfi AJ, and Calas G (2011) Deciphering the weathering processes using environmental mineralogy and geochemistry: Towards an integrated model of laterite and podzol genesis in the upper Amazon basin. *Comptes Rendus Geoscience* 343(2–3): 188–198. https://doi.org/10.1016/j.crte.2010.11.002.

Galeotti S, DeConto R, Naish T, Stocchi P, Florindo F, Pagani M, Barrett P, et al. (2016) Antarctic ice sheet variability across the Eocene-Oligocene boundary climate transition. *Science* 352(6281): 76–80. https://doi.org/10.1126/science.aab0669.

Galili N, Shemesh A, Yam R, Brailovsky I, Sela-Adler M, Schuster EM, Collom C, et al. (2019) The geologic history of seawater oxygen isotopes from marine iron oxides. *Science* 365(6452): 469–473. https://doi.org/10.1126/science.aaw9247.

Gaskell DE and Hull PM (2023) Technical note: A new online tool for $\delta^{18}$ O–Temperature conversions. *Climate of the Past* 19(6): 1265–1274. https://doi.org/10.5194/cp-19-1265-2023.

Geyman EC, Wu Z, Nadeau MD, Edmonsond S, Turner A, Purkis SJ, Howes B, et al. (2022) The origin of carbonate mud and implications for global climate. *Proceedings of the National Academy of Sciences* 119(43): e2210617119. https://doi.org/10.1073/pnas.2210617119.

Gough CM (2011) Terrestrial primary production: Fuel for life. *Nature Education Knowledge* 2(10): 28.

Greene SE, Ridgwell A, Kirtland Turner S, Schmidt DN, Pälike H, Thomas E, Greene LK, and Hoogakker BAA (2019) Early Cenozoic decoupling of climate and carbonate compensation depth trends. *Paleoceanography and Paleoclimatology* 34(6): 930–945. https://doi.org/10.1029/2019PA003601.

Greenop R, Hain MP, Sosdian SM, Oliver KIC, Goodwin P, Chalk TB, Lear CH, Wilson PA, and Foster GL (2017) A record of Neogene seawater $\Delta^{11}$B reconstructed from paired $\Delta^{11}$B analyses on Benthic and Planktic Foraminifera. *Climate of the Past* 13(2): 149–170. https://doi.org/10.5194/cp-13-149-2017.

Greenop R, Sosdian SM, Henehan MJ, Wilson PA, Lear CH, and Foster GL (2019) Orbital forcing, ice volume, and $CO_2$ across the Oligocene-Miocene transition. *Paleoceanography and Paleoclimatology* 34(3): 316–328. https://doi.org/10.1029/2018PA003420.

Grew ES (2017) Boron: From cosmic scarcity to 300 minerals. *Elements* 13(4): 225–229. https://doi.org/10.2138/gselements.13.4.225.

Gröning M, van Duren M, and Andreescu L (2006) Metrological characteristics of the conventional measurement scales for hydrogen and oxygen stable isotope amount ratios: The δ-scales. In: *Proceedings of an International Workshop on "Combining and Reporting Analytical Results: The Role of Traceability and Uncertainty for Comparing Analytical Results*, pp. 62–72. Royal Society of Chemistry.

Grotzinger JP (ed.) (2000) *Carbonate Sedimentation and Diagenesis in the Evolving Precambrian World*. Tulsa, Okla: SEPM (Society of Sedimentary Geology). SEPM Special Publication 67.

Gruber N, Bakker DCE, DeVries T, Gregor L, Hauck J, Landschützer P, McKinley GA, and Müller JD (2023) Trends and variability in the ocean carbon sink. *Nature Reviews Earth and Environment* 4(2): 119–134. https://doi.org/10.1038/s43017-022-00381-x.

Guinoiseau D, Fekiacova Z, Allard T, Druhan JL, Balan E, and Bouchez J (2021) Tropical weathering history recorded in the silicon isotopes of lateritic weathering profiles. *Geophysical Research Letters* 48(19): e2021GL092957. https://doi.org/10.1029/2021GL092957.

Gutjahr M, Ridgwell A, Sexton PF, Anagnostou E, Pearson PN, Pälike H, Norris RD, Thomas E, and Foster GL (2017) Very large release of mostly volcanic carbon during the Palaeocene–Eocene thermal maximum. *Nature* 548(7669): 573–577. https://doi.org/10.1038/nature23646.

Hain MP and Sigman DM (2024) $CO_2$ in Earth's ice age cycles. In: Dolman H (ed.) *Oxford Research Encyclopedia on Climate Science: $CO_2$ in the Climate System*. Oxford, UK: Oxford University Press. In press.

Hain MP, Sigman DM, and Haug GH (2010) Carbon dioxide effects of Antarctic stratification, North Atlantic intermediate water formation, and sub-Antarctic nutrient drawdown during the last Ice Age: Diagnosis and synthesis in a geochemical box model: Atmospheric $CO_2$ during the last Ice Age. *Global Biogeochemical Cycles* 24(4). https://doi.org/10.1029/2010GB003790.

Hain MP, Sigman DM, and Haug GH (2014) The biological pump in the past. In: *Treatise on Geochemistry*, pp. 485–517. Elsevier. https://doi.org/10.1016/B978-0-08-095975-7.00618-5.

Hain MP, Sigman DM, Higgins JA, and Haug GH (2015) The effects of secular calcium and magnesium concentration changes on the thermodynamics of seawater acid/base chemistry: Implications for Eocene and Cretaceous ocean carbon chemistry and buffering. *Global Biogeochemical Cycles* 29(5): 517–533. https://doi.org/10.1002/2014GB004986.

Hain MP, Foster GL, and Chalk T (2018) Robust constraints on past $CO_2$ climate forcing from the boron isotope proxy. *Paleoceanography and Paleoclimatology* 33(10): 1099–1115. https://doi.org/10.1029/2018PA003362.

Hansell DA (2013) Recalcitrant dissolved organic carbon fractions. *Annual Review of Marine Science* 5(1): 421–445. https://doi.org/10.1146/annurev-marine-120710-100757.

Hayes JM (2004) *An Introduction to Isotopic Calculations*. Woods Hole Oceanographic Institution. https://www.whoi.edu/cms/files/jhayes/2005/9/IsoCalcs30Sept04_5183.pdf.

Haynes LL and Hönisch B (2020) The seawater carbon inventory at the Paleocene–Eocene thermal maximum. *Proceedings of the National Academy of Sciences* 117(39): 24088–24095. https://doi.org/10.1073/pnas.2003197117.

Hedges JI and Keil RG (1995) Sedimentary organic matter preservation: An assessment and speculative synthesis. *Marine Chemistry* 49(2–3): 81–115. https://doi.org/10.1016/0304-4203(95)00008-F.

Hélie J-F, Adamowicz-Walczak A, Middlestead P, Chartrand MMG, Mester Z, and Meija J (2021) Discontinuity in the realization of the Vienna Peedee Belemnite Carbon Isotope Ratio Scale. *Analytical Chemistry* 93: 10740–10743. https://doi.org/10.1021/acs.analchem.1c02458.

Hemming NG and Hanson GN (1992) Boron isotopic composition and concentration in modern marine carbonates. *Geochimica et Cosmochimica Acta* 56(1): 537–543. https://doi.org/10.1016/0016-7037(92)90151-8.

Henehan MJ, Foster GL, Rae JWB, Prentice KC, Erez J, Bostock HC, Marshall BJ, and Wilson PA (2015) Evaluating the utility of B/C a ratios in planktic foraminifera as a proxy for the carbonate system: A case study of *G Lobigerinoides Ruber*. *Geochemistry, Geophysics, Geosystems* 16(4): 1052–1069. https://doi.org/10.1002/2014GC005514.

Henehan MJ, Klein CD, Gebbinck JVB, Wyman MP, Hain JWB, Rae BH, Foster GL, and Kim S-T (2022) No ion is an island: Multiple ions influence boron incorporation into $CaCO_3$. *Geochimica et Cosmochimica Acta* 318: 510–530. https://doi.org/10.1016/j.gca.2021.12.011.

Hilton RG and Joshua West A (2020) Mountains, erosion and the carbon cycle. *Nature Reviews Earth and Environment* 1(6): 284–299. https://doi.org/10.1038/s43017-020-0058-6.

Hodell DA and Venz-Curtis KA (2006) Late Neogene history of deepwater ventilation in the Southern Ocean. *Geochemistry, Geophysics, Geosystems* 7(9): 2005GC001211. https://doi.org/10.1029/2005GC001211.

Hoffman DW and Rasmussen C (2022) Absolute carbon stable isotope ratio in the Vienna Peedee Belemnite isotope reference determined by $^{1}$H NMR spectroscopy. *Analytical Chemistry* 94(13): 5240–5247. https://doi.org/10.1021/acs.analchem.1c04565.

Hoffman PF, Kaufman AJ, Halverson GP, and Schrag DP (1998) A Neoproterozoic snowball Earth. *Science* 281(5381): 1342–1346. https://doi.org/10.1126/science.281.5381.1342.

Holbourn A, Kuhnt W, Kochhann KGD, Andersen N, and Sebastian Meier KJ (2015) Global perturbation of the carbon cycle at the onset of the Miocene climatic optimum. *Geology* 43(2): 123–126. https://doi.org/10.1130/G36317.1.

Hönisch B, Gary Hemming N, Archer D, Siddall M, and McManus JF (2009) Atmospheric carbon dioxide concentration across the mid-Pleistocene transition. *Science* 324(5934): 1551–1554. https://doi.org/10.1126/science.1171477.

Hönisch B, Eggins SM, Haynes LL, Allen KA, Holland KD, and Lorbacher K (2019) *Boron Proxies in Paleoceanography and Paleoclimatology*, 1st edn. Wiley. https://doi.org/10.1002/9781119010678.

Hönisch B, Fish CR, Phelps SR, Haynes LL, Dyez K, Holland K, Fehrenbacher J, Allen KA, Eggins SM, and Goes JI (2021) Symbiont photosynthesis and its effect on boron proxies in Planktic Foraminifera. *Paleoceanography and Paleoclimatology* 36(10): e2020PA004022. https://doi.org/10.1029/2020PA004022.

Hönisch B, Royer DL, Breecker DO, Polissar PJ, Bowen GJ, Henehan MJ, Cui Y, et al. (2023) Toward a Cenozoic history of atmospheric $CO_2$. *Science* 382(6675): eadi5177. https://doi.org/10.1126/science.adi5177.

Hoogakker B, Davis C, Wang Y, Kusch S, Nilsson-Kerr K, Hardisty D, Jacobel A, et al. (2024) Reviews and syntheses: Review of proxies for low-oxygen paleoceanographic reconstructions. Preprint, In: *Paleobiogeoscience: Proxy use, Development & Validation*. https://doi.org/10.5194/egusphere-2023-2981.

Horner TJ, Little SH, Conway TM, Farmer JR, Hertzberg JE, Janssen DJ, Lough AJM, et al. (2021) Bioactive trace metals and their isotopes as paleoproductivity proxies: An assessment using GEOTRACES-Era data. *Global Biogeochemical Cycles* 35(11): e2020GB006814. https://doi.org/10.1029/2020GB006814.

Hülse D, Arndt S, Wilson JD, Munhoven G, and Ridgwell A (2017) Understanding the causes and consequences of past marine carbon cycling variability through models. *Earth-Science Reviews* 171: 349–382. https://doi.org/10.1016/j.earscirev.2017.06.004.

Humphreys MP, Lewis ER, Sharp JD, and Pierrot D (2021) PyCO2SYS v1.8: Marine carbonate system calculations in Python. *Geoscientific Model Development* 15: 15–43. https://doi.org/10.5194/gmd-15-15-2022.

Hut G (1987) *Stable Isotope Reference Samples for Geochemical and Hydrologic Investigations*. International Atomic Energy Agency. https://nucleus.iaea.org/sites/ReferenceMaterials/Shared%20Documents/Publications/SI_meetings/IAEA-1987-Hut_CMeeting-StableIsotopeRM.pdf.

Inglis GN, Bragg F, Burls NJ, Cramwinckel MJ, Evans D, Foster GL, Huber M, et al. (2020) Global mean surface temperature and climate sensitivity of the early Eocene climatic optimum (EECO), Paleocene–Eocene thermal maximum (PETM), and latest Paleocene. *Climate of the Past* 16(5): 1953–1968. https://doi.org/10.5194/cp-16-1953-2020.

IOC, SCOR and IAPSO (2010) *The International Thermodynamic Equation of Seawater—2010: Calculation and Use of Thermodynamic Properties*. Manuals and Guides, No. 56, UNESCO.

IPCC and IPCC. (2021) *Climate Change 2021: The Physical Science Basis. Contribution of Working Group I to the Sixth Assessment Report of the Intergovernmental Panel on Climate Change*. Masson-Delmotte V, Zhai P, Pirani A, Connors SL, Péan C, Berger S, Caud N, Chen Y, Goldfarb L, Gomis MI, Huang M, Leitzell K, Lonnoy E, Matthews JBR, Maycock TK, Waterfield T, Yelekçi O, R. Yu, and Zhou B (eds.). *10.1017/9781009157896*. Cambridge, United Kingdom and New York, NY: Cambridge University Press. https://doi.org/10.1017/9781009157896.

Isson TT and Planavsky NJ (2018) Reverse weathering as a long-term stabilizer of marine pH and planetary climate. *Nature* 560(7719): 471–475. https://doi.org/10.1038/s41586-018-0408-4.

Ito T and Follows MJ (2005) Preformed phosphate, soft tissue pump and atmospheric $CO_2$. *Journal of Marine Research* 63(4): 813–839. https://doi.org/10.1357/0022240054663231. https://elischolar.library.yale.edu/journal_of_marine_research/102/.

Jian J, Bailey V, Dorheim K, Konings AG, Hao D, Shiklomanov AN, Snyder A, et al. (2022) Historically inconsistent productivity and respiration fluxes in the global terrestrial carbon cycle. *Nature Communications* 13(1): 1733. https://doi.org/10.1038/s41467-022-29391-5.

Jiao N, Herndl GJ, Hansell DA, Benner R, Kattner G, Wilhelm SW, Kirchman DL, et al. (2010) Microbial production of recalcitrant dissolved organic matter: Long-term carbon storage in the global ocean. *Nature Reviews Microbiology* 8(8): 593–599. https://doi.org/10.1038/nrmicro2386.

Jin X, Gruber N, Dunne JP, Sarmiento JL, and Armstrong RA (2006) Diagnosing the contribution of phytoplankton functional groups to the production and export of particulate organic carbon, $CaCO_3$, and opal from global nutrient and alkalinity distributions. *Global Biogeochemical Cycles* 20(2): 2005GB002532. https://doi.org/10.1029/2005GB002532.

Jochum M, Chase Z, Nuterman R, Pedro J, Rasmussen S, Vettoretti G, and Zheng P (2022) Carbon fluxes during Dansgaard–Oeschger events as simulated by an Earth system model. *Journal of Climate* 35(17): 5745–5758. https://doi.org/10.1175/JCLI-D-21-0713.1.

Jones MW, Santín C, van der Werf GR, and Doerr SH (2019) Global fire emissions buffered by the production of pyrogenic carbon. *Nature Geoscience* 12(9): 742–747. https://doi.org/10.1038/s41561-019-0403-x.

Joos F, Colin Prentice I, Sitch S, Meyer R, Hooss G, Plattner G-K, Gerber S, and Hasselmann K (2001) Global warming feedbacks on terrestrial carbon uptake under the Intergovernmental Panel on Climate Change (IPCC) emission scenarios. *Global Biogeochemical Cycles* 15(4): 891–907. https://doi.org/10.1029/2000GB001375.

Joos F, Roth R, Fuglestvedt JS, Peters GP, Enting IG, von Bloh W, Brovkin V, et al. (2013) Carbon dioxide and climate impulse response functions for the computation of greenhouse gas metrics: A multi-model analysis. *Atmospheric Chemistry and Physics* 13(5): 2793–2825. https://doi.org/10.5194/acp-13-2793-2013.

Kasbohm J and Schoene B (2018) Rapid eruption of the Columbia River flood basalt and correlation with the mid-Miocene climate optimum. *Science Advances* 4(9): eaat8223. https://doi.org/10.1126/sciadv.aat8223.

Kashiwagi H, Ogawa Y, and Shikazono N (2008) Relationship between weathering, mountain uplift, and climate during the Cenozoic as deduced from the global carbon–strontium cycle model. *Palaeogeography, Palaeoclimatology, Palaeoecology* 270(1–2): 139–149. https://doi.org/10.1016/j.palaeo.2008.09.005.

Kast ER, Stolper DA, Auderset A, Higgins JA, Ren H, Wang XT, Martínez-García A, Haug GH, and Sigman DM (2019) Nitrogen isotope evidence for expanded ocean suboxia in the early Cenozoic. *Science* 364(6438): 386–389. https://doi.org/10.1126/science.aau5784.

Keir RS (1988) On the late Pleistocene ocean geochemistry and circulation. *Paleoceanography* 3(4): 413–445. https://doi.org/10.1029/PA003i004p00413.

Kennett JP, Houtz RE, et al. (1975) *Initial Reports of the Deep Sea Drilling Project, 29*, vol. 29. U.S. Government Printing Office. https://doi.org/10.2973/dsdp.proc.29.1975. Initial Reports of the Deep Sea Drilling Project.

Kim S-T, Coplen TB, and Horita J (2015) Normalization of stable isotope data for carbonate minerals: Implementation of IUPAC guidelines. *Geochimica et Cosmochimica Acta* 158: 276–289. https://doi.org/10.1016/j.gca.2015.02.011.

Klochko K, Kaufman AJ, Yao W, Byrne RH, and Tossell JA (2006) Experimental measurement of boron isotope fractionation in seawater. *Earth and Planetary Science Letters* 248(1–2): 276–285. https://doi.org/10.1016/j.epsl.2006.05.034.

Kochhann KGD, Holbourn A, Kuhnt W, Channell JET, Lyle M, Shackford JK, Wilkens RH, and Andersen N (2016) Eccentricity pacing of eastern equatorial pacific carbonate dissolution cycles during the Miocene climatic optimum. *Paleoceanography* 31(9): 1176–1192. https://doi.org/10.1002/2016PA002988.

Komar N and Zeebe RE (2021) Reconciling atmospheric $CO_2$, weathering, and calcite compensation depth across the Cenozoic. *Science Advances* 7(4): eabd4876. https://doi.org/10.1126/sciadv.abd4876.

Komar N, Zeebe RE, and Dickens GR (2013) Understanding long-term carbon cycle trends: The late Paleocene through the early Eocene: PALEOCENE-EOCENE LONG-TERM CARBON CYCLE. *Paleoceanography* 28(4): 650–662. https://doi.org/10.1002/palo.20060.

Kump LR (1991) Interpreting carbon-isotope excursions: Strangelove oceans. *Geology* 19(4): 299. https://doi.org/10.1130/0091-7613(1991)019<0299:ICIESO>2.3.CO;2.

Kump LR (1999) Interpreting carbon-isotope excursions: Carbonates and organic matter. *Chemical Geology* 161(1–3): 181–198. https://doi.org/10.1016/S0009-2541(99)00086-8.

Kump LR and Arthur MA (1997) Global chemical erosion during the Cenozoic: Weatherability balances the budgets. In: Ruddiman WF (ed.) *Tectonic Uplift and Climate Change*, pp. 399–426. Boston, MA: Springer US. https://doi.org/10.1007/978-1-4615-5935-1_18.

Kwon EY, Sarmiento JL, Toggweiler JR, and DeVries T (2011) The control of atmospheric $p\,CO_2$ by ocean ventilation change: The effect of the oceanic storage of biogenic carbon: Ventilation control of atmospheric $CO_2$. *Global Biogeochemical Cycles* 25(3). https://doi.org/10.1029/2011GB004059.

Langmuir CH and Broecker W (2012) *How to Build a Habitable Planet: The Story of Earth from the Big Bang to Humankind*, Revised and Expanded Edition. Princeton University Press. https://doi.org/10.2307/j.ctt1r2f84.

Le J and Shackleton NJ (1992) Carbonate dissolution fluctuations in the western equatorial pacific during the late Quaternary. *Paleoceanography* 7(1): 21–42. https://doi.org/10.1029/91PA02854.

Lee K, Kim T-W, Byrne RH, Millero FJ, Feely RA, and Liu Y-M (2010) The universal ratio of boron to chlorinity for the North Pacific and North Atlantic oceans. *Geochimica et Cosmochimica Acta* 74(6): 1801–1811. https://doi.org/10.1016/j.gca.2009.12.027.

Lemarchand D, Gaillardet J, Lewin É, and Allègre CJ (2000) The influence of rivers on marine boron isotopes and implications for reconstructing past ocean pH. *Nature* 408(6815): 951–954. https://doi.org/10.1038/35050058.

Lemarchand D, Gaillardet J, Göpel C, and Manhès G (2002) An optimized procedure for boron separation and mass spectrometry analysis for river samples. *Chemical Geology* 182(2–4): 323–3234. https://doi.org/10.1016/S0009-2541(01)00329-1.

Lewis EL and Perkin RG (1981) The Practical salinity scale 1978: Conversion of existing data. *Deep Sea Research Part A. Oceanographic Research Papers* 28(4): 307–328. https://doi.org/10.1016/0198-0149(81)90002-9.

Lhomme N (2005) Global budget of water isotopes inferred from polar ice sheets. *Geophysical Research Letters* 32(20): L20502. https://doi.org/10.1029/2005GL023774.

Li G and Elderfield H (2013) Evolution of carbon cycle over the past 100 million years. *Geochimica et Cosmochimica Acta* 103: 11–25. https://doi.org/10.1016/j.gca.2012.10.014.

Liu X-P, Jin Z-J, Bai G-P, Guan M, Liu J, Pan Q-H, Li T, and Xing Y-J (2017) Formation and distribution characteristics of Proterozoic–Lower Paleozoic marine giant oil and gas fields worldwide. *Petroleum Science* 14(2): 237–260. https://doi.org/10.1007/s12182-017-0154-5.

Lord NS, Ridgwell A, Thorne MC, and Lunt DJ (2016) An impulse response function for the 'long tail' of excess atmospheric $CO_2$ in an Earth system model. *Global Biogeochemical Cycles* 30(1): 2–17. https://doi.org/10.1002/2014GB005074.

Lu W, Rickaby REM, Hoogakker BAA, Rathburn AE, Burkett AM, Dickson AJ, Martínez-Méndez G, et al. (2020) I/Ca in epifaunal benthic foraminifera: A semi-quantitative proxy for bottom water oxygen in a multi-proxy compilation for glacial ocean deoxygenation. *Earth and Planetary Science Letters* 533: 116055. https://doi.org/10.1016/j.epsl.2019.116055.

Lueker TJ, Dickson AG, and Keeling CD (2000) Ocean pCO2 calculated from dissolved inorganic carbon, alkalinity, and equations for K1 and K2: Validation based on laboratory measurements of CO2 in gas and seawater at equilibrium. *Marine Chemistry* 70(1–3): 105–119. https://doi.org/10.1016/S0304-4203(00)00022-0.

Lyle M (2003) Neogene carbonate burial in the Pacific Ocean. *Paleoceanography* 18(3): 2002PA000777. https://doi.org/10.1029/2002PA000777.

Lynch-Stieglitz J, Stocker TF, Broecker WS, and Fairbanks RG (1995) The influence of air-sea exchange on the isotopic composition of oceanic carbon: Observations and modeling. *Global Biogeochemical Cycles* 9(4): 653–665. https://doi.org/10.1029/95GB02574.

Mackensen A and Schmiedl G (2019) Stable carbon isotopes in paleoceanography: Atmosphere, oceans, and sediments. *Earth-Science Reviews* 197: 102893. https://doi.org/10.1016/j.earscirev.2019.102893.

Mackensen A and Schmield G (2019) Stable carbon isotopes in paleoceanography: atmosphere, oceans, and climates. *Earth-Science Reviews* 197. https://doi.org/10.1016/j.earscirev.2019.102893.

Maier-Reimer E and Hasselmann K (1987) Transport and storage of CO2 in the ocean ? An inorganic ocean-circulation carbon cycle model. *Climate Dynamics* 2(2): 63–90. https://doi.org/10.1007/BF01054491.

Marchitto TM, Curry WB, Lynch-Stieglitz J, Bryan SP, Cobb KM, and Lund DC (2014) Improved oxygen isotope temperature calibrations for cosmopolitan benthic foraminifera. *Geochimica et Cosmochimica Acta* 130: 1–11. https://doi.org/10.1016/j.gca.2013.12.034.

Marinov I, Follows M, Gnanadesikan A, Sarmiento JL, and Slater RD (2008a) How does ocean biology affect atmospheric *p* $CO_2$? Theory and models. *Journal of Geophysical Research* 113(C7): C07032. https://doi.org/10.1029/2007JC004598.

Marinov I, Gnanadesikan A, Sarmiento JL, Toggweiler JR, Follows M, and Mignone BK (2008b) Impact of oceanic circulation on biological carbon storage in the ocean and atmospheric *p* $CO_2$: Impact of oceanic circulation. *Global Biogeochemical Cycles* 22(3). https://doi.org/10.1029/2007GB002958.

Martens J, Wild B, Muschitiello F, O'Regan M, Jakobsson M, Semiletov I, Dudarev OV, and Gustafsson Ö (2020) Remobilization of dormant carbon from Siberian-Arctic permafrost during three past warming events. *Science Advances* 6(42): eabb6546. https://doi.org/10.1126/sciadv.abb6546.

McCrea JM (1950) On the isotopic chemistry of carbonates and a paleotemperature scale. *The Journal of Chemical Physics* 18(6): 849–857. https://doi.org/10.1063/1.1747785.

McInerney FA and Wing SL (2011) The Paleocene-Eocene thermal maximum: A perturbation of carbon cycle, climate, and biosphere with implications for the future. *Annual Review of Earth and Planetary Sciences* 39(1): 489–516. https://doi.org/10.1146/annurev-earth-040610-133431.

McKirdy DM and Imbus SW (1992) Precambrian petroleum: A decade of changing perceptions. In: Schidlowski M, Golubic S, Kimberley MM, McKirdy DM, and Trudinger PA (eds.) *Early Organic Evolution*, pp. 176–192. Berlin, Heidelberg: Springer Berlin Heidelberg. https://doi.org/10.1007/978-3-642-76884-2_12.

Meckler AN, Sexton PF, Piasecki AM, Leutert TJ, Marquardt J, Ziegler M, Agterhuis T, et al. (2022) Cenozoic evolution of deep ocean temperature from clumped isotope thermometry. *Science* 377(6601): 86–90. https://doi.org/10.1126/science.abk0604.

Menviel L, Spence P, and England MH (2015) Contribution of enhanced Antarctic bottom water formation to Antarctic warm events and millennial-scale atmospheric $CO_2$ increase. *Earth and Planetary Science Letters* 413: 37–50. https://doi.org/10.1016/j.epsl.2014.12.050.

Middelburg JJ, Soetaert K, and Hagens M (2020) Ocean alkalinity, buffering and biogeochemical processes. *Reviews of Geophysics* 58(3): e2019RG000681. https://doi.org/10.1029/2019RG000681.

Millero FJ and Pierrot D (1998) A chemical equilibrium model for natural waters. *Aquatic Geochemistry* 4(1): 153–199. https://doi.org/10.1023/A:1009656023546.

Milliman JD (1993) Production and accumulation of calcium carbonate in the ocean: Budget of a nonsteady state. *Global Biogeochemical Cycles* 7(4): 927–957. https://doi.org/10.1029/93GB02524.

Mills BJW, Krause AJ, Scotese CR, Hill DJ, Shields GA, and Lenton TM (2019) Modelling the long-term carbon cycle, atmospheric $CO_2$, and Earth surface temperature from late Neoproterozoic to present day. *Gondwana Research* 67: 172–186. https://doi.org/10.1016/j.gr.2018.12.001.

Mook WG (1986) 13C in atmospheric $CO_2$. *Netherlands Journal of Sea Research* 20(2–3): 211–223. https://doi.org/10.1016/0077-7579(86)90043-8.

Morel FMM and Hering JG (1993) *Principles and Applications of Aquatic Chemistry*. A Wiley-Interscience Publication, New York: Wiley.

Müller RD, Sdrolias M, Gaina C, and Roest WR (2008) Age, spreading rates, and spreading asymmetry of the world's ocean crust. *Geochemistry, Geophysics, Geosystems* 9(4): 2007GC001743. https://doi.org/10.1029/2007GC001743.

Naegler T and Levin I (2006) Closing the global radiocarbon budget 1945–2005. *Journal of Geophysical Research: Atmospheres* 111(D12): 2005JD006758. https://doi.org/10.1029/2005JD006758.

Nir O, Vengosh A, Harkness JS, Dwyer GS, and Lahav O (2015) Direct measurement of the boron isotope fractionation factor: Reducing the uncertainty in reconstructing ocean paleo-pH. *Earth and Planetary Science Letters* 414: 1–5. https://doi.org/10.1016/j.epsl.2015.01.006.

Nissan A, Alcolombri U, Peleg N, Galili N, Jimenez-Martinez J, Molnar P, and Holzner M (2023) Global warming accelerates soil heterotrophic respiration. *Nature Communications* 14(1): 3452. https://doi.org/10.1038/s41467-023-38981-w.

O'Leary MH (1993) Biochemical basis of carbon isotope fractionation. In: *Stable Isotopes and Plant Carbon-Water Relations*, pp. 19–28. Elsevier. https://doi.org/10.1016/B978-0-08-091801-3.50009-X.

O'Neil JR, Clayton RN, and Mayeda TK (1969) Oxygen isotope fractionation in divalent metal carbonates. *Journal of Chemical Physics* 51: 5547–5558. https://doi.org/10.1063/1.1671982.

Opdyke BN and Wilkinson BH (1988) Surface area control of shallow cratonic to deep marine carbonate accumulation. *Paleoceanography* 3(6): 685–703. https://doi.org/10.1029/PA003i006p00685.

PALAEOSENS Project Members (2012) Making sense of palaeoclimate sensitivity. *Nature* 491(7426): 683–691. https://doi.org/10.1038/nature11574.

Pälike H, Norris RD, Herrle JO, Wilson PA, Coxall HK, Lear CH, Shackleton NJ, Tripati AK, and Wade BS (2006) The heartbeat of the oligocene climate system. *Science* 314(5807): 1894–1898. https://doi.org/10.1126/science.1133822.

Pälike H, Lyle MW, Nishi H, Raffi I, Ridgwell A, Gamage K, Klaus A, et al. (2012) A Cenozoic record of the equatorial Pacific carbonate compensation depth. *Nature* 488(7413): 609–614. https://doi.org/10.1038/nature11360.

Palmer MR (2017) Boron cycling in subduction zones. *Elements* 13: 237–242.

Panchuk K, Ridgwell A, and Kump LR (2008) Sedimentary response to Paleocene-Eocene thermal maximum carbon release: A model-data comparison. *Geology* 36(4): 315. https://doi.org/10.1130/G24474A.1.

Paytan A, Griffith EM, Eisenhauer A, Hain MP, Wallmann K, and Ridgwell A (2021) A 35-million-year record of seawater stable Sr isotopes reveals a fluctuating global carbon cycle. *Science* 371(6536): 1346–1350. https://doi.org/10.1126/science.aaz9266.

Peters SE and Gaines RR (2012) Formation of the 'great unconformity' as a trigger for the Cambrian explosion. *Nature* 484(7394): 363–366. https://doi.org/10.1038/nature10969.

Rae JWB (2018) Boron isotopes in foraminifera: Systematics, biomineralisation, and $CO_2$ reconstruction. In: Marschall H and Foster G (eds.) *Boron Isotopes. Advances in Isotope Geochemistry*, pp. 107–143. Cham: Springer International Publishing. https://doi.org/10.1007/978-3-319-64666-4_5.

Rae JWB, Foster GL, Schmidt DN, and Elliott T (2011) Boron isotopes and B/Ca in benthic foraminifera: Proxies for the deep ocean carbonate system. *Earth and Planetary Science Letters* 302(3–4): 403–413. https://doi.org/10.1016/j.epsl.2010.12.034.

Rae JWB, Zhang YG, Liu X, Foster GL, Stoll HM, and Whiteford RDM (2021) Atmospheric $CO_2$ over the past 66 million years from marine archives. *Annual Review of Earth and Planetary Sciences* 49(1): 609–641. https://doi.org/10.1146/annurev-earth-082420-063026.

Raitzsch M, Hain M, Henehan M, and Gattuso J-P (2021) *Seacarbx-Seacarb Extension for Deep-Time Carbonate System Calculations*. Zenodo. https://doi.org/10.5281/ZENODO.4432170.

Raymo ME (1991) Geochemical evidence supporting T. C. Chamberlin's theory of glaciation. *Geology* 19(4): 344. https://doi.org/10.1130/0091-7613(1991)019<0344:GESTCC>2.3.CO;2.

Raymo ME, Ruddiman WF, and Froelich PN (1988) Influence of late Cenozoic mountain building on ocean geochemical cycles. *Geology* 16(7): 649. https://doi.org/10.1130/0091-7613(1988)016<0649:IOLCMB>2.3.CO;2.

Redfield AC (1934) On the proportions of organic derivatives in sea water and their relation to the composition of plankton. In: *James Johnstone Memorial Volume*, pp. 176–192. University Press of Liverpool.

Redfield AC, Ketchum BH, and Richards FA (1963) The influence of organisms on the composition of sea-water. In: Hill MN (ed.) *The Sea*, Vol. 2, pp. 26–77. New York: Wiley Interscience.

Riahi K, Van Vuuren DP, Kriegler E, Edmonds J, O'Neill BC, Fujimori S, Bauer N, et al. (2017) The shared socioeconomic pathways and their energy, land use, and greenhouse gas emissions implications: An overview. *Global Environmental Change* 42: 153–168. https://doi.org/10.1016/j.gloenvcha.2016.05.009.

Ridgwell A (2005) A mid Mesozoic revolution in the regulation of ocean chemistry. *Marine Geology* 217(3–4): 339–357. https://doi.org/10.1016/j.margeo.2004.10.036.

Ridgwell A, Hargreaves JC, Edwards NR, Annan JD, Lenton TM, Marsh R, Yool A, and Watson A (2007) Marine geochemical data assimilation in an efficient Earth system model of global biogeochemical cycling. *Biogeosciences* 4(1): 87–104. https://doi.org/10.5194/bg-4-87-2007.

Ruppel CD and Kessler JD (2017) The interaction of climate change and methane hydrates. *Reviews of Geophysics* 55(1): 126–168. https://doi.org/10.1002/2016RG000534.

Russon T, Paillard D, and Elliot M (2010) Potential origins of 400-500 Kyr periodicities in the ocean carbon cycle: A box model approach: THE 400-500 kyr carbon cycle periodicities. *Global Biogeochemical Cycles* 24(2). https://doi.org/10.1029/2009GB003586.

Sanyal A, Nugent M, Reeder RJ, and Bijma J (2000) Seawater pH control on the boron isotopic composition of calcite: Evidence from inorganic calcite precipitation experiments. *Geochimica et Cosmochimica Acta* 64(9): 1551–1555. https://doi.org/10.1016/S0016-7037(99)00437-8.

Sarmiento JL and Bender M (1994) Carbon biogeochemistry and climate change. *Photosynthesis Research* 39(3): 209–234. https://doi.org/10.1007/BF00014585.

Sarmiento JL and Gruber N (2006) *Ocean Biogeochemical Dynamics*. Princeton: Princeton University Press.

Schmittner A, Gruber N, Mix AC, Key RM, Tagliabue A, and Westberry TK (2013) Biology and air–sea gas exchange controls on the distribution of carbon isotope ratios ($\Delta^{13}C$) in the ocean. *Biogeosciences* 10(9): 5793–5816. https://doi.org/10.5194/bg-10-5793-2013.

Schmittner A, Bostock HC, Cartapanis O, Curry WB, Filipsson HL, Galbraith ED, Gottschalk J, et al. (2017) Calibration of the carbon isotope composition ($\delta^{13}C$) of benthic foraminifera. *Paleoceanography* 32(6): 512–530. https://doi.org/10.1002/2016PA003072.

Schubert BA and Hope Jahren A (2013) Reconciliation of marine and terrestrial carbon isotope excursions based on changing atmospheric $CO_2$ levels. *Nature Communications* 4(1): 1653. https://doi.org/10.1038/ncomms2659.

Seton M, Dietmar Müller R, Zahirovic S, Williams S, Wright NM, Cannon J, Whittaker JM, Matthews KJ, and McGirr R (2020) A global data set of present-day oceanic crustal age and seafloor spreading parameters. *Geochemistry, Geophysics, Geosystems* 21(10): e2020GC009214. https://doi.org/10.1029/2020GC009214.

Shackleton NJ (1974) *Attainment of Isotopic Equilibrium between Ocean Water and the Benthonic Foraminifera Genus Uvigerina: Isotopic Changes in the Ocean During the Last Glacial*. CNRS. https://core.ac.uk/download/pdf/11775131.pdf.

Sharp JD, Pierrot D, Humphreys MP, Epitalon J-M, Orr JC, Lewis ER, and Wallace DWR (2020) *CO2SYSv3 for MATLAB*. Zenodo. https://doi.org/10.5281/ZENODO.3950563.

Shevenell A, Delaney P, Meissner K, Menviel L, and Mix A (2020) Introduction to the special issue. Paleoceanography: Lessons for a changing world. *Oceanography* 33(2): 13–15. https://doi.org/10.5670/oceanog.2020.226.

Shields G and Veizer J (2002) Precambrian marine carbonate isotope database: Version 1.1. *Geochemistry, Geophysics, Geosystems* 3(6). https://doi.org/10.1029/2001GC000266.

Si W and Rosenthal Y (2019) Reduced continental weathering and marine calcification linked to late Neogene decline in atmospheric $CO_2$. *Nature Geoscience* 12(10): 833–838. https://doi.org/10.1038/s41561-019-0450-3.

Si W, Herbert T, Mengxi W, and Rosenthal Y (2023) Increased biogenic calcification and burial under elevated $p\,CO_2$ during the Miocene: A model-data comparison. *Global Biogeochemical Cycles* 37(6): e2022GB007541. https://doi.org/10.1029/2022GB007541.

Siegenthaler U, Stocker TF, Monnin E, Lüthi D, Schwander J, Stauffer B, Raynaud D, et al. (2005) Stable carbon cycleclimate relationship during the late Pleistocene. *Science* 310(5752): 1313–1317. https://doi.org/10.1126/science.1120130.

Sigman DM and Hain MP (2013) The biological productivity of the ocean. *Nature Education* 3(6): 1–16.

Sigman DM, McCorkle DC, and Martin WR (1998) The calcite Lysocline as a constraint on glacial/interglacial low-latitude production changes. *Global Biogeochemical Cycles* 12(3): 409–427. https://doi.org/10.1029/98GB01184.

Simon L, Lécuyer C, Maréchal C, and Coltice N (2006) Modelling the geochemical cycle of boron: Implications for the long-term δ11B evolution of seawater and oceanic crust. *Chemical Geology* 225(1–2): 61–76. https://doi.org/10.1016/j.chemgeo.2005.08.011.

Slotnick BS, Lauretano V, Backman J, Dickens GR, Sluijs A, and Lourens L (2015) Early Paleogene variations in the calcite compensation depth: New constraints using old borehole sediments from across Ninetyeast Ridge, Central Indian Ocean. *Climate of the Past* 11(3): 473–493. https://doi.org/10.5194/cp-11-473-2015.

Spero HJ, Bijma J, Lea DW, and Bemis BE (1997) Effect of seawater carbonate concentration on foraminiferal carbon and oxygen isotopes. *Nature* 390(6659): 497–500. https://doi.org/10.1038/37333.

Stallard RF and Edmond JM (1983) Geochemistry of the Amazon: 2. The influence of geology and weathering environment on the dissolved load. *Journal of Geophysical Research: Oceans* 88(C14): 9671–9688. https://doi.org/10.1029/JC088iC14p09671.

Stocker TF (2015) The silent services of the world ocean. *Science* 350(6262): 764–765. https://doi.org/10.1126/science.aac8720.

Suárez-Ibarra JY, Frozza CF, Petró SM, and Pivel MAG (2021) Fragment or broken? Improving the planktonic foraminifera fragmentation assessment. *Palaios* 36(5): 165–172. https://doi.org/10.2110/palo.2020.062.

Sulpis O, Boudreau BP, Mucci A, Jenkins C, Trossman DS, Arbic BK, and Key RM (2018) Current $CaCO_3$ dissolution at the seafloor caused by anthropogenic $CO_2$. *Proceedings of the National Academy of Sciences* 115(46): 11700–11705. https://doi.org/10.1073/pnas.1804250115.

Sundquist ET and Visser Ackerman K (2014) The geologic history of the carbon cycle. In: *Treatise on Geochemistry*, pp. 361–398. Elsevier. https://doi.org/10.1016/B978-0-08-095975-7.00809-3.

Super JR, Thomas E, Pagani M, Huber M, O'Brien C, and Hull PM (2018) North Atlantic temperature and pCO2 coupling in the early-middle Miocene. *Geology* 46(6): 519–522. https://doi.org/10.1130/G40228.1.

Tian H, Yao Y, Li Y, Shi H, Pan S, Najjar RG, Pan N, et al. (2023) Increased terrestrial carbon export and $CO_2$ evasion from global inland waters since the preindustrial era. *Global Biogeochemical Cycles* 37(10): e2023GB007776. https://doi.org/10.1029/2023GB007776.

Tierney JE, Zhu J, Li M, Ridgwell A, Hakim GJ, Poulsen CJ, Whiteford RDM, Rae JWB, and Kump LR (2022) Spatial patterns of climate change across the Paleocene–Eocene thermal maximum. *Proceedings of the National Academy of Sciences* 119(42): e2205326119. https://doi.org/10.1073/pnas.2205326119.

Toggweiler JR (1999) Variation of atmospheric $CO_2$ by ventilation of the ocean's deepest water. *Paleoceanography* 14: 571–588. https://doi.org/10.1029/1999pa900033.

Turner SK (2018) Constraints on the onset duration of the Paleocene–Eocene thermal maximum. *Philosophical Transactions of the Royal Society A: Mathematical, Physical and Engineering Sciences* 376(2130): 20170082. https://doi.org/10.1098/rsta.2017.0082.

Tyrrell T and Zeebe RE (2004) History of carbonate ion concentration over the last 100 million years. *Geochimica et Cosmochimica Acta* 68(17): 3521–3530. https://doi.org/10.1016/j.gca.2004.02.018.

Uchikawa J, Penman DE, Zachos JC, and Zeebe RE (2015) Experimental evidence for kinetic effects on B/Ca in synthetic calcite: Implications for potential B(OH)4− and B(OH)3 incorporation. *Geochimica et Cosmochimica Acta* 150: 171–191. https://doi.org/10.1016/j.gca.2014.11.022.

Urey HC, Lowenstam HA, and Epstein S (1951) Measurement of paleotemperatures and temperatures of the Upper Cretaceous of England, Denmark, and the southeastern United States. *Bulletin of the Geological Society of America* 62: 399–416.

Veizer J, Ala D, Azmy K, Bruckschen P, Buhl D, Bruhn F, Carden GAF, et al. (1999) 87Sr/86Sr, δ13C and δ18O evolution of Phanerozoic seawater. *Chemical Geology* 161(1–3): 59–88. https://doi.org/10.1016/S0009-2541(99)00081-9.

Vervoort P, Adloff M, Greene SE, Kirtland S, and Turner. (2019) Negative carbon isotope excursions: An interpretive framework. *Environmental Research Letters* 14(8): 085014. https://doi.org/10.1088/1748-9326/ab3318.

Vervoort P, Turner SK, Rochholz F, and Ridgwell A (2021) Earth system model analysis of how astronomical forcing is imprinted onto the marine geological record: The role of the inorganic (carbonate) carbon cycle and feedbacks. *Paleoceanography and Paleoclimatology* 36(10): e2020PA004090. https://doi.org/10.1029/2020PA004090.

Vollmer TD, Ito T, and Lynch-Stieglitz J (2022) Proxy-based preformed phosphate estimates point to increased biological pump efficiency as primary cause of last glacial maximum $CO_2$ drawdown. *Paleoceanography and Paleoclimatology* 37(11): e2021PA004339. https://doi.org/10.1029/2021PA004339.

Von Strandmann P, Philip AE, Jones MT, Joshua West A, Murphy MJ, Stokke EW, Tarbuck G, Wilson DJ, Pearce CR, and Schmidt DN (2021) Lithium isotope evidence for enhanced weathering and erosion during the Paleocene-Eocene thermal maximum. *Science Advances* 7(42). https://doi.org/10.1126/sciadv.abh4224.

Walker JCG, Hays PB, and Kasting JF (1981) A negative feedback mechanism for the long-term stabilization of Earth's surface temperature. *Journal of Geophysical Research: Oceans* 86(C10): 9776–9782. https://doi.org/10.1029/JC086iC10p09776.

Wallace WJ (1974) *The Development of the Chlorinity/Salinity Concept in Oceanography*. Amsterdam: Elsevier Scientific Pub. Co.

Wanninkhof R (1992) Relationship between wind speed and gas exchange over the ocean. *Journal of Geophysical Research: Oceans* 97(C5): 7373–7382. https://doi.org/10.1029/92JC00188.

Watson AJ, Schuster U, Shutler JD, Holding T, Ashton IGC, Landschützer P, Woolf DK, and Goddijn-Murphy L (2020) Revised estimates of ocean-atmosphere $CO_2$ flux are consistent with ocean carbon inventory. *Nature Communications* 11(1): 4422. https://doi.org/10.1038/s41467-020-18203-3.

Weber SL (2010) The utility of Earth system models of intermediate complexity (EMICs). *WIREs Climate Change* 1(2): 243–252. https://doi.org/10.1002/wcc.24.

Werner C, Fischer TP, Aiuppa A, Edmonds M, and al. et. (2019) Carbon dioxide emissions from subaerial volcanic regions. In: Orcutt BN, Daniel I, and Dasgupta R (eds.) *Deep Carbon: Past to Present*, 1st edn, pp. 188–236. Cambridge University Press. https://doi.org/10.1017/9781108677950.

Westerhold T, Marwan N, Drury AJ, Liebrand D, Agnini C, Anagnostou E, Barnet JSK, et al. (2020) An astronomically dated record of Earth's climate and its predictability over the last 66 million years. *Science* 369(6509): 1383–1387. https://doi.org/10.1126/science.aba6853.

Wolf-Gladrow DA, Zeebe RE, Klaas C, Körtzinger A, and Dickson AG (2007) Total alkalinity: The explicit conservative expression and its application to biogeochemical processes. *Marine Chemistry* 106(1–2): 287–300. https://doi.org/10.1016/j.marchem.2007.01.006.

Wong TE, Cui Y, Royer DL, and Keller K (2021) A tighter constraint on Earth-system sensitivity from long-term temperature and carbon-cycle observations. *Nature Communications* 12(1): 3173. https://doi.org/10.1038/s41467-021-23543-9.

Wood M, Hayes CT, and Paytan A (2023) Global Quaternary carbonate burial: Proxy- and model-based reconstructions and persisting uncertainties. *Annual Review of Marine Science* 15(1): 277–302. https://doi.org/10.1146/annurev-marine-031122-031137.

Yan Y, Bender ML, Brook EJ, Clifford HM, Kemeny PC, Kurbatov AV, Mackay S, et al. (2019) Two-million-year-old snapshots of atmospheric gases from Antarctic ice. *Nature* 574(7780): 663–666. https://doi.org/10.1038/s41586-019-1692-3.

Yu J and Elderfield H (2007) Benthic foraminiferal B/Ca ratios reflect deep water carbonate saturation state. *Earth and Planetary Science Letters* 258(1–2): 73–86. https://doi.org/10.1016/j.epsl.2007.03.025.

Yu J, Menviel L, Jin ZD, Thornalley DJR, Foster GL, Rohling EJ, McCave IN, et al. (2019) More efficient North Atlantic carbon pump during the last glacial maximum. *Nature Communications* 10(1): 2170. https://doi.org/10.1038/s41467-019-10028-z.

Zachos JC, Arthur MA, and Dean WE (1989) Geochemical evidence for suppression of pelagic marine productivity at the cretaceous/tertiary boundary. *Nature* 337(6202): 61–64. https://doi.org/10.1038/337061a0.

Zachos J, Pagani M, Sloan L, Thomas E, and Billups K (2001) Trends, rhythms, and aberrations in global climate 65 Ma to present. *Science* 292(5517): 686–693. https://doi.org/10.1126/science.1059412.

Zeebe RE (2012) LOSCAR: Long-term ocean-atmosphere-sediment CArbon cycle reservoir model v2.0.4. *Geoscientific Model Development* 5(1): 149–166. https://doi.org/10.5194/gmd-5-149-2012.

Zeebe RE, Zachos JC, and Dickens GR (2009) Carbon dioxide forcing alone insufficient to explain Palaeocene–Eocene thermal maximum warming. *Nature Geoscience* 2(8): 576–580. https://doi.org/10.1038/ngeo578.

Zeebe RE, Ridgwell A, and Zachos JC (2016) Anthropogenic carbon release rate unprecedented during the past 66 million years. *Nature Geoscience* 9(4): 325–329. https://doi.org/10.1038/ngeo2681.

Zeebe RE, Westerhold T, Littler K, and Zachos JC (2017) Orbital forcing of the Paleocene and Eocene carbon cycle: Orbital forcing Paleocene-Eocene C cycle. *Paleoceanography* 32(5): 440–465. https://doi.org/10.1002/2016PA003054.

Zhang X, Knorr G, Lohmann G, and Barker S (2017) Abrupt North Atlantic circulation changes in response to gradual $CO_2$ forcing in a glacial climate state. *Nature Geoscience* 10(7): 518–523. https://doi.org/10.1038/ngeo2974.

Ziegler M, Diz P, Hall IR, and Zahn R (2013) Millennial-scale changes in atmospheric $CO_2$ levels linked to the southern ocean carbon isotope gradient and dust flux. *Nature Geoscience* 6(6): 457–461. https://doi.org/10.1038/ngeo1782.

Zondervan JR, Hilton RG, Dellinger M, Clubb FJ, Roylands T, and Ogrič M (2023) Rock organic carbon oxidation $CO_2$ release offsets silicate weathering sink. *Nature* 623(7986): 329–333. https://doi.org/10.1038/s41586-023-06581-9.